Dissertation
submitted to the
Combined Faculties for the Natural Sciences
and for Mathematics
of the Ruperto-Carola University of Heidelberg,
Germany
for the degree of
Doctor of Natural Sciences

presented by
Dipl.-Phys. Peter Krüger
born in: Princeton/NJ (USA)
Oral examination: July 7$^{\text{th}}$, 2004

Coherent matter waves near surfaces

Referees: Prof. Dr. Jörg Schmiedmayer
Prof. Dr. Markus Oberthaler

Zusammenfassung

Kohärente Materiewellen in Oberflächennähe

Neutrale Atome können in der Nähe von Atomchips auf mikroskopischer Skala gefangen und manipuliert werden. Ein Teil dieser Arbeit beschäftigt sich mit der Entwicklung und dem Test mikroskopischer atomoptischer Elemente. Ein richtungsunabhängiger Materiewellenleiter und neuartige magneto-elektrische Potentiale werden experimentell mit kalten thermischen Lithiumatomen untersucht.
Während des Aufbaus einer neuen Apparatur für ultrakalte Rubidiumatome wurde ein neuer Typ einer integrierten magneto-optischen Falle für die vereinfachte Produktion von Bose-Einstein Kondensaten (BEC) in Oberflächennähe implementiert. Der Einfluss von Oberflächen-Störpotentialen auf BECs wird untersucht. Eine Verringerung störender Effekte um zwei Größenordnungen für lithographische im Gegensatz zu galvanischer Chipfabrikation wurde gemessen. Der Einfluss thermisch induzierten Stromrauschens auf die kohärente Evolution von Materiewellen in der Nähe der Oberfläche wird theoretisch untersucht und erste experimentelle Ergebnisse werden präsentiert.

Abstract

Coherent matter waves near surfaces

Neutral atoms can be trapped and manipulated on microscopic scales near surfaces of atom chips. The work covered by this thesis includes the development and test of microscopic atom optical tools. An omni-directional magnetic matter wave guide and novel types of magneto-electric trapping potentials are investigated experimentally with cold thermal lithium atoms.
During the construction of a new setup working with ultracold rubidium atoms, a novel type of integrated magneto-optical trap for a simplified production of Bose-Einstein condensates (BEC) near surfaces was implemented. The influence of surface disorder potentials on BECs is studied. A reduction of disturbing effects by two orders of magnitude for a lithographic fabrication process over electroplating is found. The impact of thermal current noise on the coherent evolution of matter waves near surfaces is investigated theoretically and initial experimental results are presented.

Contents

1 Introduction

Modern physics has come a long way since Max Planck introduced his quantum hypothesis in 1900 [161]. Today, the preparations for the centennial of the *annus mirabilis* 1905 are in full bloom. During this single year, Albert Einstein initiated and promoted the development of modern physics in the diverse areas of Brownian motion [55], special relativity [57], and quantum theory [56].
The consequences of relativity are spectacular and in the public Einstein is probably best known for this conception. But the implications and applications of quantum mechanics are driving today's technology and research more than any other modern scientific theory.
Soon after its mathematical formulation [87, 176], the interpretation problems of quantum theory were expounded, in particular after the famous paper by Einstein, Podolsky, and Rosen was published in 1935 [58]. The role of experiments – at that time still gedanken-experiments – elucidating the nature of the new theory was crucial. The most noted protagonists of the debate on issues like locality of actions and completeness of the theory were Albert Einstein and Niels Bohr [194].
It was not until 1964 that John Bell realized that some of the unresolved academic questions regarding the interpretation of quantum mechanics can actually be put to a decisive experimental test [16, 17]. Soon after, experiments – now in the laboratories – showed that Bell's inequalities can indeed be violated. The implication of the new results, namely the falsification of local realistic theories, was so severe and so much against the intuition of classical physics that experimental 'loopholes' are continued to be eliminated until today [103].
The availability of sophisticated laser technology and the fast development of quantum optics during the 1980s and early 1990s led to a whole sequence of physical implementations of former gedanken-experiments. The often cited teleportation of photons is a typical example [18, 23].
Again it were the rapid advances in technology and experimental research that initiated the drive towards actually applying quantum mechanisms to the development of usable devices rather than the mere understanding of the theory. This does not mean a discontinuation of investigations in fundamental issues. On the contrary, fundamental research and applied science mutually profit from this new trend.
Today, a high level of control over complex quantum systems in very different physical systems is possible. This is true for condensed matter systems as well as in quantum optics. Examples are molecules in liquid solutions that are used

for basic quantum computing by nuclear magnetic resonance (NMR) techniques [39] and commercially available quantum cryptography devices based on single photons [135].

Neutral atoms have specific properties that make them interesting objects for a controlled manipulation on the quantum level. On the one hand, the natural coupling to the uncontrolled environment is weak, on the other hand, quantum optics techniques are well developed in a way that provides precise manipulation handles. In particular, the invention of the magneto-optical trap (MOT) [163] has made it possible to cool atoms to ultra-low temperatures. After only a few years this led to the first demonstration of Bose-Einstein condensation (BEC) [1, 41, 24], a phenomenon that had been predicted 70 years before [22]. The regime of quantum degenerate gases when defined quantum states are macroscopically populated is one of the major research field in today's quantum optics. In this domain, it is even possible to manipulate the inter-particle interaction at will, for example by means of Feshbach resonances [105]. The controlled formation of cold molecules, even molecular BECs [104, 72] and the currently intensively studied crossover between the superfluid BCS (Bardeen-Cooper-Schrieffer) state and BEC [10, 99, 14] are an outcome of these fascinating possibilities.

The degree of control achievable in cold atomic systems allows to consider the ideas of quantum information processing (QIP). Here, individual quantum systems carry information in their quantum state. The information is processed by entangling these systems in a controlled way and by finally observing the outcome of the quantum evolution. Originally, the discovery of specific efficient quantum algorithms impossible to implement on classical computers initiated focussed research in this direction [50, 178, 76]. However, the true significance of QIP, at least in the near future, will be the possibility of the simulation of one (undecoded) quantum system by another. The observation of the Mott insulator transition in a quantum gas [71] and the indications of a successful formation of a degenerate Fermi gas in the superfluid BCS-phase [99, 14] are two examples.

The approach of this thesis is to combine the well established and still advancing techniques of atom optics with today's highly developed microfabrication techniques to form matter wave devices that are capable to control complex atomic quantum systems on a microscopic level. Such *atom chips* have the potential to be as successful as integrated microscopic devices are in electronics and photonics. The goal of the atom chip concept is to form a single integrated device based on various types of manipulation handles that would provide control on the single particle level. This can then be used to build up controlled complex systems by gradually increasing the number of particles. On the other hand, one can start with complex quantum systems like ensembles of (fermionic or bosonic) quantum gases and gradually gain control over ever smaller subsystems. We have reviewed the concepts and the status of research in this new field in [62, 121].

Based on earlier experiments with simple magnetic wire guides for cold thermal atoms [48, 46], we started to build and experimentally test the first atom chips

during my diploma thesis [61, 116]. I continued to participate in the further development of the atom chip tool box as a PhD student. Initially, I focussed on conceptualizing and experimentally testing new manipulation tools. The developed concepts and their experimental trial are discussed in chapter 2. These experiments were performed with a ^{7}Li apparatus. The newly developed mechanisms include an omnidirectional atom guide [133, 28] and the first realization of a combined magneto-electric trapping potential [119].
Later, we started to build a new setup working with ^{87}Rb atoms. During the past two years, we have been able to devise a simplified procedure to produce BECs [197] (chapter 3). The routinely available condensates rendered experiments very close to the surface of atom chips possible.
In order to exhaust the full capabilities of micromanipulation of atoms, it is inevitable to be able to approach the surface of an atom chip to $\sim 1\mu$m or less. Only at such distances complex potentials can be formed with micron resolution which in turn is necessary in order to realize quantum operation such as atom-atom entanglement by controlled inter-atomic collisions [184]. Consequently, it has been attempted to approach the surfaces of atom chips to as small as possible distances. On this path, a number of potentially disturbing mechanisms have to be controlled. The mechanisms are on the one hand static deviations from the designed manipulation potentials caused by fabrication imperfections. On the other hand, noisy potentials can lead to unwanted coupling of the atoms to the surface of the atom chip.
These issues are addressed in this thesis. Chapter 3 deals with static disorder potentials. We have been able to reduce unwanted effects by two orders of magnitude with respect to previous experiments performed in other groups. In the course, it has turned out that BECs can actually be used as ultra-sensitive microscopic probe of subtle disorder effects.
Chapter 4 covers theoretical investigations of the influence of noisy potentials on the controlled quantum evolution near surfaces and our first experimental tests.
This thesis concludes with an outlook (chapter 5) where some of the possible paths of future experiments are highlighted and some preliminary results are discussed.

2 Tools for matter wave manipulation near surfaces

The flexibility and the great variety of possibilities of atom manipulation near surfaces have been advertised in the introduction. Some of the tools that may be used for the manipulation of neutral atoms are introduced in this chapter. A number of examples of experimental implementations will be given. These experiments with cold thermal atoms were performed in order to understand and test the devices that were later employed in the experiments with matter waves near surfaces. In most cases the apparatus was a bosonic lithium magneto-optical trap (MOT) setup (appendix A) as described in detail in [45, 35].
The chapter starts with some general comments about parameter ranges of microtrap experiments and performance criteria for the the atom chips (Sect. 2.1) and their fabrication which is described in Sects. 2.2 and 2.3. The design of microscopic atom-optical tools based on magnetic and electrostatic fields and examples of test experiments will be given in the last two sections of the chapter (Sects. 2.4 and 2.5).

2.1 Cold atoms in microtraps

Out of the many possibilities for the choice of a physical implementation of a controllable quantum system, neutral atoms have two distinct advantages: The absence of electric charge minimizes unwanted coupling to the environment to higher order effects. On the other hand, the internal structure with its sharp line spectrum provides natural handles for purposeful manipulation.
External electromagnetic fields are used to manipulate the atoms through different interaction mechanisms. The interactions applied can be dynamic or static magnetic, electric, or light fields or combinations thereof. The various coupling strengths and practical limits for maximal field strengths set the energy scales of the associated potentials.
Magnetic fields couple to the magnetic moment of a neutral atom given by its total angular momentum. The order of magnitude of the coupling strength is given by the Bohr magneton $\mu_B = 9.27 \times 10^{-24}\mathrm{J/T} = h \times 1.4\mathrm{MHz/G} = k_B \times 67\mu\mathrm{K/G}$. Consequently, field variations of tens of Gauss allow to confine atomic samples of temperatures of $\sim$ 1mK and below.
The coupling of neutral atoms to *electric fields* is in general much weaker since

it is only a second order effect. The induced dipole of the atom is drawn towards increasing external electric fields. Typical polarizabilities of alkali atoms are on the order of $\alpha = 4\pi\epsilon_0 \times 50\text{Å}^3 \approx k_B \times 400\mu\text{K}/(\text{V}/\mu\text{m})^2$ (^{87}Rb). This means that even for the manipulation of cold atoms ($T \sim 100\mu$K), relatively large field variations are necessary. Very high voltages can only be avoided if the distances between electrodes are reduced to microscopic scales. Unlike magnetic potentials, the ultimate depth of electrostatic potentials is limited since the maximally possible field is determined by material breakthrough fields (typically on the order of several tens of V/μm).

While the coupling to magnetic and electric fields leads to conservative potentials for the atom, *light fields* exert both conservative and dissipative forces. The dissipative *scattering force* dominates at near resonant light frequencies. The operation principle of laser cooling in magneto-optical traps (MOT) and sub-Doppler molasses cooling as applied in the experiments presented here is based on this force. With these techniques, the temperature scales given above are routinely reached within typically 10s for ensembles of $\sim 10^8$ atoms. Thus cold atom clouds or fractions thereof can directly be loaded to potentials based on magnetic and electric fields. The loading efficiencies will in general depend on the phase space volume of the original atom cloud and on the overlap with the bound states in the trapping potential (*mode matching*).

For large detuning δ of the light field relative to an atomic resonance ($\delta \gg \Gamma, \Omega$; Γ is the line width of the atomic transition, Ω is the Rabi frequency characterizing the atom field coupling), the other part of the light force, the conservative *dipole force*, dominates. The strength of dipole potentials is given by the ratio I/δ (I is the light field intensity). For a controlled manipulation of atoms, a reduced spontaneous photon scattering is desirable which limits the minimally usable δ. The value of this limit depends on the specific experimental situation. Typically, accessible laser intensities lead to potential variations on the order of $k_B \times$mK which again allows an efficient transfer of laser cooled atoms to optical dipole traps [73]. An important feature of confining optical dipole potentials is that they are independent of the magnetic substate of the atom unlike magnetic traps.

Macroscopic implementations of these types of potentials are routinely used as atom-optical tools. For example, Bose-Einstein condensates (BEC) have been formed in magnetic [1, 41, 24] and optical [13] traps. Quantum manipulation on the single or few atom level, however, requires a confinement on a much smaller scale that should be on the order of μm or below [184]. This implies that the fields have to be varied on the same length scale. The field producing components thus have to be structured with a (sub)micron resolution, and the atoms have to be brought similarly close to these structures. Such demands can be met if microfabricated devices, *atom chips*, are used.

In the remainder of this chapter, the properties of atom chips utilizing magnetic and electric potentials, their fabrication, and implementations of microscopic atom-optical tools will be discussed in more detail. Optical atom chips have been

developed elsewhere [21] and a future combination of optical, magnetic, and electric micropotentials promises to further enrich the range of possible experiments.

2.2 Fabrication of atom chips

As mentioned above, the full range of capabilities of atom manipulation in microtraps becomes available only if potentials with a high spatial resolution can be realized. In order to study and exploit effects like tunnelling and inter-trap atom-atom coupling, for example, it is therefore necessary to design structures with sizes of a few microns and below. Microstructures also facilitate extreme trap gradients and frequencies (up to MHz) and the implementation of highly anisotropic trapping potentials (aspect ratios $> 10^4$) for investigations of atoms in (quasi) one- or two-dimensional environments [150, 157] (Sect. 5.1).
Technical advantages of substrate mounted microstructures include robustness and alignment of potentials by construction, scalability of the fabrication to multiple similar or equal structures, high degree of achievable structure complexity, and large tolerated current densities (Sect. 2.3).
From the theoretical considerations presented in chapters 3 and 4 two important conclusions are drawn.
One concern is the extreme sensitivity of ultracold atoms to small disorder potentials that occur in addition to the confining trapping and guiding potentials. Such potentials have been shown to be derivable from wire edge roughness [190, 60]. Extreme care has to be taken to reduce all wire roughness, not only at the edges but also in the bulk metal since conductivity fluctuations may also lead to unwanted disorder fields (Sect. 3.2).
The other important issue is the rapid increase of loss, heating, and decoherence rates as the surface is approached (Sect. 4.1). Since these rates depend on the resistance of the potential creating structure, the tolerated current densities should be as high as possible. This will not only allow to reduce the amount of metal used but also more extreme trap parameters can be reached [62] 4.2.
In principle, standard lithographical microchip production techniques may be applied to fabricate atom chips. There are, however, a number of peculiarities that necessitate to customize the process where sometimes machine parameters have to be pushed to their limits as will be discussed in detail in [74].
Our process (Fig. 2.1) starts with cleaning the substrate sample that is cut from a semiconductor (Si or GaAs) or dielectric wafer (sapphire or alumina). The semiconductor wafers are factory covered with a thin passivation layer (typically SiO_2) of 17.5–500nm thickness. A layer of image reversal photoresist is then centrifugally spun onto the surface. For some experiments in which large trapping volumes are more important than small scale potentials with high gradients, the wire current is more important than the current density (Sect. 2.4.2). In these cases it is desirable to fabricate thick metal layers and, deviating from standard

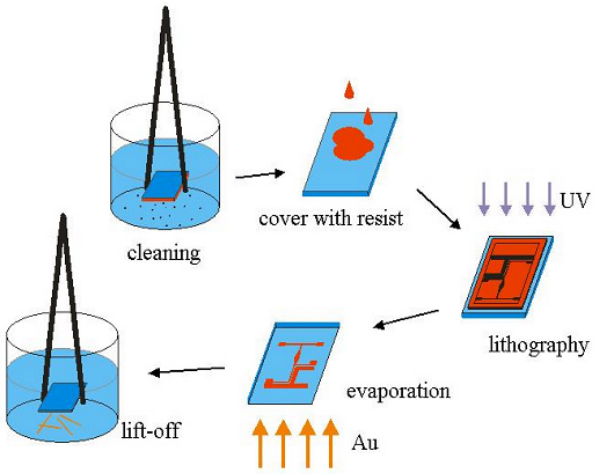

Figure 2.1: Schematic overview of the fabrication process (see text).

processes, also a thick photoresist layer is needed for the lithography. This is achieved by the use of a special photoresist that can be spun onto the surface at low rotation speeds. After exposing the chip to a pulse (0.9s) of ultraviolet light through an electron beam patterned mask and a standard development procedure, only a few lines of photoresist located at the future gaps in the metal layer remain.

The next step of evaporating metal (a 3-30nm tall titanium adhesion layer and an up to 5μm tall gold layer), is critical regarding the bulk and edge quality of the wires. Here, the relevant parameters (source–sample distance, evaporation speed, substrate temperature) have to be carefully controlled to obtain the smoothest structures possible. Finally, the remainder of photoresist is removed together with its metal cover, leaving a smooth gold mirror with fine gaps defining the wire and electrode structures on the chip. In some cases, the lithography was repeated with a second mask in order to increase the wire thickness even further. This technique is particular useful if structures of different sizes are to be integrated on a single chip because smaller features can simply be left out on the second mask. All the experiments presented in chapters 3 and 4 used such a double–layer chip. It should be noted, however, that the surface quality of the second (top) layer turns out be be slightly deteriorated with respect to the first (bottom) layer. This is clearly visible by the increased amount of laser light scattered off the double layer part of the chip.

Fig. 2.2 shows microscope images of typical details of our atom chips during and after the fabrication. The smoothness of the wires clearly exceeds that achieved in electro-chemical processes such as electroplating [51, 64, 130].

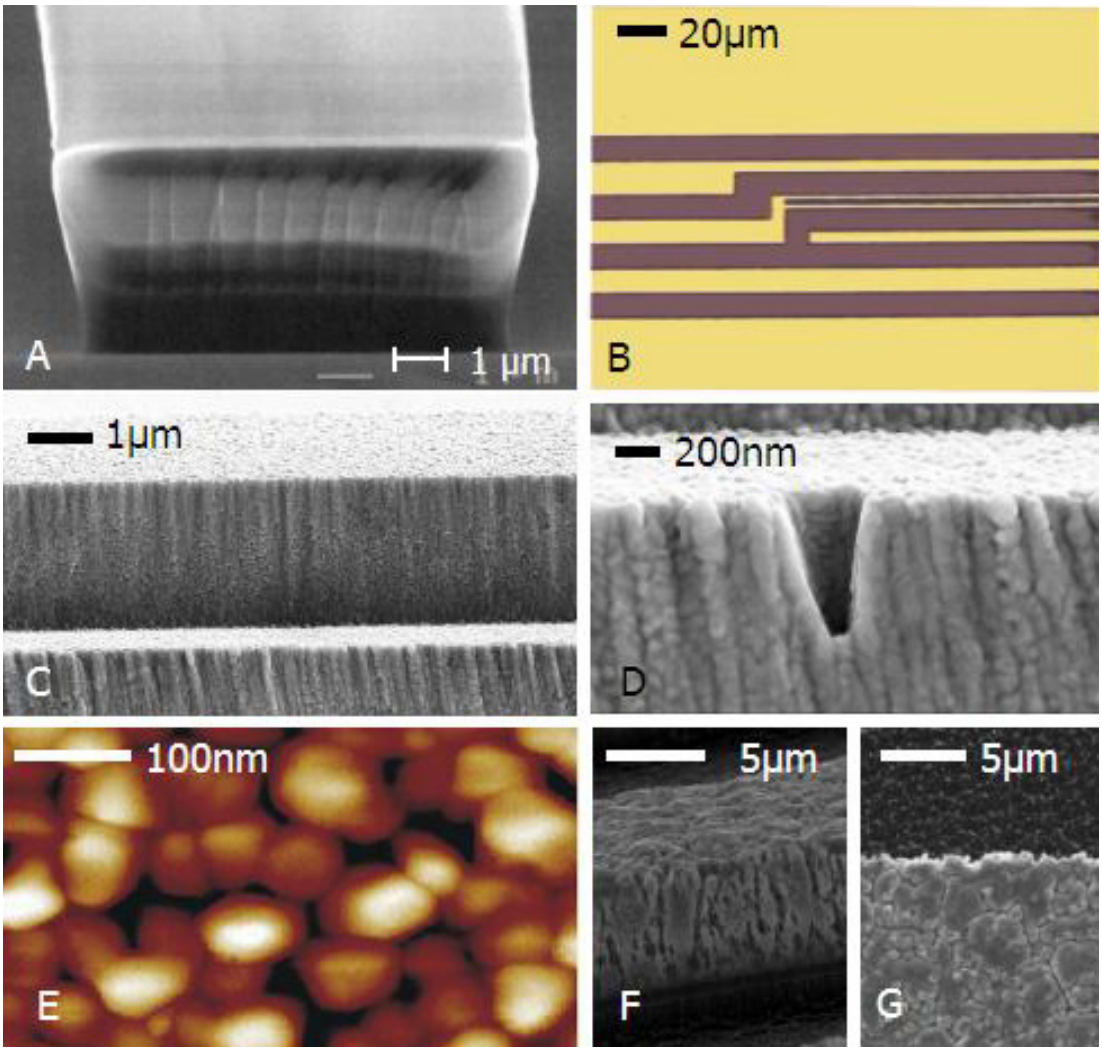

Figure 2.2: Microscope images of chip details during and after the fabrication. A: Scanning electron microscope (SEM) picture of the resist structure. Here, its thickness is 4.5μm, the undercut is 0.6μm. This slightly trapezoid form may lead to slightly thinner wires than intended in the chip design. B: Light microscope image of a detail of a fully fabricated chip. The gold wires have widths of 1, 5, and 10μm. C: SEM image of wire edges. In this case, two wires were fabricated on top of each other in a two-layer process. Hence two steps are visible. D: SEM image of a rare defect in a wire edge. Typically, edge and surface roughness are both < 100nm. E: Atomic force microscope (AFM) image of the gold surface. The grain size is 50–80nm. F: For comparison, an electroplated wire exhibits roughness on a much larger scale (SEM image). G: Top view of the edge of the same wire. F and G taken from [60].

2.3 Thermal properties

The earlier atom chip experiments were mainly meant to demonstrate the capability of atom chips to form complex manipulation potentials for atoms. In this case, it was often preferable to use large currents and fairly large distances from the surface to achieve large trapping volumes. This allows to capture many atoms and thus enhance signal to noise ratios in the demonstration experiments. As discussed earlier, the full scope of experiments at the quantum level becomes only accessible in steep potentials near the surface. As electric fields are mainly used to alter magnetic potentials, reaching the necessary voltages on the chips turns out to be not problematic. Even thermal atoms ($T \sim 100\mu$K) have been manipulated at fairly large (50μm) surface distances (Sect. 2.5) without relevant hardware limitations on the voltages. Colder atoms at lower distances are affected already by much lower voltages. Magnetic potentials are more critical: the relevant parameter here is the maximal current density j because the relevant trapping parameters scale with j (Sect. 2.4.2). In the following, the limitations of the maximal current density are discussed.
Substrate mounted wires (height H and width W) tolerate much larger current densities $j = I/WH$ than free standing wires. The heat deposited due to ohmic power dissipation $P = RI^2$ when a current I flows through a wire with resistance R is removed mainly through heat conduction to the substrate. Thus, the temperature rise and eventually the destruction limit of a wire not only depends on j during a current pulse of a certain duration τ but also on geometrical and material parameters of the assembly, i.e. heat conductivity λ and heat capacities (per volume) $C_{V;w}$ and $C_{V;s}$ of the wire and the substrate, respectively.
Typically the heat source (the wire) is separated from the thermally fairly well conducting substrate by a thin electrical and at the same time thermal insulation layer. This structure leads to two heat removal mechanisms on very different time scales.
The first process is the heat flow from the wire to the substrate through the insulation layer. In a one dimensional model, the timescale of this process is given by

$$\tau_{\text{fast}} = \frac{C_{V;w}H}{k - Hj^2\alpha\rho} \tag{2.1}$$

where k is the thermal conductance through the isolation layer, ρ the resistivity of the conducting material, and α the relative increase of ρ per unit of temperature change. For typical parameters of our chips, τ_{fast} is on the order of 1μs. Compared to timescales in microtrap experiments this time is so short that the temperature difference between wire and substrate

$$\Delta T(t) = \frac{Hj^2\rho}{k - Hj^2\alpha\rho}(1 - e^{-t/\tau_{\text{fast}}}) \tag{2.2}$$

saturates practically instantaneously.

The heat transport in the substrate is much slower: In a two dimensional model, a pointlike heat source is assumed on the surface a half space substrate. The temperature increase at this point is then given by the incomplete Γ function

$$T_s(t) = \frac{\rho I j}{2\pi\lambda}\Gamma\left(0, \frac{C_{V;s}W^2}{4\pi^2\lambda t}\right) \approx \frac{\rho I j}{2\pi\lambda}\ln\left(\frac{4\pi^2\lambda}{C_{V;s}W^2}t\right). \tag{2.3}$$

Here, the (small) temperature dependence of the resistivity is neglected. The logarithmic approximation is valid in the long time limit (for typical parameters already after $\sim 10\mu$s).
These two models reproduce the results obtained in a two-dimensional numerical calculation as long as the substrate can be treated as a heat sink. After a certain time (typically 100ms–1s), the heat transport out of the substrate has to be taken into account. At this stage, the heat transport along the direction parallel to the wire starts to play a role, too. In this case, the two-dimensional numerical calculation has to be modified to predict the wire heating quantitatively. The relevant timescale for the transport out of the substrate to become important is given mainly by the heat capacity of the substrate. A proper correction to the two-dimensional model can therefore be applied by altering the substrate size to match the three-dimensional wire to substrate volume ratio.
Figure 2.3 shows a comparison between the simple model outlined above, a corrected two-dimensional numerical calculation[1] for a realistic setup, and experimental data that was obtained in an extensive series of test experiments. For these measurements, we designed a special chip design containing a number of 2mm long wires of widths ranging between 2 and 100μm. This mask was used to fabricate test chips on various wafers with different substrate materials (sapphire, GaAs, Si) and different isolation layer (SiO_2) thicknesses (0, 25, and 500nm) between substrate and gold wires. After mounting the chip on a holder similar to the ones used in the regular experiments, current pulses of varying current and duration were applied to the wires and the increase in voltage drop was recorded. The change in resistance is a measure of the temperature of the wire.
The most important results of the test measurements are summarized in [75]. In general, the experimental data confirms the model [75, 74], and some important conclusions for (future) chip designs can be drawn from our model and the test measurements:
The main parameter for optimization is the maximal current density $j_{\max}$ that is supported by wires with small cross sections since this will allow to form steep traps with high spatial resolution. For sufficiently small $j \ll \sqrt{k/H\alpha\rho}$, the saturated temperature difference between substrate and wire (Eq. 2.2) simplifies to

$$\Delta T = \frac{H\rho}{k}j^2. \tag{2.4}$$

[1] The heat equation was numerically integrated with the generic partial differential equation solver FEMLab that is based on a finite element method.

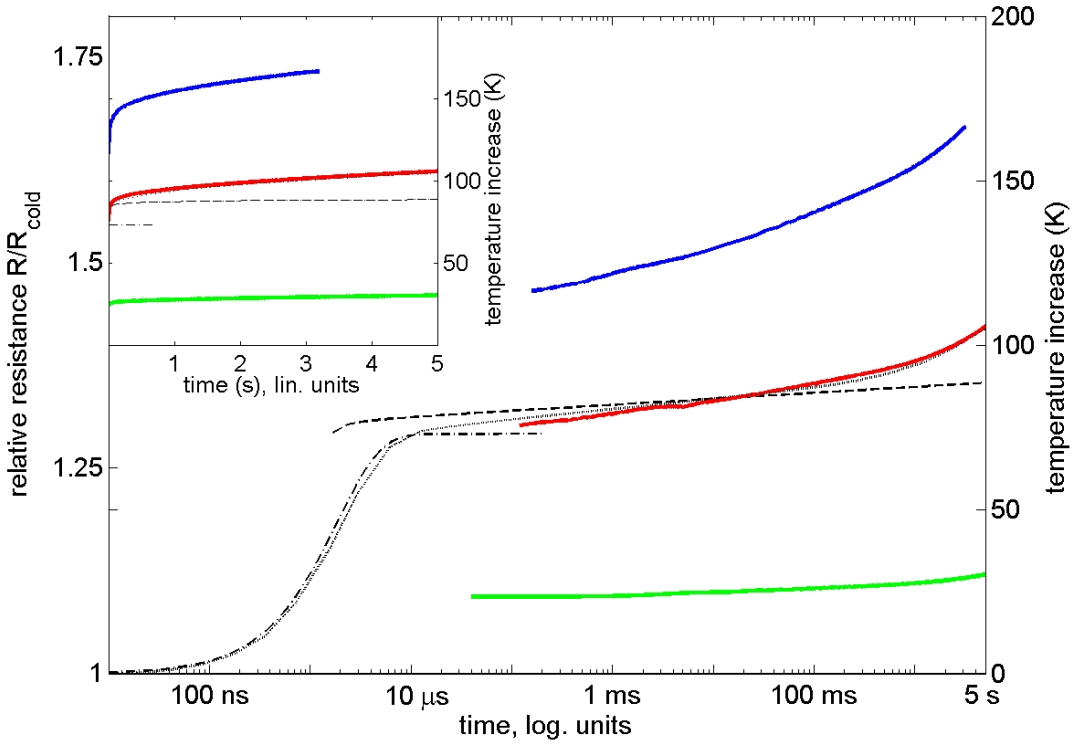

Figure 2.3: Temperature development of a 5μm wide, 1.5μm tall wire mounted on a 700μm thick Silicon substrate with a 500nm SiO_2 isolation layer. The colored thick curves show the measured resistances (normalized to the cold resistance) for 600mA, 500mA, and 300mA current pulses (top to bottom, blue, red, and green curves, respectively). In one case (500mA) also the theoretical predictions are shown. The initial fast temperature increase (dashed-dotted curve) happens on a μs timescale that was not resolved in the measurements. The analytically solvable model for the heat transport through the substrate (dashed curve) holds only as long as the approximation of a half space substrate is valid (for ∼100ms). If a two-dimensional numerical calculation is modified to correct for the finite heat capacity of the substrate, it reproduces the measurements to a high numerical accuracy. In the comparison between theory and experiment no fitting parameters were used.

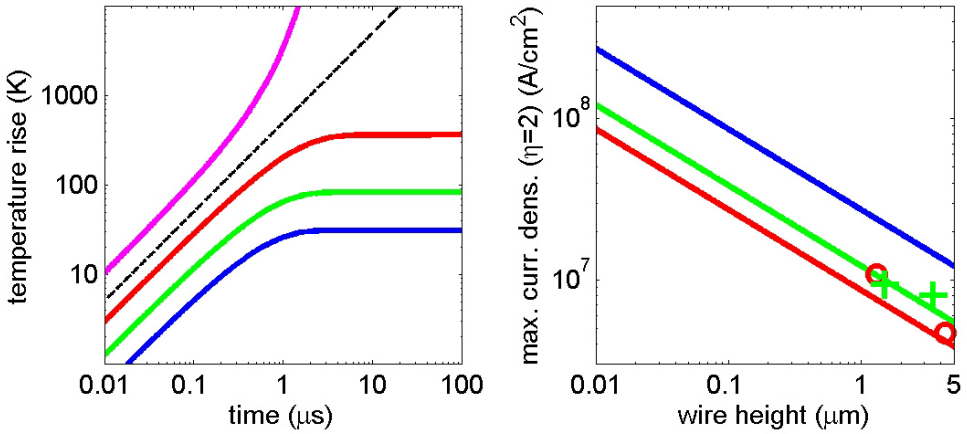

Figure 2.4: The maximal current density $j_{\max}$ supported by a wire is ultimately limited by the temperature dependent growth of resistivity at high j. (*left*) According to Eq. 2.5, the temperature rise saturates rapidly for sufficiently large $\eta > 1$ ($\eta = 3$ and $\eta = 2$ shown as blue and green curves, respectively). If η approaches unity (dashed line), saturation occurs later and at a higher equilibrium temperature ($\eta = 1.2$, red curve), $\eta < 1$ leads to an exponential heating of the wire ($\eta = 0.8$, magenta curve). This example is based on the tested parameters $H = 1\mu$m and $k = 5 \times 10^6 \mathrm{W/Km^2}$ for gold wires. (*right*) An extrapolation to small wire heights H shows that $j_{\max} > 10^8 \mathrm{A/m^2}$ should be safely sustained by a flat wire ($H = 10$nm) at observed values of k ($k = 5 \times 10^6 \mathrm{W/Km^2}, 2.5 \times 10^6 \mathrm{W/Km^2}$, green and red lines, respectively). The green crosses (red circles) mark values of j that have observed to leave relatively thick wires with a thermal contact of $k = 5 \times 10^6 \mathrm{W/Km^2} (2.5 \times 10^6 \mathrm{W/Km^2})$ intact. An improved thermal contact of $k = 2.5 \times 10^7 \mathrm{W/Km^2}$ (blue line) would lead to even larger $j_{\max}$. The calculations are based on the safe $\eta = 2$ ($\eta = 1.3$ would increase all values for $j_{\max}$ by $\sim 50\%$.)

In this case, the saturation time is given by $\tau = C_{V;w} H/k$. At larger $j \lesssim \sqrt{k/H\alpha\rho}$, the increased resistance and thus the increased power dissipation in the wire starts to play a role: ΔT saturates later and thus the saturation temperature scales more strongly with j. At $j \geq \sqrt{k/H\alpha\rho}$, the heat flow to the substrate cannot compensate the increasing power dissipation, and the wire temperature rises exponentially[2]. This will clearly lead to a rapid destruction of the wire. In our test measurements, we have observed current densities limited by

$$j_{\max} = \frac{1}{\eta} \sqrt{\frac{k}{H\alpha\rho}} \tag{2.5}$$

where the parameter η takes into account that wire is strongly heated at large j even before ΔT ceases to saturate and that the exact maximal sustainable wire temperature is in general unknown (Fig. 2.4). Empirically, we have found small values of η ranging between 1 and 2.

[2]This corresponds to $\tau_{\mathrm{fast}} < 0$ in Eq. 2.1

Eq. 2.5 implies that the value of k should be increased and H should be reduced in order to increase $j_{\max}$. Experiments with different thicknesses d of the (SiO_2) isolation layer between wire and substrate have shown that thermal contact resistances at the material interfaces become important for $d < 100$nm. So far, $k \approx 5 \times 10^6 \mathrm{W/m^2K}$ (equivalent to $d = 250$nm and perfect thermal contact at the interfaces) has been achieved but further optimization seems to be possible (for example by also reducing the thickness of the Ti adhesion layer). The reduction of H is not problematic regarding the fabrication process. A limit to the drive to flatter wires arises from considerations limiting the minimal distance of the trapped atoms to the surface as discussed in Sect. 4.2. Fig. 2.4 shows an extrapolation to flatter wires based on measured data for taller wires. As a result, current densities of several $10^8 \mathrm{A/cm^2}$ should be safely sustained by 10nm tall gold wires with realistic thermal contact to the substrate. This result agrees to data that has been measured for gold nanowires (cross section $\sim$ 100nm×20nm) [53]. Even in superconductors, higher current densities have not been achieved [192].

Though technically intricate, cooling the substrate [51] should further improve these values due to reduced material resistivity ρ. For gold ρ drops from $2.2\mu\Omega$cm to $0.45\mu\Omega$cm ($0.022\mu\Omega$cm) if the temperature is decreased from room temperature to liquid nitrogen (helium) temperatures (77K and 4K, respectively) [137]. According to Eq. 2.5, this would increase $j_{\max}$ by a factor of 2 (10) at 77K (4K). The relative influence of the slow heat transport in the substrate on the wire temperature after a current pulse of a given duration t is

$$\frac{T_{\mathrm{slow}}}{T_{\mathrm{fast,sat}}} = \frac{kW}{2\pi\lambda} \ln\left(\frac{4\pi^2\lambda}{C_{V;s}W^2}t\right) \tag{2.6}$$

for sufficiently low $j < \sqrt{k/H\alpha\rho}$. Large current densities are predominantly important for small wires, i.e. narrow wires (small W), so that an increase of k would typically be compensated by a reduction of W. Thus, $j_{\max}$ is indeed expected to be limited by the fast process for wires with small cross sections even for high current densities. For example, a current pulse of $j = 3 \times 10^8 \mathrm{A/cm^2}$ ($I = 30$mA) passed through a wire of a $W \times H = 1\mu$m×10nm cross section should cause a practically instantaneous heating of 110K while the additional slow heating would not exceed 50K after a pulse duration of 1s.

The reason for the small influence of the slow process on the heating behavior of small wires is that this heating depends on the total dissipated *power* that is proportional to I *and* j (not only j as for the fast process). This makes the heat flow in the substrate and out of the substrate the dominant mechanisms if chip wires are to be used to form deep traps with large trapping volume which require mainly large currents. Such traps are useful for the application of efficient evaporative cooling for the production of large BEC samples. Improvements over the current situation are possible if substrates with larger λ were used (for instance by increasing the doping in the Si wafers) or if the substrate thickness was

increased. The strongest effect, however, can be expected from a better thermal contact to a heat sink in the sample holder. The currently used material (MACOR, $\lambda = 1.5\text{W/Km}^2$) is a thermal isolator and will be replaced by Shapal ($\lambda = 100\text{W/Km}^2$). Ideally, a large cross section copper ($\lambda = 401\text{W/Km}^2$) connector should be brought into good thermal contact with the chip. This "cooling finger" should preferably be located in the center of the chip so that the heat produced at the chip center flows the shortest possible path to this heat sink. Such a holder is currently being developed.
A detailed account of the test measurements and a full analysis of the validity parameters of the presented heat dissipation model and numerical calculations will be given in [74]. This thesis will also include results of currently performed tests with very flat wires ($H = 20\text{nm}$) that are expected to sustain extremely large current densities well in excess of 10^8A/cm^2 (see above).
Finally, it should be noted that individual wires do exhibit individual properties. Slightly varying thermal contact resistances to the substrate that are equivalent to varying isolation layer thicknesses of $\sim 50 - 100\text{nm}$ have, for example, been observed. Therefore, it seems wise to monitor a wire's resistance at all times when a current is passed through it in the experiment. As a safety precaution during the actual experiments, we have never let the resistance of a wire exceed its cold resistance by more than 30% which corresponds to a temperature increase of 75K.
The following sections of this chapter are devoted to the different mechanisms of atom manipulation based on the microfabricated structures described above.

2.4 Magnetic fields

In the most general case, the interaction of magnetic fields and a neutral atom depends on the internal structure of the atom. If an external magnetic field varies on a scale typical of the extension of the atom, the coupling of the field to the nucleus and the electrons have to be treated separately. Such a situation may arise when atoms in highly excited Rydberg states are positioned in extremely inhomogenous fields. This case has been studied in detail in [127, 129, 128], and interesting effects such as a magnetic field gradient induced permanent electric dipole moment are predicted. Even though the atom chip environment provides the most extreme parameters available, only large gradients of $\sim 10^9\text{G/cm}$ require this type of treatment. Such strong field inhomogenities are not experimentally accessible at this time.
In current experiments, an approximation treating the atom as a pointlike neutral particle with a magnetic dipole moment $\boldsymbol{\mu}$ is fully valid. The (Zeeman) interaction energy arising from a (weak) external magnetic field ($\mathbf{B}$) induced perturbation is given by

$$U_{\text{mag}} = -\boldsymbol{\mu}.\mathbf{B} = \mu_B m_F g_F |\mathbf{B}| \tag{2.7}$$

where $\mu_B = h \times 1.4\text{MHz/G}$ is the Bohr magneton, g_F the Landé factor of the atomic (hyperfine) state, and m_F the projection of the atomic spin onto the external field direction. If the change of direction of $\mathbf{B}$ in the rest frame of the atom is slow on a time scale given by the precession frequency ω_{Larmor} of the spin around the field axis, an *adiabatic approximation* holds. In this case m_F is a constant of motion and the potential is simply proportional to the field strength $B = |\mathbf{B}|$ ($U_{\text{mag}} \sim B$). This essentially reduces the design of potential configurations to a design of a magnetic field configuration. Different internal atomic states will react differently to the field, and are typically categorized by the sign of the proportionality constant. *Strong field seekers* are drawn towards regions of high fields while *weak field seekers* are attracted towards field minima. The *Earnshaw* theorem [54] generalized to magnetic, electrostatic, and gravitational fields [200, 111] forbids (local) maxima of the field in source-free regions. Thus, there are no stable static trapping geometries for atoms in high field seeking states. Confining potentials for these atoms are only possible in dynamic situations, i.e. if, for example, orbiting atoms are repelled from the attractive singularity of the field creating object by a centrifugal barrier. This situation has been experimentally realized, and atoms have been observed to circle a current carrying wire in two-dimensional "Kepler"-like orbits [46]. An alternative method would be to dynamically vary the magnetic field in analogy to the electric fields in AC-Paul traps [154].
The situation is simpler if low field seeking atoms are trapped since the Earnshaw theorem permits local minima of the *modulus* of the magnetic field in free space. In this case, the dynamic change needed for stable trapping can be viewed as being provided by the spin of the atom that follows the direction of the static external field. The vast majority of magnetic trapping experiments uses low field seeking atoms. A disadvantage, however, arises from the fact that the low field seeking states are always metastable states that can decay to the energetically preferred anti-trapped high field seeking states (*Landau-Zener* transitions and *Majorana* spin flips). The transition rates depend mainly on the strength of the magnetic field at the potential minimum as discussed in Sect. 4.1.2. As a consequence, vanishing fields at the potential minimum should be avoided if ultracold thermal atoms and BECs are to be stored in a trap for a significant time.

2.4.1 Wire guides

Macroscopic magnetic traps are typically based on fields produced by large coils far away from the trapped atoms (usually placed outside the vacuum chamber containing the atomic ensemble). The coils are necessary in order to achieve appreciable trap gradients at macroscopic distances. The reason is that the field energy and thus power dissipation in the coils scales with distance. For some field configurations (for example the *Ioffe-Pritcard* trap used in conventional BEC-experiments [69, 162, 8]) straight rods partially replace coils and have to carry

hundreds to thousands of Amperes to provide the required atom confinement.
If a trap is designed to be located close to a current carrying wire, the situation is very different, and steep gradients and large trap curvatures and frequencies may be achieved at low field energies. At the same time, close proximity to current carrying wires allows to shape the potential essentially by shaping the wires. The resolution of potential tailoring is given by the atom-wire distance. These points make wire traps an attractive tool for atom manipulation on a microscopic scale. An alternative are highly structured permanently magnetic structures [96]. This approach is less flexible than the electro-magnets but has the advantage of securing quiet fields that are not disturbed by technical and thermal current noise (Sect. 4.1).
In the following, different types of wire guides, their properties and potential design considerations are discussed. Examples of experimental implementations are given in most cases.

2.4.2 Single wire guides and scaling laws

The simplest form of a wire based confining potential for atoms in low field seeking states is the *side guide*. In this configuration, the field of a straight current carrying wire is superimposed with a homogeneous external bias field $\mathbf{B_b}$. As the field of a (thin) wire decays as $1/r$ with the distance r from the wire, a non-vanishing component $B_\perp$ of $\mathbf{B_b}$ perpendicular to the wire will always compensate the wire field at some distance h. This leads to a two-dimensional quadrupole field confining the atoms along a line parallel to the wire. The field zero associated with the quadrupole shape of the potential can be lifted if $\mathbf{B_b}$ has a component $B_\parallel$ (*Ioffe-Pritchard* field) parallel to the wire. This basic configuration has previously been described in all details [36, 11, 29, 62]. Here, an example of an experimental realization (Fig. 2.5) and some important scaling laws are given. A convenient system of units for wire traps uses G for magnetic fields, μm for lengths, and mA for currents (the use of mm and A is equivalent). The natural constants are set to $\mu_0 = 4\pi$, $m_F g_F \mu_B = 1$, $h = 1$ and $k_B = 1$. In these units, energy, temperature, frequency, and field units are equated. The field of a current carrying wire is simply $B = 2I/r$. The basic scaling laws are:

- The *distance* of the trap minimum from the wire is given by $h = 2I/B_\perp$.
- The *gradient* at (near) the minimum is $\partial B/\partial r = B_\perp^2/2I = B_\perp/h = 2I/h^2$.
- The trap *frequency* scales as $\omega \propto B_\perp^2/I\sqrt{MB_\parallel} = B_\perp/h\sqrt{MB_\parallel}$.
- The *density of states* scales as $\rho(E) \propto E^{3/2}/\omega^2$ in the harmonic region of the potential and as $\rho(E) \propto E^{5/2}/(\partial B/\partial r)^2$ in the linear regions.
- The trapped *phase space volume* (number of bound states) scales as $I^2/\sqrt{B_\perp}$ in the two-dimensional quadrupole case ($B_\parallel = 0$).

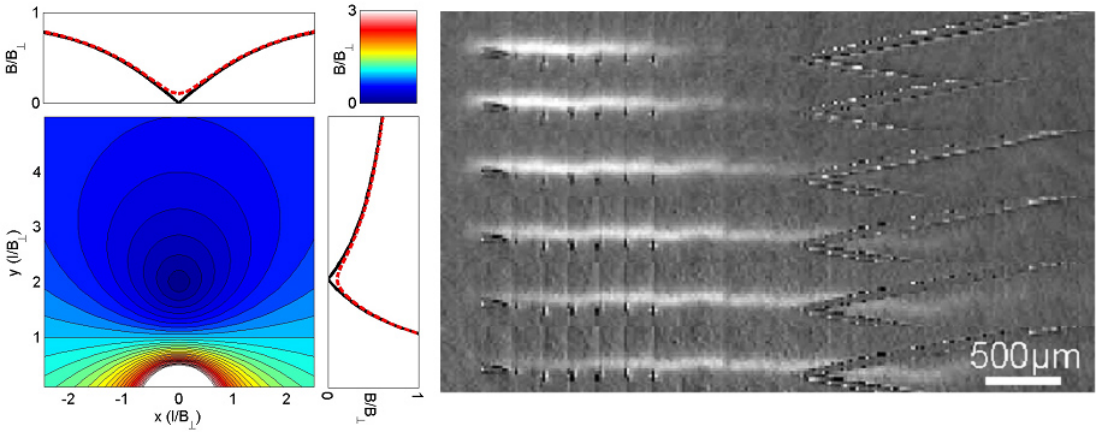

Figure 2.5: (*left*) Side guide: The contour plot shows equipotential lines in the plane perpendicular to the wire (located at the origin) in units of the orthogonal component of $\mathbf{B_b}$ (spacing $B_\perp/10$). This plot and the one-dimensional cuts through the potential minimum (black curves) are based on $B_\parallel = 0$. The field zero of this configuration can be removed by chosing $B_\parallel \neq 0$. The dotted red curves ($B_\parallel = B_\perp/10$) show how the trap bottom is lifted and becomes harmonic. (*right*) Time sequence (10ms) of fluorescence images of atoms released from a trap into a side guide. A small longitudinal magnetic field gradient causes a slow center of mass motion of the cloud to the right. The finite temperature ($\sim 100\mu$K) of this thermal ^{7}Li sample results in an expansion of the cloud along the unconfined longitudinal direction. The guide ends on the right hand side of the images where the guiding wire is broadened in order to guide the atoms to the chip surface (see Sect. 2.4.10) where they are lost by adsorption (*beam dump*).

M is the mass of the atom. For ^{7}Li (^{87}Rb) atoms in the $|F = 2, m_F = 2\rangle$ state, the proportionality constant for ω is $2\pi \times 44.8$kHz ($2\pi \times 12.7$kHz) (including the factor $\sqrt{1/M}$, valid for gradients in units G/μm).
The last equality for the trap gradient implies that the achievable steepness of a wire trap is determined by the maximally tolerated *current density* j in the wire. The reason is that the proximity of the trap to the wire center is limited by the wire size[3] (diameter) R, so that

$$\partial B/\partial r \propto I/h^2 \leq I/R^2 \propto j. \tag{2.8}$$

In Sect. 2.3 it has been shown that attaching wires to substrates strongly increases $j_{\max}$ and that small wires tolerate larger $j_{\max}$ than wires with large cross section. This means that miniaturization not only provides means for designing potentials with high spatial resolution but also stronger confinement than possible in macroscopic traps.

[3] All expressions given so far are based on an infinitely long, infinitesimally thin straight wire. The field of a wire with a circular cross section (diameter R) equals that of a thin wire located at its center for distances $r > R$. Finite size effects of realistic rectangular wires are discussed in Sect. 2.4.10.

On the other hand, large phase space volumes can only be trapped if larger *currents* are used. This is relevant for an initial collection of large atomic ensembles. It turns out that mm-sized structures provide a combination of strong confinement (j and h-dependent) and large trapping volumes (I-dependent) that is well suited for the production of sizable Bose-Einstein condensates in reasonably short cooling times (Sect. 3.1.2) [173, 197].

2.4.3 Two wire guides

The side guide is a powerful tool which is used in many applications. Modifications of this basic concept allow to form a variety of two-dimensional and three-dimensional (Sect. 2.4.8) trapping geometries with large parameter tuning ranges.

Slightly increasing the complexity by increasing the number of used wires, however, gives access to new classes of trapping and guiding geometries: A single additional wire already allows to form various types of beam splitters (Sect. 2.4.9) and more flexible guides [62]. Here, the basic properties of two-wire potentials are briefly discussed based on the simple case of parallel, infinitely long wires. In this case, the problem can be treated in two dimensions.

Horizontal bias fields

If the two wires carry *co-propagating* currents I, the field approximately equals that of a current $2I$ flowing through a single wire at the center between the two wires as long as the distance h from the wire plane is much larger than the wire separation $2d$. In the opposite limit $h \ll d$, the local fields of each of the two wires will dominate. Along the center line between the wires ($h = 0$), the total field cancels (quadrupole minimum).

A superimposed weak bias field $\mathbf{B_b}$ with a component $B_\perp$ orthogonal to the wires and parallel to the wire plane can now be used to form a second potential minimum in the quasi-single wire (side guide) regime ($h \gg d$). As $B_\perp$ is gradually increased, the first minimum moves away from the wire plane while the second minimum approaches this plane. If $\mathbf{B_b}$ has no component perpendicular to the wire plane, the two minima merge to a hexapole minimum for $B_{\perp,\mathrm{crit}} = 2I/d$ at a distance $h = d$ from the wire plane. If $B_\perp$ is increased further, the regime in which the local fields dominate is entered, and two separate side guides are formed, one near each wire. The potential configurations in the various regimes are depicted in Fig. 2.6. The detailed potential parameters and various dependencies can be found in [67].

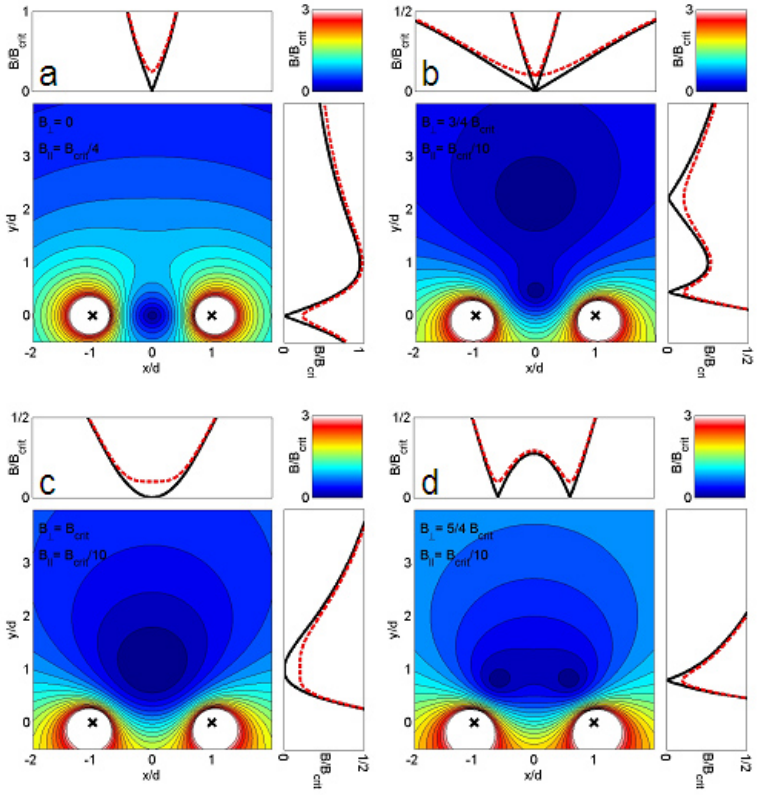

Figure 2.6: Potential shapes for two parallel wires carrying co-propagating currents. From a to d, the strength of the additional bias field is increased from zero to the over-critical value $B_\perp = 1.25 B_{\perp,\mathrm{crit}}$. The contour plots (contour spacing $0.15 B_{\perp,\mathrm{crit}}$, wire positions indicated as $\times$) as well as the one-dimensional cuts through the minima shown as black curves represent the $B_\parallel = 0$ case, the red dashed curves are calculated for $B_\parallel \neq 0$.

Vertical bias fields

Two parallel wires carrying *counter-propagating* currents produce a field that is directed *perpendicular* to the wire plane (chip surface). The strength of this field is $B_{v,\mathrm{crit}} = 4I/d$ in the wire plane and decays according to $4Id/(d^2 + h^2)$ with the distance h. Thus, a guide at variable h is obtained if a bias field $\mathbf{B_b}$ with a *vertical* component (normal to the wire plane) B_v is superimposed. Similar to the horizontal bias field case, two potential minima are formed (one above and one below the wire plane for $B_v < B_{v,\mathrm{crit}}$) that merge for $B_v = B_{v,\mathrm{crit}}$ in the wire plane. If B_v is increased further, two separate minima are again obtained, now located in the wire plane near each of the wires (Fig. 2.7).

For flat surface mounted wires, the atoms are lost from the guide when they hit the wire plane. In this case, the largest possible phase space volume is trapped if the guide is positioned at a distance $h = d$ ($B_v = B_{v,\mathrm{crit}}/2 = 2I/d$) from the wire

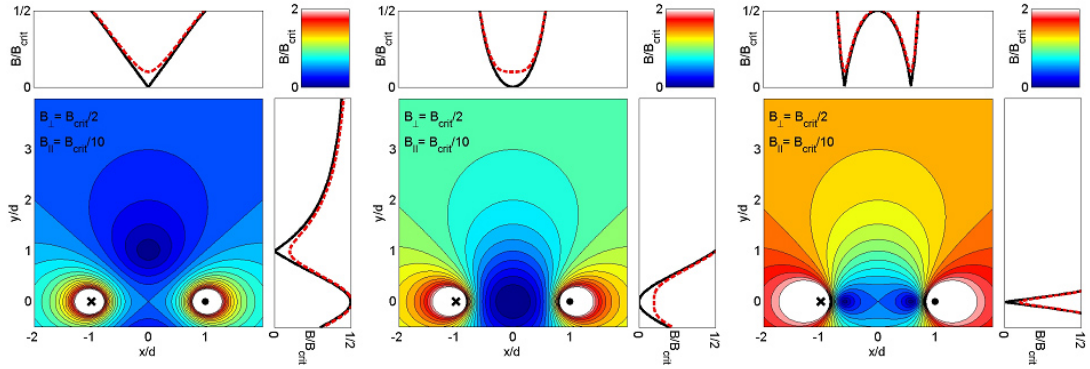

Figure 2.7: Two-wire guides based on counter-propagating currents and a vertical bias field. The wire positions are indicated as $\times$ and $\bullet$, depending on the current orientation. The bias field strength is increased from $B_{v,\mathrm{crit}}/2$ to $3B_{v,\mathrm{crit}}/2$ (left to right). The contour plots (contour spacing $0.1B_{v,\mathrm{crit}}$) and the one-dimensional cuts through the minima depicted as black curves illustrate the $B_{\parallel} = 0$ case in which the minima are quadrupole (hexapole in the center case of $B_v = B_{v,\mathrm{crit}}$) field zeroes. The red dashed curves show the effect of a non-vanishing longitudinal field component $B_{\parallel} = B_{v,\mathrm{crit}}/10$.

plane. In this configuration the potential barriers to the wire plane and towards infinity are equally high.

2.4.4 Multi-wire guides

More advanced and complex potential geometries can be realized if more than two wires are used. For example, in all of the above discussed configurations based on a single wire (Sect. 2.4.2) or two wires (Sect. 2.4.3), the bias fields used for controlling the trap confinement and distance from the surface can be replaced by one or better two additional current carrying wires. If the path of these wires is parallel to the actual guiding wire(s), a co-(counter-)propagating current flow will provide a horizontal (vertical) bias field. The advantages of such an arrangement are that external coils become obsolete and that the direction of $\mathbf{B_b}$ can be varied locally by appropriately shaping the wire paths. In addition, it is technically simpler to correlate current noises in the wires (for instance by a serial connection) than in wires and external coils. This type of *common mode* noise coupling can, for example, be used to ensure that the condition $B_{\perp} = B_{\perp,\mathrm{crit}}$ is met by construction and thus stable guiding in the hexapole minimum of a horizontal two-wire guide is possible.

An adequate treatment of the generalized N-wire case has been introduced in [43]. All currents are assumed to flow along straight, parallel, infinitesimally thin and infinitely long paths, thus allowing a reduction of the problem to two dimensions in a plane normal to the current paths.

By applying the transformations

$$\begin{array}{lcl} \mathbf{x} = (x, y) & \mapsto & \zeta := x + iy \\ \mathbf{B}(\mathbf{x}) = (B_x(x, y), B_y(x, y)) & \mapsto & \beta(\zeta) := B_x(\zeta) - iB_y(\zeta) \end{array} \tag{2.9}$$

to coordinates and fields, the two-dimensional problem is mapped to regular one-dimensional complex analysis. The field of N currents $I_1 \dots I_N$ at the positions $\zeta_1 \dots \zeta_N$ and a homogenous bias field β_b is simply given by the analytic function

$$\beta(\zeta) = \beta_b - 2i \sum_{j=1}^{N} \frac{I_j}{\zeta - \zeta_j} \tag{2.10}$$

(with the exception of the singularities at ζ_j). Even though the approximations made are typically not strictly valid for atom chip based (three-dimensional) microtrap potentials, a number of general properties and design rules can be derived:

- The number of potential minima is given by N if an external bias field is applied. These minima are quadrupole like field zeros, i.e. the field direction rotates by 2π as the minimum is circled and the potential rises linearly near the zeroes. The field gradient is direction independent.

- In special (unstable) cases, two or more minima can merge to a single hexapole or higher order zero (potential has harmonic (or higher power) shape at the minimum). The position of such a higher order minimum is already determined by locations ζ_j and magnitudes of the currents I_j. Only if the bias field exactly matches a critical bias field β_{crit}, the higher order minimum is actually obtained. Deviations result in a minimally remaining potential barrier of $|\beta_b - \beta_{\text{crit}}|$ between two quadrupole minima.

- All continuous parameter changes in β_b, I_j, ζ_j result in continuous changes in guide locations and potential gradients.

- Longitudinal field components $B_\parallel$ do not appear in the two-dimensional treatment. They can be applied externally and lift the zero fields at the potential minima. The potential shape near the minima then turns from linear to harmonic, from harmonic to quartic and so forth. The curvature of the harmonic potential is always given by $\partial^2 B/\partial r^2 = (\partial B/\partial r)^2/B_\parallel$, the frequency is propotional to $\omega_r \propto 1/\sqrt{B_\parallel}\partial B/\partial r$.

More details of the behavior of multi-wire guides and the underlying analytical calculations can be found in [67].
As an example of a multi-wire guide, we have used a four wire guide in our ^{87}Rb apparatus. Results of these experiments are shown in the section dealing with initial experiments with guided matter wave interferometers (Sect. 4.4).

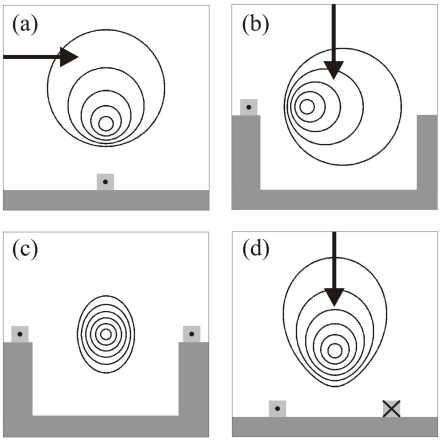

Figure 2.8: The *upper* row presents the potential for a side guide generated by a single wire and an external bias field (a) parallel and (b) perpendicular to the surface. The *lower* row presents the field configuration for a two wire guide with (c) parallel co-propagating currents and no bias field and (d) counter-propagating currents and an external bias field perpendicular to the plane containing the wires.

2.4.5 Curved wire guides

Access to trapping potentials near the full two-dimensional surface of an atom chip is facilitated by guiding potentials that do not depend on the guide's direction. In analogy to fibers used in light optics, it is desirable to make an omnidirectional matter wave guide (an 'atom fiber') available as standard tool. Such a tool allows not only to load and access individual traps in a two-dimensional trap array used, for example, as quantum bit register. With omnidirectional guides symmetric beam splitters (Sect. 2.4.9) and ring geometries that are important for guided matter wave interferometry (Sect. 4.4) can be formed. We have discussed various implementations of omnidirectional guides both conceptually and regarding our experimental implementations and those of other groups in [28].

It is immediately obvious that a planar guide can only be based on a bias field that has no component in the guiding plane because an in-plane component $\mathbf{B_p}$ would break the rotational symmetry (Fig. 2.8a). The varying angle between $\mathbf{B_p}$ and the guiding direction would directly translate into potential modulations. The tolerable remaining $\mathbf{B_p}$ depends on the temperature of the atoms to be guided and the maximal angular direction change of the guide.

As a consequence, a simple single-wire side guide can only be used with a vertical bias field B_v which forces the guide to be formed in the wire plane. Thus, the current carrying wire has to be mounted onto the chip substrate and be tall enough to allow for a sufficient guide-surface separation with a sufficiently high potential barrier so that losses and surface 'shaving effects' of hotter atoms are avoided. Alternatively, trenches can be etched into the substrate at desired guiding paths (Fig. 2.8b).

The situation for a two-wire guide with co-propagating currents is very similar. As a horizontal bias field cannot be used to control the guide's distance from the surface, the guide is necessarily formed in the wire plane (Fig. 2.8c). Some parameter tuning flexibility remains since the guide's position between the wires and the confinement can be varied by altering the ratio of the two currents.

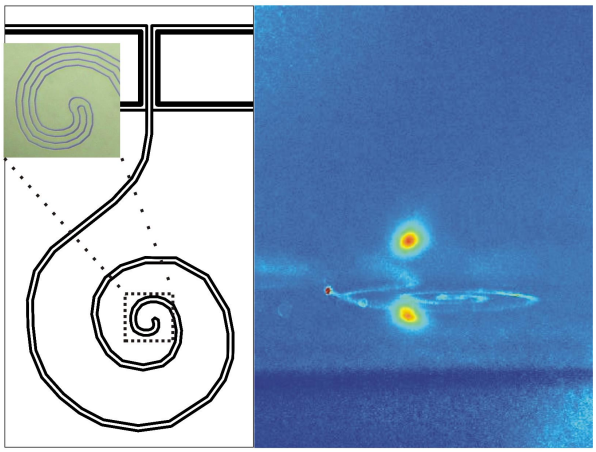

Figure 2.9: Omni-directional guide. (*left*) Chip design: The wires are shown as black lines, the white areas are grounded parts of the chip surface. The insert shows a microscope image of a detail of the spiral shaped wire guide. (*right*) Fluorescence of a magnetically trapped cloud and its reflection from the chip surface just before the guide is loaded. The guiding wires are visible through scattered imaging light.

In contrast, the two-wire guide with counter-propagating currents is particularly well suited for omnidirectional guiding because it is based on a vertical bias field B_v (Fig. 2.8d). In this case, the guide can be formed at various distances h from the surface, and the confinement can be controlled by tuning wire currents and B_v (Sect. 2.4.3). We have thoroughly tested the feasibility of this guiding configuration [133]. The results are summarized in the following section.

2.4.6 Demonstration experiment: the spiral guide

The first experimental realization of a curved wire guide was reported in [141]. In this experiment, atoms were deflected by small angles in a guide based on co-propagating currents. Later, a ring shaped geometry of two co-propagating currents was employed to guide atoms several times around a full circle [168]. The straight version of the more flexible counter-propagating current configuration has previously been used to guide a free falling atomic cloud [44].
In our experiment, we set out to demonstrate deterministic loading and actual guiding of atoms confined in a bent two-wire guide with counter-propagating currents. For this purpose, we designed a spiral shaped two-wire guide (Fig. 2.9). The two wires (width $\times$ height $= 45 \times 5\mu\text{m}^2$, center to center spacing $2d = 115\mu\text{m}$) are connected at the inner end of the spiral. This automatically leads to a counter-propagating current flow. The spiral shape was chosen in order to demonstrate the full flexibility of the guide by incorporating more than two full rotations with curve radii ranging from 200μm to 3mm along the 25mm long guiding path. The U-shaped wires (cross section $200 \times 5\mu\text{m}^2$) on either side of the straight beginning of the guide are used to form three-dimensional traps [62].
The starting point of our atom chip experiments is a reflection MOT [166] that contains a cloud of typically 10^8 cold ^{7}Li atoms located a few millimeters above the chip surface. Assisted by a U-shaped wire underneath the chip, the atoms are brought closer to the surface and transferred to a purely magnetic trap [61, 37].

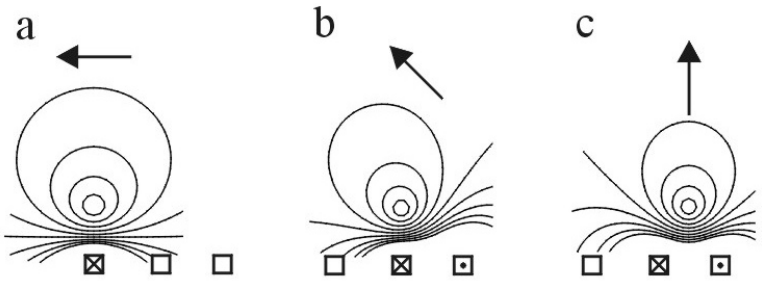

Figure 2.10: Potential configurations during the transfer of atoms from a single-wire guide with horizontal bias field (a) to a two-wire guide with vertical bias field (c). In each configuration, an arrow points in the direction of the bias field and three squares represent the three wires. The current flow is indicated by the symbols in the squares. A dot (cross) corresponds to a current flow out of (into) the shown plane, a blank square corresponds to zero current. In the intermediate stage (b), the currents run already exclusively through the two wires carrying counter-propagating currents while the bias field has been rotated by 45° with respect to the wire plane.

The wire traps for cooling and transfer use single wires and horizontal bias fields. We load the atoms to the spiral shaped two-wire guide by ramping down the current of the single wire after ramping up the counter-propagating currents in the two parallel wires of the guide. During this first step, the bias field is partially rotated so that the bending of the spiral wires still provides an endcap of the potential, thus confining the atoms in three dimensions. As depicted schematically in Fig. 2.10b, this intermediate configuration is reminiscent of the simple side guide (Fig. 2.10a) with only a slight perturbation by the current in the extra wire. In the final step, the rotation of the bias field is completed (Fig. 2.10c), and the atoms can expand freely along the spiral shaped path of the guide. Fig. 2.11 shows a time sequence of the fluorescence signal of atoms in the guide. The images are taken by exposing the atoms to a flash (100μs) of near resonant laser light. In order to avoid any disturbing reflections, the light enters the chamber from two directions parallel to the chip surface. Guiding of atoms was possible over a wide range of parameters. By varying the bias field strength B from 1G to 50G at a constant current of 1A through both (connected) wires, the height of the potential tube above the surface was scanned from 450μm to 35μm. The corresponding gradients ranged between 40G/cm and 8kG/cm for atoms in the $|F = 2, m_F = 2\rangle$ state. The parameter dependencies of gradients and distances are published in [62, 28]. The images and density profiles in Fig. 2.11 show the atom cloud expanding according to its temperature[4] and also moving as a whole along the guide. This center of mass motion is induced by a longitudinal

[4]The clouds exhibit an anisotropic temperature profile (450μK in the transverse, 50μK in the longitudinal direction) due to a transverse compression during the loading without rethermalization.

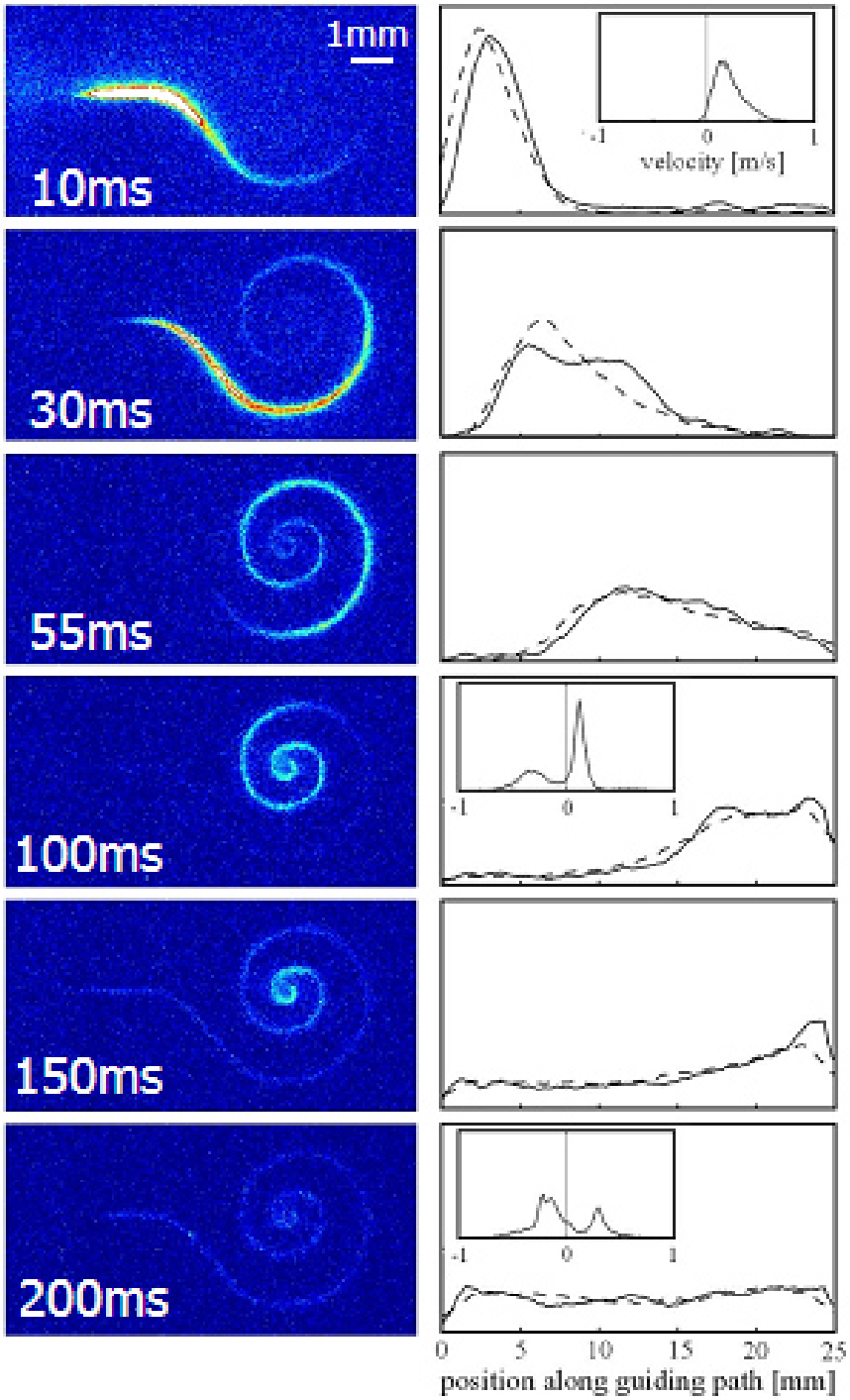

Figure 2.11: Time sequence of atoms released from the reservoir trap into the spiral shaped guide. (*left*) Fluorescence images. Atoms that have reached the end of the guide (center of the spiral) are reflected from a potential barrier and propagate in the backward direction. (*right*) One-dimensional density distributions along the path of the spiral, extracted from the experimental data and Monte-Carlo (MC) simulations (solid and dashed curves, respectively). In the inserts, the corresponding velocity distributions obtained by the same MC calculations are depicted. In these plots, a clear signature of the reflection is visible, the part of the cloud propagating backwards is clearly separated from that propagating in the forward direction.

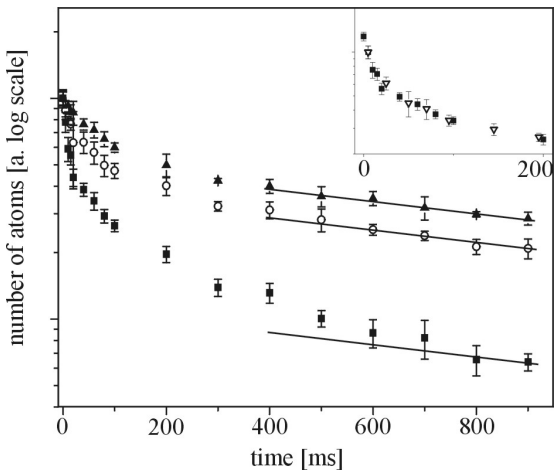

Figure 2.12: Lifetime graphs of three dimensional traps based on two counter-propagating currents in combination with a vertical bias field. Two different loss mechanisms can be distinguished in the time domain: An initial overexponentially fast process plays a role during the first $\sim$ 100ms; afterwards a slow exponential loss (time constant 1.6s, solid lines) stemming from collisions with the background gas dominates. Both the rate and amount of the fast loss depend on the depth of the trapping potential while the vacuum limited loss does not. The data were taken for traps with depths of 1250, 950, 500μK (triangles, circles, squares, respectively). The insert shows a comparison between the lifetime of a three dimensional trap (squares) and the guide (triangles) of approximately equal potential depth of 500μK.

field gradient produced by the current in the two leads from the beginning of the spiral wires to the connecting pads on the edge of the chip. By running a parallel current through another wire on the chip, we could even enhance this 'pushing' effect.

For a quantitative understanding of the density profiles, we have performed Monte-Carlo (MC) simulations of classical trajectories of particles in the guide. The results are depicted in Fig. 2.11 and show good agreement with the experiment. In particular, the reflections that occur when atoms reach the inner end of the guide are reproduced well. The effect of the reflection becomes most apparent in the plots of the velocity distributions extracted from the MC calculations (inserts). The velocity classes for forward and backward motion in the guide are clearly separated.

We have extensively investigated the lifetimes of the guided atom clouds and samples that were confined in three dimensional traps that were also based on vertical bias fields. The results are thoroughly discussed in [30] and [28]. A short summary is given here as well.

In our single vacuum chamber apparatus, the rest gas pressure is typically of the order of $\sim 10^{-9}$mbar, corresponding to background gas collision limited lifetimes of $\sim$ 1s as was confirmed in a conventional Z-trap (Sect. 2.4.8).

Direct lifetime measurements in the guide were only carried out for guiding times

of up to $\sim$ 200ms [5]. Indirect lifetime measurements were performed in three dimensionally confining potentials based on counter-propagating currents through two parallel wires. For this purpose we used the two U-shaped wires (Fig. 2.9) where the confinement in the longitudinal direction is provided by the wire leads. In these traps, the lifetime measured in the conventional Z-trap could be reproduced for the long trapping time regime (τ >300ms). For shorter times, the shape of the potential leads to a faster additional loss of the hottest atoms on a timescale of $\sim$ 100ms. This behavior was again confirmed by MC-calculations and will not pose a problem for colder atom samples. The measured results for different potential depths are depicted in Fig. 2.12. The comparison of the data obtained for the guide and for the three-dimensional trap (insert) shows complete agreement on the short timescale indicating the validity of the indirect measurements also for longer times.

2.4.7 Guiding BECs around curves: time orbiting potentials

The experiments with the spiral shaped guide have shown that a two-wire guide based on a vertical bias field allows a smooth transport of atoms along a curved barrier free potential tube. In spite of the quadrupole shape of the potential, Majorana spin flips (Sect. 4.1.2) did not play a role in the demonstration experiments with comparably hot thermal atoms. Eventually however, most experiments will rely on much colder and Bose-condensed atoms.
For bent guides the removal of the field zero at the potential minimum is not as straightforward as for a single-direction guide. An added Ioffe-field could not be constant anymore but it would rather have to be varied. A spatially homogeneous but time dependent field could be used if the extension of an atomic cloud along the guide is small. In this case, the Ioffe-field direction could be matched to the cloud's position.
A locally varying but static inhomogenous field configuration avoids involved timing sequences and more complex situations such as the guiding of two separated samples in the same guide at the same time are realizable. An implementation on a chip, however, is non-trivial since a field component along the guide can only be produced by a current flowing perpendicular to it, i.e. perpendicular to the guiding wires. This would either require multi-layer fabrication and a number of crossed wires or an adaptation of the transport mechanism demonstrated in [166]. This configuration is essentially a single layer approximation of a guide being crossed by periodically spaced perpendicular wires introducing local Ioffe-fields. The use of current sheets rather than thin wires would provide a smoother variation of the field that could possibly allow a static situation where the Ioffe-field magnitude is constant along the guide but the direction follows that of the

[5] Ohmic heating in the long guiding wires did not allow longer guiding times without risking damage to the wires.

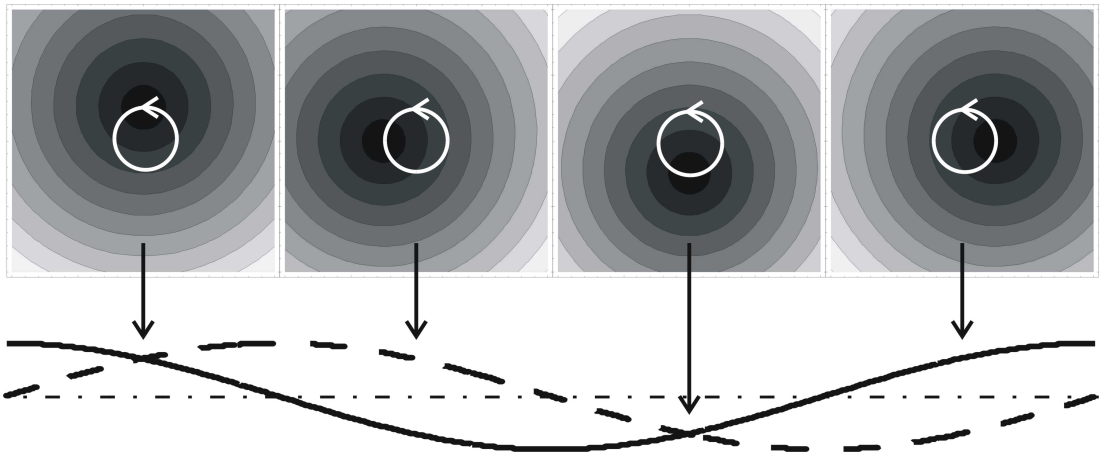

Figure 2.13: (*top*) Time sequence over one oscillation period of a time orbiting guiding potential. Darker shading corresponds to lower potential. (*bottom*) Each of the counter-propagating currents (solid and dashed curves) in two parallel wires is sinusoidally modulated around the steady current I_0 (dashed-dotted line). A relative phase difference of $\Delta\phi = \pi/2$ results in a quadrupole field zero circling around the minimum of the static situation (white arrows). With a proper choice of the modulation frequency, cold atoms are trapped in a time averaged potential. While the position of the potential minimum remains unchanged with respect to the static case, the atoms never encounter a magnetic field zero and thus do not undergo Majorana spin flips.

guide. Constraints regarding bending radii are likely to be unavoidable in this type of solution to the problem.
In [133] we have suggested a more flexible solution that appears to be simpler to implement experimentally. This solution is based on a periodical variation of the currents in the guiding wires themselves. A sinusoidal modulation of the currents according to

$$I(t) = I_0 + \sqrt{2} I_{\mathrm{mod}} \sin(\omega_{\mathrm{mod}} t + \phi) \tag{2.11}$$

in the two guiding wires with a relative phase difference of $\Delta\phi = \pi/2$ leads to a (nearly) circular motion of the quadrupole minimum of the guide (Fig. 2.13). As long as the modulation frequency ω_{mod} is slow with respect to the Larmor frequency ω_{Larmor} but fast with respect to the atomic oscillation frequency ω_{trap}, the atoms can be described as moving in a time averaged (orbiting) potential (TOP). Such TOP have successfully been used for the production of Bose-Einstein condensates [156]. The integrals for obtaining the average potential can generally only be solved numerically. In an ideal quadrupole field approximation the average field is given by elliptic functions whose Taylor expansion yields a parabolic leading term. Thus, the trap can be viewed as harmonic, and the definition of a trap frequency $\omega_{\mathrm{trap}}/2\pi$ is meaningful. If the height h of the guide over the wire plane is equal to the half distance d between the wires, the characteristic

frequencies of the trap simplify to

$$\omega_{\mathrm{Larmor}} = 2\pi \frac{B}{m_F} \frac{I_{\mathrm{mod}}}{I_0} = \frac{4\pi}{m_F} I_{\mathrm{mod}} d \tag{2.12}$$

and

$$\omega_{\mathrm{trap}} = \frac{1}{2}\sqrt{\frac{1}{2M}\frac{B^3}{I_0 I_{\mathrm{mod}}}} = \sqrt{\frac{1}{M}}\frac{I_0}{\sqrt{I_{\mathrm{mod}} d}}. \tag{2.13}$$

The radius of the circle of vanishing field ('circle of death') may be expressed in units of d or in units of the harmonic oscillator ground state size $a_0 = \sqrt{1/2\pi M \omega_{\mathrm{trap}}}$:

$$r_0 = d\frac{I_{\mathrm{mod}}}{I_0} = a_0 \sqrt{\frac{m_F}{2}\frac{\omega_{\mathrm{Larmor}}}{\omega_{\mathrm{trap}}}} \tag{2.14}$$

Thus, fulfilling the condition $\omega_{\mathrm{Larmor}} \gg \omega_{\mathrm{mod}} \gg \omega_{\mathrm{trap}}$, i.e. $\omega_{\mathrm{Larmor}}/\omega_{\mathrm{trap}} \gg 1$, will automatically ensure that the radius of the circle of death is much larger than the extension of a guided cloud in the ground state of the guide. For strongly interacting BEC clouds, the enlarged ground state may put a constraint on a minimal r_0 which would in turn automatically secure the above condition on the frequencies.
The depth of the TOP is given by the average fields at r_0 and at the center of the guide.

$$U_{\mathrm{depth}} = B_{\mathrm{TOP}}(r_0) - B_{\mathrm{TOP}}(0) = \left(\frac{4}{\pi} - 1\right)\frac{I_{\mathrm{mod}}}{I_0} B \approx 0.27 \frac{I_{\mathrm{mod}}}{I_0} B \tag{2.15}$$

The potential tuning range is large, a few example configurations and the resulting guide parameters are listed in table 2.1.
These parameters are calculated according to the above formulae. The deviations from the approximations used grow as the ratio I_{mod}/I_0 is increased, and as h/d deviates from unity. This can be observed in numerical potential calculations. The results of such calculations in the $h = d$ case are plotted for two different current modulation ratios (Fig. 2.14), Fig. 2.15 shows the corrections for the circle of death.

2.4.8 Trapping geometries

So far, only two-dimensionally confining, i.e. guiding, potentials have been treated. In this simple situation, the general properties of wire traps could be studied. Many experiments, however, are only possible if atoms are confined in all three spatial dimensions.
It has been mentioned that a bias field component $B_{\parallel}$ can be used to remove zeroes of the magnetic field at the trap minima. If $B_{\parallel}$ is inhomogeneous along a

d μm	B G	I_0 mA	I_{mod} mA	ω_{Larmor} $2\pi\times$MHz	ω_{trap} $2\pi\times$kHz	r_0 μm	U_{depth} $k_B\times\mu$K
1	40	20	3	4.2	150	0.15	110
1	40	20	5	7	110	0.25	180
1	40	20	8	11	90	0.4	290
10	20	100	4	0.6	20	0.4	15
10	20	100	10	1.4	13	1	37
10	20	100	40	5.6	6.4	4	150
50	20	500	10	0.3	5.7	1	7
50	20	500	50	1.4	2.5	5	37
50	20	500	200	5.6	1.3	20	150

Table 2.1: Realistic parameters for TOP two wire guides on atom chips. The resulting potential characteristics are calculated for ^{87}Rb atoms in the $|F=2, m_F=2\rangle$ state.

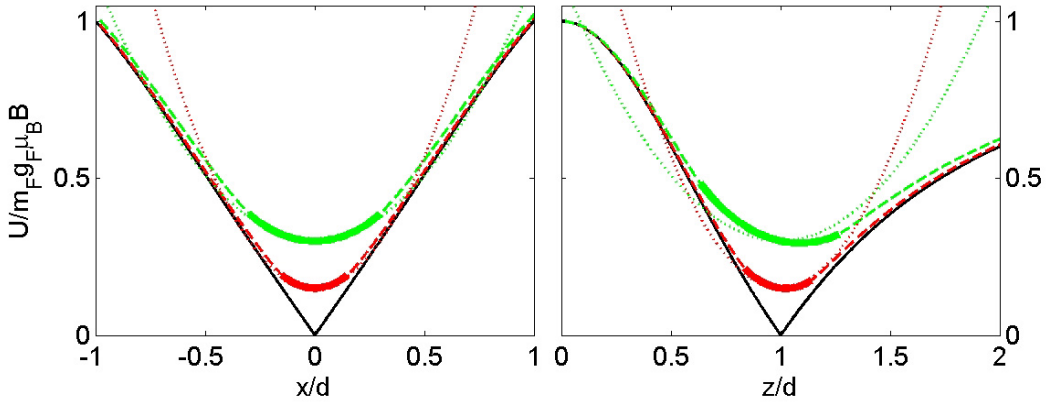

Figure 2.14: Numerical calculation of the TOP for the $d = h$ case for $I_{\mathrm{mod}}/I_0 = 15\%$ (red) and 30% (green). The potentials are plotted versus the position perpendicular to the wires with respect to the guide's minimum (left) and as a function of height over the wire plane (right). The length units are given in half wire separations d, the energy scale is given in units of the bias field B. Inside the circle of death, the potentials are depicted as thick solid lines, outside as dashed lines. For comparison, the harmonic approximation (equations 2.13 and 2.15)(dotted lines) and the static potential (black lines) are shown.

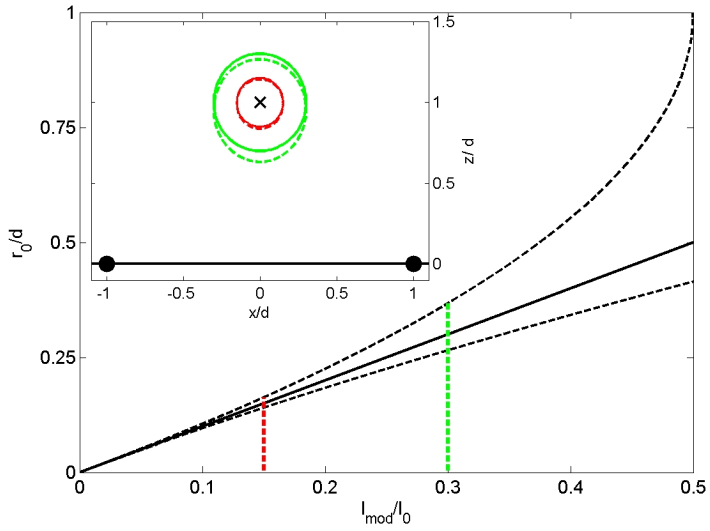

Figure 2.15: Deviations from the radius of the circle of death in a TOP guide according to equation 2.14 (solid line) from the values of vanishing fields obtained in a full calculation. The dashed lines show the maximal and minimal distances of the field zero from the (average) potential minimum as functions of the current modulation I_{mod}/I_0. In the insert all positions of vanishing field are plotted (dashed lines) for the two cases $I_{\mathrm{mod}}/I_0 = 15\%$ (red) and $I_{\mathrm{mod}}/I_0 = 30\%$ (green). For comparison, the circles with the radius r_0 taken from equation 2.14 are shown (solid lines). The wire positions on the chip surface (black line) are marked as black solid circles, the length scales are given in units of the half wire separation d. The guiding potential minimum (both for the static and the TOP case) is marked as a black cross.

guiding potential, it can also be used to provide the desired confinement in the longitudinal direction. Such a situation of a locally varying field in the thus far unused direction can be achieved by passing currents through additional wires or simply by bending the wire(s) providing the guiding potential.
There is an unlimited number of possible three-dimensional wire traps, and the exact trap parameters have to be calculated case by case. Typically, it is sufficient to use a 'stick model', i.e. to approximate the fields by adding the fields of infinitesimally thin straight current carrying wires of finite length (see Sect. 2.4.10 for validity considerations and corrections). In cylindrical coordinates, the field of a single wire piece of length L derived from Biot-Savart's law is given by:

$$\mathbf{B}(\mathbf{r}) = \mathbf{e}_\phi \frac{I}{\rho}\left[\frac{z_+}{\sqrt{\rho^2+z_+^2}} + \frac{z_-}{\sqrt{\rho^2+z_-^2}}\right]. \tag{2.16}$$

The wire extends from $-L/2$ to $L/2$ on the z-axis, the relative coordinates are defined as $z_\pm = L/2 \pm z$. In the limit of $L \to \infty$, the expression for an infinitely long wire is recovered ($\mathbf{B}(\mathbf{r}) = \mathbf{e}_\phi \frac{2I}{\rho}$). The resulting multi-wire expressions are of-

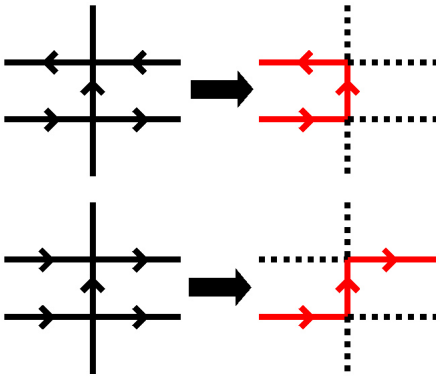

Figure 2.16: Basic configurations of three-dimensional traps. (*left*) Two parallel wires crossing a side guide wire ('H'-shape) can be used to introduce potential 'endcaps' by introducing inhomogeneous longitudinal field components. Depending on the relative direction of these two additional currents, a quadrupole (top) or a Ioffe-Pritchard (bottom) type trap is obtained. (*right*) These two trapping potentials are approximated by the commonly used single layer 'U'- or 'Z'-structures (top and bottom, respectively).

ten complex, and care has to be taken in the design because an added wire never only produces a single field component (for example the desired inhomogeneous $B_\parallel$ to provide 'endcaps' for a guiding potential). Since the various field contributions have to be added vectorially before the modulus is computed to derive the potential, the unintended additional field components may significantly alter the trapping potentials.
In general, magnetic traps may be categorized into *quadrupole* type traps with vanishing field at the trap minimum and *Ioffe-Pritchard* (IP) type traps without field zeroes. If a two-dimensional guiding potential is closed by an inhomogeneous $B_\parallel$, the type of the resulting three-dimensional trap depends on whether or not $B_\parallel$ changes its orientation (sign) within the trapping region.
One way of turning a side guide into a three-dimensional trap is to cross the guiding wire with two orthogonal 'endcap' wires ('H'-structure, Fig. 2.16). Co-propagating currents in the endcap wires result in an IP-trap as $B_\parallel$ rises near the endcap wires and drops in the center between them, but never changes its orientation. On the other hand, counter-propagating currents lead to the same effect regarding the field modulus near the wires but with reversed field orientation. Thus, the contributions cancel due to symmetry in the center between the endcap wires, and a quadrupole trap is formed.
The details of this prototype wire trap and the dependence of the trapping parameters on geometry, currents, and bias fields have been discussed elsewhere [173]. For practical reasons, it is often preferable to use approximations of the H-trap in the experiments. A 'U'- and a 'Z'-shaped wire in combination with a homogeneous bias field have become well established standard tools and are briefly introduced in the following paragraphs.

U-trap: A quadrupole wire trap

Bending a straight wire to a U-shape closely resembles the above discussed H-trap with counter-propagating currents (Fig. 2.16). The contributions of the two bent leads to $B_\parallel$ cancel in the center between them where the quadrupole field zero

is found. The transverse confinement is that of a regular side guide formed by the central wire piece of the U. The leads also produce vertical field components that add constructively in the center of U, and effectively rotate the bias field. Consequently, the side guide potential is rotated about the central wire of the U which can in turn be compensated by introducing an opposing vertical field component to $\mathbf{B_b}$. This compensation improves the trap properties, in particular the trap depth is enhanced. The specific parameters of the U-wire field are widely tunable by adjusting current, bias field, and geometry of the wire. In particular, the ratio of transverse and longitudinal gradients is controlled by the length L of the central wire and the distance of the trap from the wire h. A more detailed analysis has been performed many times, results may be found, for example, in [195].
The most important application of fields produced by U-shaped wires is to form the quadrupole field for collecting and cooling the atoms in the MOT. Originally, we used a simple silver wire ($\varnothing = 1$mm) bent to a U-shape and mounted directly underneath the chip in our ^{7}Li setup. Even though currents of up to 25A were tolerated by this wire and the trapping volume was accordingly large, the region of validity of the quadrupole field approximation near the field zero was too small to load a sufficiently large number of atoms directly into the *U-MOT*. Instead, the accumulation of many atoms was assisted by a pair of massive coils ($\sim$ 2000A windings each). A large cloud of atoms could then be transferred to the U-MOT which was directly transformed to a U-magnetic trap by extinguishing the MOT-light (see appendix A). Here, it is essential that the axis of the U-quadrupole field coincides with that of the coils and that necessary for a reflection MOT, i.e. an axis that is inclined by 45° with respect to the mirror (chip) surface.
For our ^{87}Rb setup we improved the U-structure to resemble the ideal quadrupole field over a larger volume, thus facilitating the initial collection of atoms in the MOT. In fact, we were able to discard the quadrupole coils altogether (Sect. 3.1.1) [197].

Z-trap: A wire based Ioffe-Pritchard trap

The most widely used wire trap of the Ioffe-Pritchard type is the Z-trap. Bending a side guide wire to a Z-shape approximates the H-trap with co-propagating currents in the endcap wires (Fig. 2.16). In this case, the contributions of the leads to the vertical field B_v cancel in the trap minimum that is hence found directly above the wire (if $\mathbf{B_b}$ itself is oriented parallel to the wire plane). However, B_v is non-zero at all off-center longitudinal positions and changes orientation at the minimum position. This effect leads to a rotation of trapped clouds about an axis through the minimum, normal to the wire (chip) plane. Consequently the natural coordinate system of the Z-trap is rotated with respect to the natural wire coordinate system. Typically, all trap parameters are expressed in terms of the coordinates given by the trap eigenaxes.

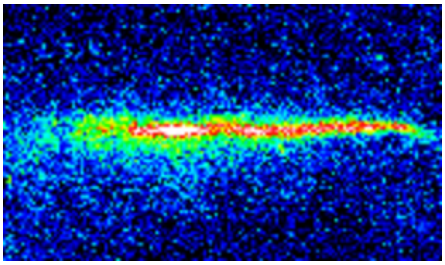

Figure 2.17: In situ fluorescence image of a cloud of thermal ^{7}Li atoms trapped in an elongated Z-trap based on a wire with a cross section as small as $1 \times 1 \mu m^2$ [195]. This wire tolerated a current density of $> 1.5 \times 10^7 A/cm^2$, and atoms could be trapped down to distances of 6μm from the wire (chip) surface.

As for the U-trap, the Z-trap is similar to the side guide regarding transverse confinement. The longitudinal confinement is tuned mainly by choosing the length of the central wire L and the distance of the trap from the wire plane h. In particular, the shape of the potential along the longitudinal trap axis is gradually transformed from harmonic to box-like as the wire plane is approached (as the ratio h/L is decreased). Since the $B_\parallel$-component of the wire field does not change its orientation along the trap, a homogeneous component $B_\parallel$ may be added or subtracted to adjust the field at the trap minimum (trap bottom) and hence the transverse trap frequency and extension of the harmonic part of the potential. Thorough studies of the Z-trap, both theoretically and experimentally, have been performed [78, 174].
The manipulation of (comparably hot) thermal ^{7}Li atoms was insensitive to Majorana spin flip (Sect. 4.1.2) losses in regions of small or vanishing fields. Here, the use of a Z-trap was intended to demonstrate and characterize [78, 80] the potentials (Fig. 2.17). For the evaporative cooling and manipulation of ultracold and BEC ^{87}Rb atoms, however, it is crucial to avoid too small fields throughout the trap in order to suppress large loss rates due to Majorana spin flips (Sect. 4.1.2). We have employed mostly Z-traps and sometimes closely related more complex geometries to produce our samples at $T \sim 1 - 10\mu$K and BECs in the experiments presented in chapter 3.

X-trap

Even though it has not directly been used in the experiments in the framework of this thesis, a third basic configuration should be mentioned here: a simple intersection of currents (X-shaped cross) at a right angle in combination with an appropriate bias field $\mathbf{B_b}$. Again, one of the wires forms a side guide which is modulated by a longitudinal field. Here, this field is produced by the second wire. Atoms are trapped if the longitudinal component $B_\parallel$ of $\mathbf{B_b}$ is large enough to overcompensate this field since the resulting total field will be minimal at the closest approach to the wire intersection. The difference between the homogeneous and inhomogeneous contributions to $B_\parallel$ will determine the field strength at the trap minimum.
This simple configuration may be scaled to a two-dimensional array of traps formed by a grid of wires. A prerequisite for such a configuration is a double

layer fabrication technology. A single-layer approximation has been used to dynamically vary the currents in a number of wires arranged orthogonally near a side guide wire. A controlled transport of a cloud of thermal atoms [83] and BEC [82] using proper timing of these currents has been demonstrated.
Note that the Z-trap is equivalent to an X-trap for sufficiently large $d > L$ since the field of the two Z-leads closely resembles that of a single wire in the middle between the leads (cf. Sect. 2.4.3).

2.4.9 Splitting geometries

One of the basic tools in optics is a beam splitter. Beam splitters also play an important role in integrated matter wave optics. They are necessary to distribute atomic clouds, for example to fill the individual sites of an array of traps. If a coherent splitting of matter waves is possible, however, many new and more interesting possibilities arise: Interferometers can be built and used for a great variety of applications ranging from high precision acceleration sensors to fundamental investigations of decoherence mechanisms near surfaces. Coherent beam splitters also allow to envision experiments studying inter-atomic quantum correlations (entanglement).
While the coherence of the splitting remains to be proven in future experiments, a number of wire-based splitting geometries has been developed and tested in the laboratory. Here, a summary of different approaches and some experimental examples are given. First, beam splitters in the time domain are described, i.e. splitting inside a trap via change of an external parameter (typically the bias field). The following part of this section is then devoted to spatial beam splitters which split the atoms (clouds of atoms) as they move along a guiding potential. Interferometers are discussed in chapter 4, Sect. 4.4.

Time dependent beam splitters

A rather simple configuration, the *split Z-trap*, exploits the inhomogeneity of $B_{\parallel}$ in a Z-trap. It has been mentioned above that an external bias field component $B_{\parallel}$ can be used to tune the field strength at the trap minimum. In particular, the component $B_{\parallel,\mathrm{wire}}$ of the wire field can be compensated at the minimum by subtracting a homogeneous field with a longitudinal component $B_{\parallel,\mathrm{hom}}$. For BEC experiments, it is necessary to choose $B_{\parallel,\mathrm{wire}} > B_{\parallel,\mathrm{hom}}$ in order to avoid spin flip losses at the field zero in the trap. However, thermal atoms tolerate field zeroes for a certain time (depending on cloud size and temperature and specific trap geometry). Choosing $B_{\parallel,\mathrm{wire}} < B_{\parallel,\mathrm{hom}}$, i.e. overcompensating the wire contribution to $B_{\parallel}$ leads to a formation of two quadrupole minima in the trap, i.e. a double well potential. A beam splitter can now simply be implemented by ramping $B_{\parallel,\mathrm{hom}}$ up. The potential shape and the corresponding behavior of an atomic cloud are depicted in Fig. 2.18.

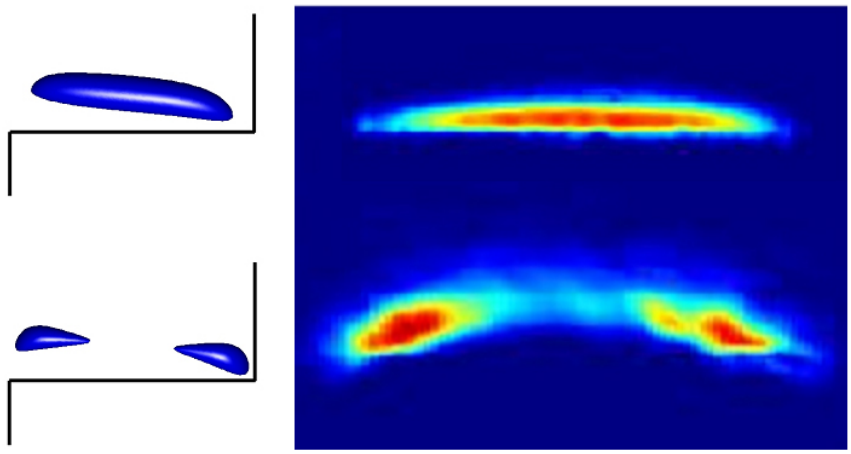

Figure 2.18: A thermal atom cloud confined in a Z-trap can be split by overcompensating $B_{\parallel,\mathrm{wire}}$ with a stronger $B_{\parallel,\mathrm{hom}}$. (*left*) Typical equipotential surfaces for the combined (top) and split (bottom) case. (*right*) Demonstration experiment with thermal ^{87}Rb atoms. The in situ absorption images (appendix B.5) are taken from the direction parallel to the wire plane and perpendicular to the center wire of the (copper wire) Z-trap (Sect. 3.1.2).

A slightly more complex geometry allows to avoid the appearance of field zeroes in the split Z-trap scheme. The additional inhomogeneity of $B_\parallel$ needed to transform a single well into a double well potential can be introduced by an extra wire crossing the side guide wire (central part of a Z-wire or H-structure [83]). Ramping up the current in this wire will gradually raise a barrier in the original trap. This *crossed wire* beam splitter scheme can be generalized to a chain of X-traps where individual traps or barriers (depending on wire currents and external contributions to $B_\parallel$) can be tuned by adjusting the individual currents.

Another type of beam splitter utilizes the above described geometry of two wires with co-propagating currents (Sect. 2.4.3). Splitting can be realized simply by varying the horizontal component $B_\perp$ of the bias field around $B_{|,\mathrm{crit}}$. In order to truly merge the minima and split them into two indistinguishable ones, extreme care has to be taken to zero the vertical bias field component B_v. Fig. 2.19 illustrates how the critical point of merged minima (hexapole minimum) is missed for different small B_v. This problem may be circumvented if the bias field is produced locally by additional wires. These extra wires can be accurately positioned and the currents can be driven in a common mode configuration to secure $B_v = 0$.

We have demonstrated splitting and recombination of a cloud of ^{7}Li atoms in an experiment with a trap based on two U-shaped wires (Fig. 2.20) [195, 62]. The leads of the U-wires confine the atoms in the longitudinal direction in much the same way as for a single U-wire (Sect. 3.1.1).

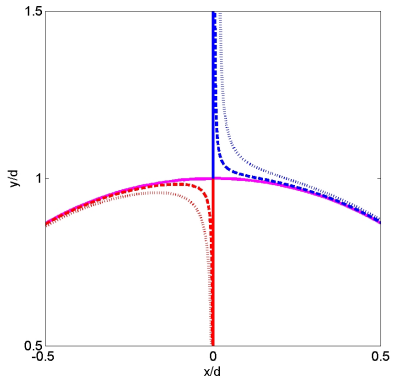

Figure 2.19: Imperfections of horizontal splitting. The path of the upper (lower) minimum are shown as blue (red) trajectories as the bias field $\mathbf{B_b}$ is increased. Only if the vertical component B_v of $\mathbf{B_b}$ vanishes, the two minima truly merge (solid lines) for $|\mathbf{B_b}| = B_{\perp,\mathrm{crit}}$ and separate horizontally along indistinguishable paths (magenta) at larger fields. The dotted (dashed) trajectories are plotted for a residual $B_v = 0.02 B_{\perp,\mathrm{crit}}$ ($B_v = 5 \times 10^{-3} B_\perp$).

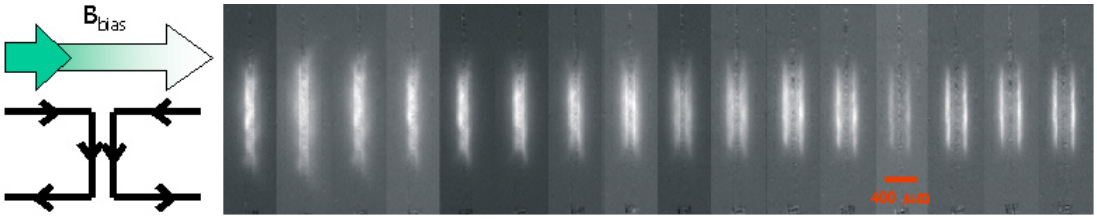

Figure 2.20: (*left*) Two U-shaped wires with co-propagating currents in the central wires together with a horizontal bias field form a single trap that is gradually transformed to a double well potential as the bias field strength is increased. (*right*) Fluorescence images of a cloud of ^{7}Li atoms that is split into two as the bias field is increased (from left to right). The wires used in this experiments have a cross section of $200 \times 1.1\mu\mathrm{m}^2$, the central wires are 1.6mm long and their distance is 360μm (center-center). At a current of 2A flowing through each of the wires, $B_\perp$ was scanned from 4 to 44G ($B_{\perp,\mathrm{crit}} = 22.4$G) to obtain the results shown here. The process could also be reversed, thus simulating an interferometer sequence.

Guided matter wave beam splitters

An alternative to time dependent beam splitters are *spatial* beam splitters that split propagating matter waves in analogy to beam splitters known from optics. The simplest version of a *guided* matter wave beam splitter, a Y-shaped wire that splits an incoming atomic cloud into two, has been tested earlier in this group [37, 120]. The Y-configuration has been studied theoretically in quantum electronics [152, 193]. Similar wave guides have been used experimentally in photon and electron interferometers [31].

The design of split wire guides with a single or multiple spatial input ports and two or more output ports may be based on the above considerations concerning multi-wire guides (Sect. 2.4.4). In general, N wires in combination with a bias field will form N guiding minima. This implies that in any configuration with merging wires, a channel will end at the merging point. Such a loss channel exists in the simple case of a single wire that is split into two in a Y-shape (Fig. 2.21A). In the experiments with comparably hot ^{7}Li atoms, losses through this small

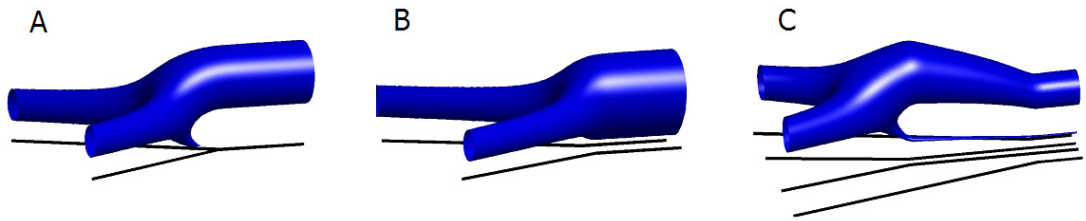

Figure 2.21: Y-beam splitter configurations for guided matter waves. The contour plots show different wire geometries and typical equipotential surfaces. A: The simple configuration of splitting a side guide wire into two has been tested experimentally [37]. The stronger confinement in the two output guides and the appearance of a loss channel to the surface are disadvantages of this configuration. B: The loss channel can be removed by using a two wire input guide (parallel currents), thus avoiding wire mergers that cause loss channels. C: A vertical bias field four wire (alternating anti-parallel currents) beam splitter is a truly symmetric beam splitter, even if a longitudinal bias field component $B_{\parallel}$ is introduced.

channel were unimportant. For colder atoms these loss channels pose a problem, and wire junctions should hence be avoided. Fig. 2.21B shows an improved configuration in which two parallel wires are bent off to form a Y-like structure without wire junctions. Depending on the bias field strength $B_{\perp}$, two vertically separated incoming guides merge near the forking point and split horizontally. If $B_{\perp} = B_{\mathrm{crit}}$, a single (unstable) hexapole guide is split horizontally.

In the two presented beam splitters the confinement differs between the input and the output guides because the (effective) current in the input guide wire(s) is twice as high as in each of the output guide wires. This may lead to reflections from the splitting region. More importantly, the horizontal bias field breaks the symmetry of the splitting as soon as a component $B_{\parallel}$ is introduced to avoid Majorana spin flips (Sect. 4.1.2). For this reason, we have chosen to use beam splitters based on vertical bias fields B_v. The minimal number of wires in this case is four since two wires are needed for each output arm of the beam splitter. Fig. 2.21C illustrates the geometry and the potential, an experimental test with ^{87}Rb atoms in an interferometer configuration is presented in chapter 4 (Sect. 4.4). The parameter set chosen for this plot (and for the experiments) is far from the special case of a single hexapole minimum in the input guide because any instabilities in the bias field would lead to an uncontrolled splitting and hence ill-defined evolution of propagating matter waves. However, the additional, unused input guide may give rise to disturbing reflections and unwanted propagation from the original input guide into the extra channel.

This behavior is a consequence of general wire guide properties: The position, i.e. the type of splitting (horizontal or vertical), of the N guiding minima of N wires depends on the bias field strength relative to certain critical values. The effect of bias field changes in parallel wire configurations has been discussed above (Sect.

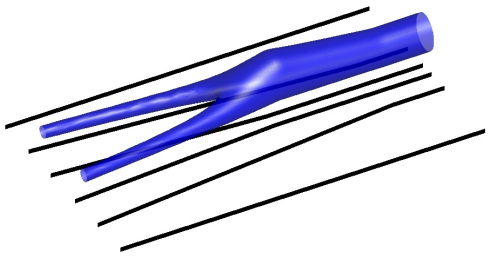

Figure 2.22: Multi-wire configurations can replace all external bias fields. This has the advantage that the trap parameters can be tuned by designing the appropriate robust geometry. In the example shown here, a six wire beam splitter is formed by equal currents in alternating directions. The geometry ensures that the input guide is in a stable hexapole configuration.

2.4.3). Equivalently, the wire distance(s) d can be varied spatially along the direction of atom propagation. The number of spatial input channels of this kind of beam splitter is equal to the number of output channels unless the bias field exactly equals a critical field. In such a case two or more input channels merge to a higher order potential minimum. Stabilizing this special situation requires accurate control over the bias field (see above). The usage of 'on board' bias fields , i.e. bias fields that are produced locally by additional wires greatly facilitates the fulfillment of this requirement. The extra wires can be connected in series with the guiding wire(s) and thus carry equal currents. If the wire separations are chosen appropriately, the critical condition is met for an arbitrary wire current. An example beam splitter is shown in Fig. 2.22. The quantum behavior of generic Y-beam splitters is discussed in Sect. 4.4.

A different possible beam splitter geometry relies on the tunnelling effect: Two separate wires are arranged to form an X, where both wires are bent at the position of the crossing in such a way that they do not touch (Fig. 2.23). An added horizontal bias field $B_\perp$ forms two side guides that are separated by a barrier that can be adjusted to be low enough to raise the tunnelling probability considerably at the point of closest approach. If the distance between the wires becomes so small that $B_\perp = B_{\perp,crit}$, the barrier vanishes completely, resulting in a configuration that is equivalent to a combination of two Y-beam splitters [142]. The choice of the parameters in the wire geometry, the wire current and the bias field govern the tunnelling probability and thereby the splitting ratio in this type of beam splitter. The relative phase shift between the two split partial waves in a tunnelling beam splitter allows to combine two beam splitters to form a Mach-Zehnder interferometer. Another property of the X-beam splitter is that the potential shape in the inputs and outputs stays virtually the same all over the splitting region as opposed to the Y-beam splitter. A detailed analysis of the tunnelling X-beam splitter can be found in [4].

2.4.10 Rectangular wires

To conclude this section on magnetic tools for micro-manipulation of atoms, the realistic situation of a finite wire size is discussed. Deviations from the fields

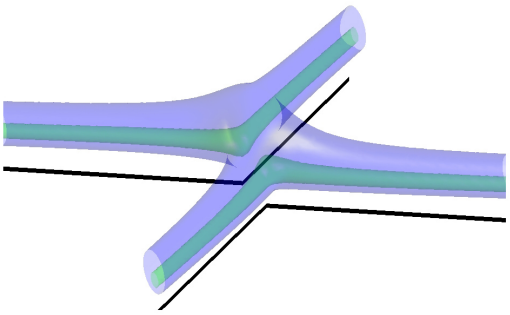

Figure 2.23: X-beam splitter based on tunnelling. The barrier between the two side guides at the point of closest approach of the guiding wires (black lines) is small enough to allow tunnelling. Equipotential surfaces at small energies (green) are separated while the two guiding potentials merge at higher energies (blue).

calculated for infinitesimally thin structures start to play a significant role as soon as the distance from the structure is on the order of the structure size or smaller.
All wires fabricated on our atom chips have rectangular cross sections. The field of a current flowing homogeneously through an infinitely long wire with a width W and a height H ($j = I/HW = \text{const.}$) can be calculated analytically. The components of the field (x-axis in the W-direction, y-axis along the H-direction, origin in the wire center) are given by

$$\begin{aligned} B_x(x,y,W,H) = \; & j \quad \Big[2y_- \left(\arctan\tfrac{x_-}{y_-} - \arctan\tfrac{x_+}{y_-}\right) + \\ & \quad\; 2y_+ \left(\arctan\tfrac{x_+}{y_+} - \arctan\tfrac{x_-}{y_+}\right) + \\ & \quad\; x_- \ln\left(\tfrac{x_-^2+y_-^2}{x_-^2+y_+^2}\right) + x_+ \ln\left(\tfrac{x_+^2+y_+^2}{x_+^2+y_-^2}\right)\Big] \\ B_y(x,y,W,H) = \; & \quad\; -B_x(-y,x,H,W). \end{aligned} \tag{2.17}$$

The abbreviations used are $x_\pm = x \pm W/2$ and $y_\pm = y \pm H/2$. For locations above the wire center ($x = 0$), the field is oriented perpendicular to the current flow and parallel to the surface. The field strength is maximal on the wire surface ($h = y - H/2 = 0$):

$$B_{\max}(W,H) = j\left[4H \arctan\left(\frac{W}{2H}\right) + W \ln\left(1 + \frac{4H^2}{W^2}\right)\right] \tag{2.18}$$

If $H \ll h$ and $x = 0$, Eq. 2.17 reduces to the expression for an infinitesimally flat broad wire ($j = I/W$)

$$B_x(W,h) = 4j \arctan\left(\frac{W}{2h}\right); B_y = 0. \tag{2.19}$$

If in addition $W \ll h$, this reduces to $B(h) = 2I/h$, and the original field of a infinitesimally thin wire is recovered. The field on the surface of a flat ($H = 0$) but broad wire is $B_{\max}(W) = 2\pi j$. Fig. 2.24 illustrates the field scaling near a rectangular wire and compares it to the flat wire approximation which accurately describes the fields near wires with aspect ratios $W/H > 1$.

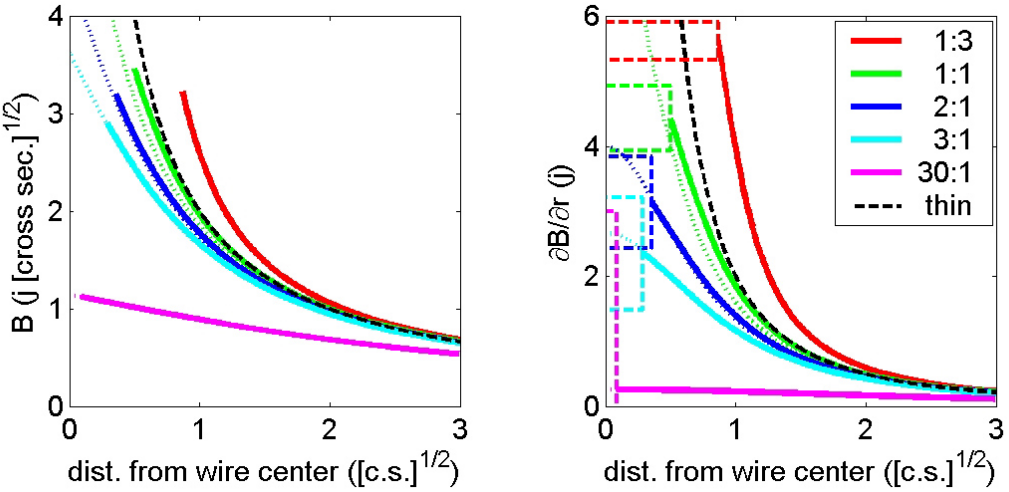

Figure 2.24: (*left*) Field strength as a function of height over the wire center for wires with different width to height aspect ratios. The solid lines represent the values calculated according to Eq. 2.17 and end at the wire surface. The dotted lines represent the flat wire approximation (Eq. 2.19). All wires are normalized to equal cross sections, thus the fields are equally normalized to current and current density. For comparison, the field of a infinitesimally thin wire carrying the same current is given (black dashed line). (*right*) Corresponding field gradients. In this plot the wire cross sections are shown to scale (dashed lines).

The field gradient of a broad and thick wire and thus the potential gradient at the trap minimum in a side guide configuration as a function of height over the wire surface ($x = 0$) is given by:

$$\frac{\partial B}{\partial r}(h, W, H) = 4j \left[\arctan\left(\frac{W}{2h}\right) - \arctan\left(\frac{W}{2h + 2H}\right) \right] \tag{2.20}$$

which reduces to

$$\frac{\partial B}{\partial r}(h, W) = 8j \left(\frac{W}{W^2 + 4h^2}\right) \tag{2.21}$$

in the limit of $H \to 0$ (Fig. 2.24). These expressions are maximal for $h \to 0$, i.e. on the wire surface:

$$\left.\frac{\partial B}{\partial r}\right|_{\max} = 8j \arctan\left(\frac{W}{H}\right) \xrightarrow{H \to 0} \frac{8j}{W} \tag{2.22}$$

In a realistic situation, however, it is impossible to form traps with these gradients since the barrier to the wire will be too small due to attractive surface interactions (Sect. 4.3) if h is smaller than some h_0. The magnitude of h_0 and the resulting limits for trap gradients and frequencies are discussed in Sect. 4.2.
It some cases it is desirable to form traps at off-center locations ($x \neq 0$). This can be realized by rotating the bias field so that a vertical field component B_v is

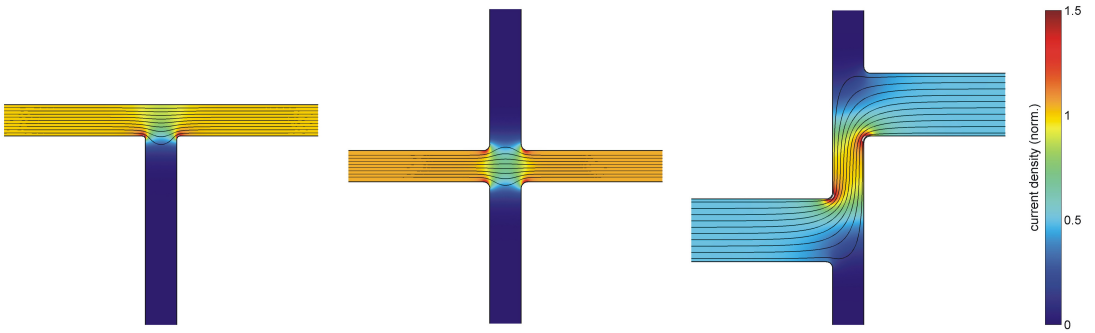

Figure 2.25: Numerical calculations of (planar) current densities in different geometries. The current density magnitudes (false colors) are normalized to the value at each of the central wires. The directions are indicated as stream lines. (*left*) The current flowing through a straight wire 'spreads out' at a wire junction. (*center*) The behavior at a wire crossing is similar. (*right*) The current flow through a Z-shaped wire can deviate significantly from a simple 'stick model' approximation in which thin wires are assumed to replace the real wires at their respective centers. The geometry shown is the one used underneath the atom chip for BEC production (Sect. 3.1.2).

introduced. In chapter 3 (Sect. 3.2.6) the technique of scanning B_v is applied to probe the surface of a wire at different transverse positions.
For three-dimensional wire geometries, effects arising from inhomogeneous current densities $\mathbf{j}$ have to be taken into account. Fig. 2.25 shows examples of numerical calculations of $\mathbf{j}$ near wire bends and junctions. In many cases, a modified stick model accounting for the $\mathbf{j}$ profile by introducing effective lengths and angles is sufficient to approximate the fields of such structures. For a Z-trap, for instance, the effective length that needs to be assumed for the central wire (Fig. 2.25) is shorter than the real center to center length.

2.5 Electric fields

The interaction between a neutral atom and an electric field is determined by the electric polarizability α of the atom. In general, α is a tensor. For the simple atoms used in our experiment, i.e. atoms with only one unpaired electron in an s-state, the electric polarizability is a scalar and the interaction can be written as

$$U_{\mathrm{el}}(r) = -\mathbf{d}.\mathbf{E} = -\frac{1}{2}\alpha E^2(r). \tag{2.23}$$

Eq. 2.23 shows that atoms in the ground state are drawn towards higher electric fields since the interaction of the induced dipole $\mathbf{d}$ with the field is always attractive. As a consequence, the *minimum* of a purely electrostatic trapping potential will be located at a (local) *maximum* of E. According to the Earnshaw theorem, however, such a maximum cannot exist in free space. Any trap utilizing

electric fields therefore has to compensate for the attraction of the trapped atoms towards the charged objects creating the electric fields.
Stabilizing such a trap is possible either by adding (static) repulsive potentials, e.g. by introducing inhomogeneous magnetic fields or light fields, or by dynamically changing the electric fields (the 'Kapitza' wire, [85, 177]). The repulsion of a centrifugal barrier felt by atoms orbiting around a charged wire cannot be used since no stable orbits exist is such a potential. This motion of atoms near an attractive $1/r^2$ singularity has been studied both theoretically [47] and experimentally [48].
Instead, it has been suggested to form a barrier by mounting charged structures onto magnetic or optical atom mirrors [172, 96]. Alternatively, blue detuned light propagating through an optical fiber could be used to provide an exponentially decaying repulsive potential in combination with an attractive electric potential invoked by charging the fiber electrostaticly. We have discussed these and other scenarios of combining the electric interaction with an appropriate repulsive potential to confine atoms in [62].
The integration of electric fields as means of atom manipulation provides an additional degree of freedom and enhances the degree of control over matter waves on atom chips. In addition to the higher flexibility in the design of confining potentials (Sects. 2.5.2, 2.5.3), the fact that the magnetic quantum number m_F of the atom affects only the interaction with magnetic fields, and not the electrostatic interaction allows state conditional operation in combined magneto-electric potentials (Sect. 2.5.4). Another application of electric fields is to modify a mainly magnetic potential. This can, for example, be used to imprint a controlled phase difference between the two arms of an otherwise symmetric guided matter wave interferometer (Sect. 4.4) or to locally slightly lower the trapping potential in an elongated trap in order to form a 'dimple' that promotes the transition to Bose-Einstein condensation (Sect. 5.1).
The first experimental demonstration of a trapping potential based on electrostatic fields was an *opto*-electric trap where the confinement in the direction of free propagation in an two-dimensionally confining optical dipole trap was provided by the electrostatic field of a charged ring electrode [125]. This experiment was performed on a macroscopic scale, but the concept could in principle be transferred to microtraps on atom chips. This would have all the above advantages, except for the state dependent operations since both the electrostatic and the light interaction do not depend on m_F.
In our experiments with thermal ^{7}Li atoms, we have used electrostatic fields to form a novel type of combined magneto-electric trap where the confinement in two dimensions is magnetic while the movement in the third dimension is controlled by electric fields [119]. These experiments that were performed on atom chips are described in this section. First, the demonstration of the traps is presented (Sect. 2.5.1), followed by examples of first applications (Sects. 2.5.2, 2.5.3). The chapter ends with an account on first hints of observation of state selective operation and

an outline of possible trapping geometries for a clear future demonstration of principle (Sect. 2.5.4).

2.5.1 Modulated wire guides: combined magneto-electric traps

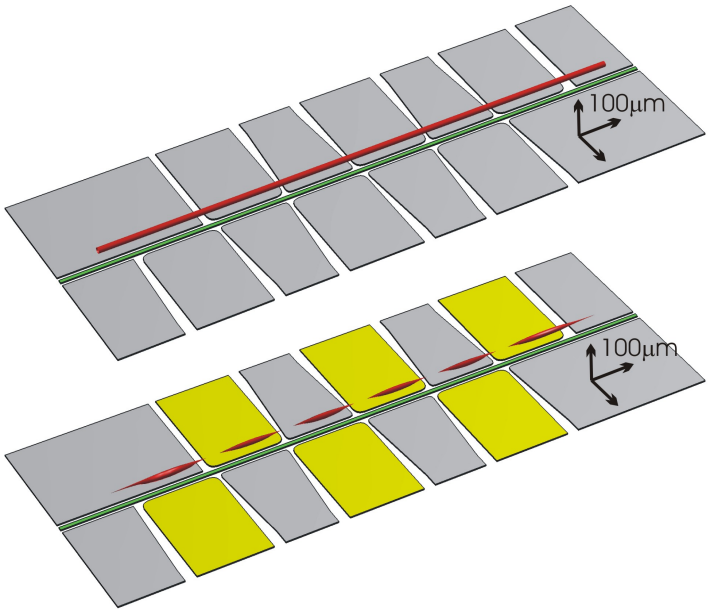

Figure 2.26: Chip design: A magnetic side guide is modulated by applying voltages to the set of six electrodes (dark gray in center plot). Equipotential surfaces ($E_{\mathrm{pot}} = 475\mu$K) are shown for ^{7}Li atoms in the $|F = 2, m_F = 2\rangle$ ground state for the side guide (top) and a string of six combined magneto-electric traps (bottom). The parameters chosen for these numerical calculations were $I_{\mathrm{wire,y}} = 1$A, $B_{\mathrm{bias,x}} = 40$G, and $V_{\mathrm{elec}} = +475$V.

A combination of the electric and magnetic interactions allows to realize stable trapping configurations on atom chips. In our experiments, we produce electric fields by charging a set of electrodes distributed along a current carrying wire (Fig. 2.26) forming a side guide (Sect. 2.4.2). Charging the electrodes results in an inhomogeneous electric field that is modulated in strength along the guide. Such a modulation can lead to a full three-dimensional confinement given by the potential

$$U_{\mathrm{mag+el}} = \mu_B g_F m_F B - \frac{\alpha}{2} E^2. \tag{2.24}$$

Fig. 2.26 shows our design and typical equipotential surfaces of the magnetic side guide and a string of combined traps that is formed when a moderate voltage is applied to the six electrodes along the guiding wire. We have performed extensive

numerical calculations regarding the parameter ranges needed to form combined magneto-electric traps with this geometry. The details of the calculations and their results are given in [112]. We found that a few hundred volts are needed in order to form potential wells that are deep enough to trap thermal ^{7}Li atoms of $T \sim 100\mu$K at a height of 50μm above the chip surface. If the voltage is too low, the modulation of the guiding potential becomes weaker, if it is too high, the attractive electric interaction lowers the magnetic barrier to the chip, and the atoms can propagate onto the surface. However, the voltage range where traps are formed is large, and trap depths of up to 500μK are possible. In this case, the barrier to the attractive potential near the electrodes is large enough to inhibit tunnelling to the surface completely.

The two atom chips we have used in our experiments are based on silicon and sapphire substrates with a thickness of 600μm covered with a $\sim 4.5\mu$m tall gold layer. Both types of substrates tolerated voltage differences of a few hundred volts over spatial separations of 10μm. The Si substrate, however, exhibited a slow degradation at $V_{\mathrm{elec}} > 300$V which was not encountered on the sapphire substrate at all tested voltages, i.e. up to 400V. The distance of the charged structures to grounded parts of the chip was 10–50μm.

In our experiment, we accumulate typically 10^8 ^{7}Li atoms in a reflection MOT [30]. With the intermediate support of a U-shaped silver wire mounted directly underneath the chip, atoms in the weak field seeking states ($|F, m_F\rangle = |2, 2\rangle;|2, 1\rangle;|1, -1\rangle$) are loaded into a Z-shaped wire trap on the chip. The loading procedure is described in [61, 37].

Fluorescence images are taken by exposing the atoms to a light pulse of 100μs duration from two counter-propagating light beams that enter the vacuum chamber parallel to the chip surface. This configuration suppresses all artifacts on the images stemming from features on the chip surface. Even if electric fields are present at the time of the imaging light pulse, the resonance shift due to the differential Stark effect is much smaller than the line width of the atomic transition (at a typical field of 10^6V/m, $\Delta\nu_{\mathrm{Stark}} = 450\mathrm{kHz} \ll \Gamma/2\pi = 5.8\mathrm{MHz}$ [199]). Therefore, the modulation of the fluorescence signal can only be attributed to an actual modulation in the atomic density.

After loading, the atoms hover 50–100μm above the chip surface in an elongated trap of approximately 1mm in length. In the next step, the trapping potential is opened on one side by switching the current so that it now runs along an L-shaped path. If no voltage is applied to the electrodes along the central piece of the Z-shaped wire, all atoms are lost within approximately 50ms after they are released to the guide (Fig. 2.27 left). If, however, at the time of the opening of the guide the voltage on the electrodes is switched on non-adiabatically (within 5μs)[6] to 250–350V, a sizeable fraction of the cloud, i.e. those (sufficiently cold)

[6] An adiabatic switching would not allow to trap the atoms because a conservative potential cannot introduce the necessary energy dissipation.

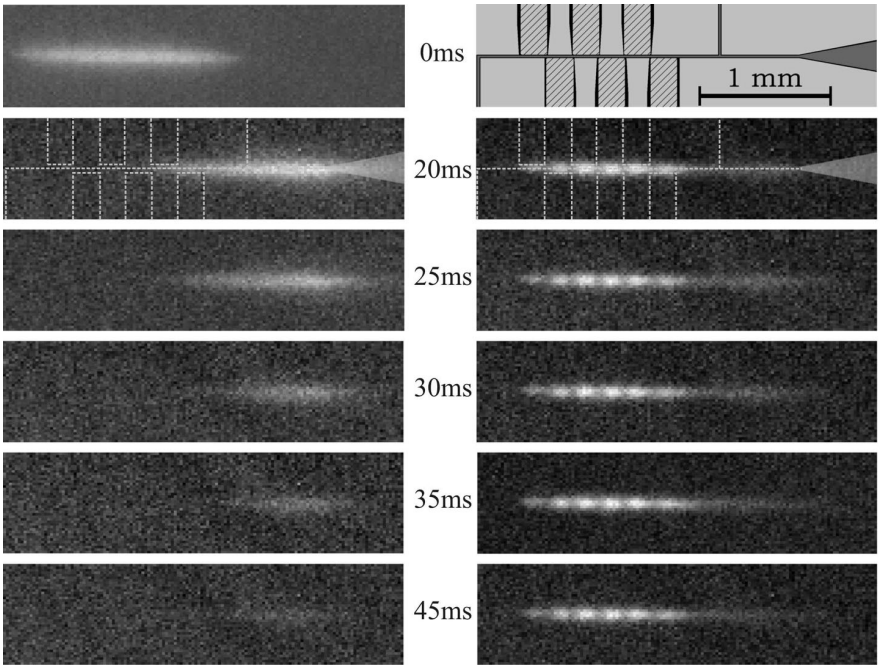

Figure 2.27: Time series of fluorescence signals in experiments demonstrating the trapping of thermal ^{7}Li atoms in combined magneto-electric traps: (*left*) At $t = 0$, a cloud of atoms is released from a magnetic Z-trap into an open L-shaped guide where the guiding wire is broadened at the open end on the right hand side, guiding the atoms towards the chip surface where they are lost. (*right*) If a voltage is applied to the electrodes along the guide, atoms remain in six individual trap sites. The smaller populations in the leftmost traps can be attributed to the magnetic field gradient stemming from the current flow in the lead of the L-shaped wire. (*top right*) The actual chip design used in these experiments with the different current carrying and charged structures. The parameters used in this case were $I_{\mathrm{wire}} = 1.6\mathrm{A}$, $B_\perp = 44\mathrm{G}$, and $V_{\mathrm{elec}} = +300\mathrm{V}$.

atoms that are located above the electrodes where the potential minima appear, remains trapped (Fig. 2.27 right). A comparison of the two experiments described above clearly shows the trapping effect of the electric field introduced by the high voltage. All six electrodes could be switched separately so that an arbitrary subset of traps could be operated (Fig. 2.28). The lifetime of the trapped clouds was consistent with lifetimes measured in purely magnetic traps. A detailed analysis can be found in [28]. In our experiments with ^{7}Li atoms, the lifetimes were limited by background gas collisions to 1s; with better vacuum, lifetimes > 30s have been obtained in our new ^{87}Rb apparatus (chapter 3). Losses induced by Majorana transitions do not play a role here, due to the relatively high temperatures of the atoms. For colder atoms, they can be avoided by adding a small longitudinal magnetic bias field component.

The experimental results agree quantitatively with the numerical predictions presented above regarding size and position of the traps, while the exact voltages

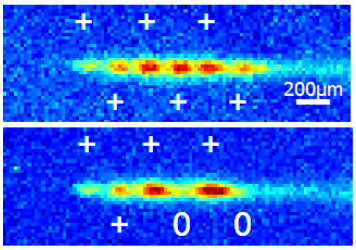

Figure 2.28: Within a string of six electrodes, an arbitrary subset of traps can be operated (almost) independently (the longitudinal confinement in one trap is slightly higher if the neighboring trap is operated than if it is not). (*top*) False color fluorescence image of all six traps in operation (indicated by '+'-signs). (*bottom*) A subset of four traps ('0's indicate grounded electrodes).

leading to a maximal number of trapped atoms differ by up to 50%. We attribute this deviation to the fact that the calculations were idealized, i.e. the dielectric properties of the involved materials were neglected and only the central region of the chip was taken into account. The anticipated behavior of weaker modulation in the atom density for lower electric fields was observed as well as the loss of atoms to the chip surface at voltages that were too high (Sect. 2.5.4).

2.5.2 Controlled transport

In order to demonstrate some of the new capabilities of the atom chip introduced by the integration of electric fields, we carried out further experiments. In one experiment we showed the controlled transfer of an atom cloud along a magnetic guide by means of electric fields (see [166] for a purely magnetic transfer).
The geometry of the chip structures necessary for this 'motor' experiment and the timing sequence is illustrated in Fig. 2.29. A single trap was initially loaded by repeating the above described procedure, but only switching on the voltage on one of the electrodes. After a short trapping time, a voltage of reversed polarity was ramped up on a neighboring electrode on the opposite side of the guiding wire while the voltage on the first electrode was ramped down to zero. At the intermediate stage where the voltages on both electrodes are on, the electric field strength along the guide is maximal in the middle between the two electrode centers. The different polarity is essential for a smooth, barrier-free transfer of the cloud. To maintain a nearly constant trap depth throughout the transfer, the voltage ramps were run in two steps: During the first 7.5ms the voltage on the first electrode was ramped from +280V to +200V, while the voltage on the second electrode was ramped from 0 to −200V. Within the following 7.5ms, the first voltage was ramped down to 0, while the second voltage was ramped up completely to −280V. This process was subsequently replicated between the second electrode and a third electrode, again located on the opposite side of the guiding wire. After the complete sequence of 30ms duration, the whole atomic cloud had been transported over a distance of 400μm. Adiabaticity conditions limit the speed of the transport. When colder atoms, ideally BEC are used, the traps can be made much smaller, and trap frequencies of up to 1MHz are possible. This will allow an adiabatic transport on a time scale (μs) that is much faster than predicted coherence times [90] (Sect. 4.1). The measured loss of atoms during

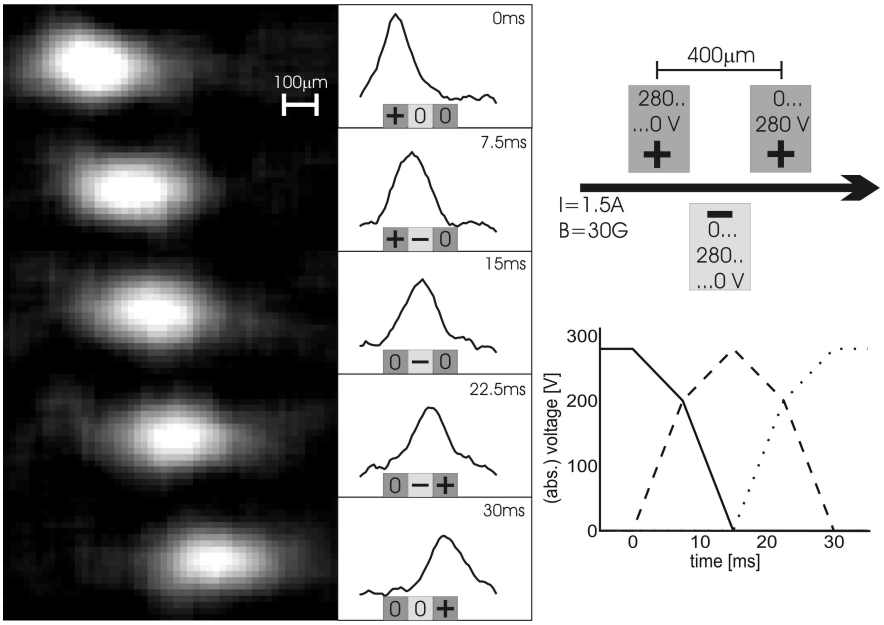

Figure 2.29: (*left*) An atom cloud confined in a single combined magneto-electric trap ($I_{\mathrm{wire}} = 1.5\mathrm{A}$, $B_{\perp} = 30\mathrm{G}$, and $V_{\mathrm{elec}} = 280\mathrm{V}$) is smoothly transported along the magnetic side guide. (*center*) Longitudinal profile of the atom distribution as the cloud is transferred over a distance of 400μm during 30ms. The voltage on the different electrodes at the different phases of the transfer are depicted schematically. (*right*) The timing of the voltage ramps was chosen to allow a smooth transfer from one trapping site to another while maintaining a nearly constant trap depth of 50–60μK.

the transfer is equal to that observed in a static trap which proves that losses induced by the transfer process are negligible with respect to the trap lifetime.
As wire cross sections, resistances, and atom-surface distances become smaller in more recent (chapters 3 and 4) and future experiments (chapter 5), the voltage drop along current carrying wires becomes important. While too high voltages are able to reduce or even remove the repulsive magnetic barrier to the surface, such effects can also be used constructively. In [62] we have outlined a scheme to use the remaining free parameter when driving a current through a wire, namely the overall electric potential, to form another type of 'motor' based on electrostatic fields. Here, the transport relies on a gradual tuning of the wire voltages so that an atom cloud always follows the position of maximal electric field along the magnetic guide.

2.5.3 An electric beamsplitter

In a second experiment we observed a dynamic splitting and recombination of an atom cloud into two separate clouds. Again, the experiment was initiated by loading a single trap. While the voltage on the first electrode is ramped down

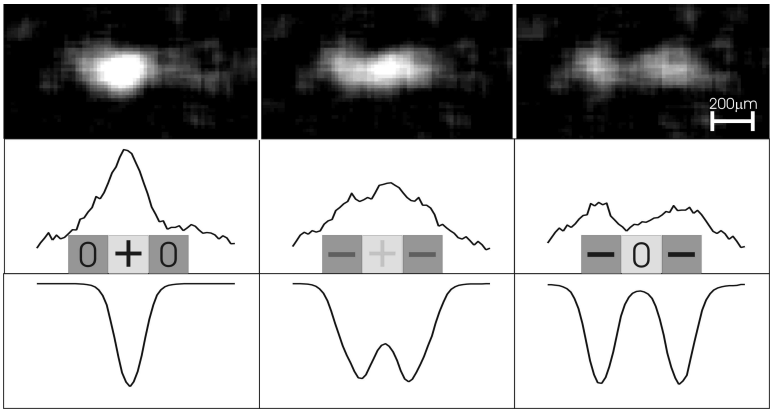

Figure 2.30: Dynamic splitting of an atom cloud. A single trap is gradually (within 15ms) turned into a double well potential by ramping the voltage on one electrode down while two neighboring electrodes are slowly charged. (*top*) Fluorescence images of the atoms during different stages of the experiment. The inserts schematically show the polarities and voltages (darker shading corresponds to higher voltage) during the different phases of the experiment. (*center*) The density profile clearly shows the gradual splitting of a single cloud into two. (*bottom*) The corresponding potentials along the axis of free motion in the magnetic guide.

to 0, voltages of equal magnitude but different polarity (−200V) are gradually (within 15ms) ramped up on the two neighboring electrodes on the opposite side of the guiding wire in a fashion similar to the one used for the 'motor'. The results of this experiment and the calculated potentials during the different stages of the experiment are shown in Fig. 2.30. For the recombination of the two clouds, the process is reversed. In these experiments, again no additional loss with respect to the lifetimes in the static traps could be detected.

2.5.4 State dependent operation

Electric fields can be used for state-selective operations. This is based on the fact that the magnetic part of the combined magneto-electric potential (Eq. 2.24) depends on the magnetic quantum number m_F while the electric part does not. In [184] it has been shown that a two-qubit phase gate based on controlled collisions can be realized by storing two atoms in the two minima of a double well potential in which the separating barrier can be conditionally removed for one qubit state but not for the other. If the qubit is encoded in atomic hyperfine states with different m_F, a combination of electric and magnetic potentials will allow such a configuration: The central barrier in a magnetic double well potential is of different height for the different m_F, and can therefore be removed state-selectively by an electric field since the electric potential does not depend on m_F (Eq. 2.24). In the following, the first indications of state dependent operation in our experiments are discussed, and future demonstration experiments in double well

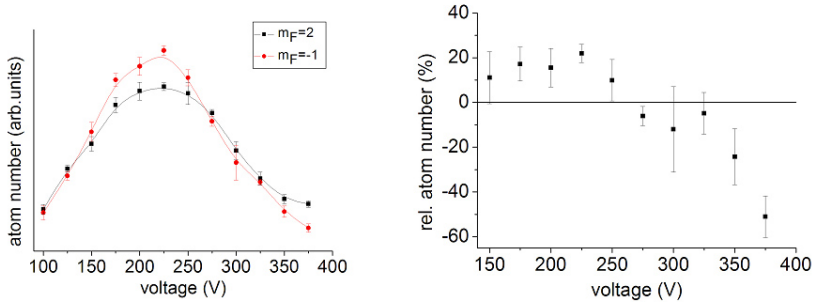

Figure 2.31: The effect of the electrode voltages in combined electro- magnetic traps differs for atoms in states with different m_F. (*left*) Number of trapped atoms versus applied electrode voltage for different m_F. The trapping potential used is that described in Sect. 2.5.1 with $I_{\text{wire}} = 1\text{A}$ and $B_\perp = 25\text{G}$. The lines are spline interpolations shown to guide the eye. (*right*) Relative deviations from equal atom numbers for both voltages as a function of applied voltage. The magnetically less bound state ($m_F = -1$) appears to be slightly favored at smaller voltages (positive deviation), while the $m_F = 2$ state dominates at larger voltages (negative deviation).

potentials are outlined.

State selective trapping

In our ^{7}Li setup hyperfine states with different magnetic quantum numbers m_F were prepared by optionally switching the laser on the repumping transition ($F = 1 \rightarrow 2$) off 100μs before the MOT-phase of the experimental cycle is ended by extinguishing also the light on the cooling transition ($F = 2 \rightarrow 3$). As a cooling cycle under the assumption of light intensities much larger than saturation intensity lasts only ~ 50ns, a non-resonant transition to the $F' = 2$ state followed by a decay into the dark $F = 1$ state is likely to occur during these 100μs. Since the only trapped state of the $F = 1$ manifold is the $m_F = -1$ magnetic substate, this procedure ensures a pure $m_F = -1$ sample in the magnetic traps. On the other hand, if the repumping light is switched simultaneously with the cooling light, a mixed sample of atoms in $|F = 2, m_F = 2\rangle$, $|F = 2, m_F = 1\rangle$, and $|F = 1, m_F = -1\rangle$ states will be transferred to the magnetic trapping potentials. In this case, lossy binary collisions probably remove the atoms quickly from the trap, unless they are in the $|F = 2, m_F = 2\rangle$ state [40, 62]. Even though we have not verified a pure $|F = 2, m_F = 2\rangle$ population experimentally, it appears to be safe to assume that at least a significant fraction of atoms should be in this magnetically more strongly confined state.

In order to investigate the state dependent behavior in our combined magneto-electric traps, we have performed electrode voltage dependent atom number measurements for both above described state preparations. The results are depicted in Fig. 2.31. At large voltages, clearly more atoms in the $m_F = 2$ state are

trapped than in the same experiments with an $m_F = -1$ sample. This can be explained by the fact that atoms are lost at high voltages due to a compensation of the magnetic barrier to the chip surface by the electric potential. Since the magnetic barrier for the $m_F = 2$ state is twice as high as for the $m_F = -1$ state, this effect becomes important already at lower voltages for the magnetically less bound state. The slight preference for the $m_F = -1$ state at low voltages, on the other hand, can possibly be attributed to the higher compression and hence larger temperature of the magnetically strongly confined $m_F = 2$ state.
The details and exact behavior of different m_F states in combined magneto-electric potentials remain to be investigated in future experiments. We are currently preparing such experiments with much colder ^{87}Rb atoms which will be optically pumped into the desired states.

Double well potentials and controlled collisions

A more compelling demonstration of state conditional operation of a combined magneto-electric potential would not be based on state selective losses. Rather, a potential design should aim at merging the two wells of a double-well potential for one magnetic state but not for the other along the lines of the quantum gate proposal suggested in [184]. Here, two example configurations are sketched that should be fairly simple to implement experimentally on an atom chip.
In the first scheme, the magnetic double well potential is formed by overcompensating the bias field $B_\perp$ in a Z-trap (Sect. 2.4.9). The height of the barrier between the two wells is given by the amount of overcompensation scaled with a factor $g_F m_F$. Electrodes on the side of the wire can now be used to remove this barrier state-selectively. Numerical calculations show that a careful choice of voltages on the electrodes on the chip used in the above described experiments leads to a situation of the desired kind. A double well potential with a barrier sufficient to maintain a $\sim 50\mu$K barrier between the two wells for $m_F = 2$ state atoms turns into a single well potential for atoms in the $m_F = -1$ state. In our experiments, the atoms were not cold enough to actually observe this effect. This limitation does not play a role in our ^{87}Rb apparatus, and a simulation of a controlled collisions experiments should be possible by observing merging clouds in one case ($m_F = -1$) and clouds that remain split ($m_F = 2$) in the other. Care has to be taken regarding losses due to Majorana spin flips if the atoms are too cold.
The second scheme is based on a double well potential above two wires carrying co-propagating currents (Sect. 2.4.3). A third wire in the center between the two current-carrying wires can be charged and thus conditionally remove the barrier between the two guiding minima whose strength again depends on m_F. This scheme should easily be extendable to three-dimensionally confining geometries. An advantage over the first scheme is that zeroes in the magnetic trapping potentials are avoidable.

3 Surface disorder potentials

Various methods of manipulating cold atoms near structured surfaces in well controlled potentials have been presented in chapter 2. The basic concepts and parameter scaling was experimentally verified with thermal ^{7}Li atoms. The feasibility of a variety of different micro-atomoptical techniques and tools could already be demonstrated, but the limitations of experiments with thermal atoms at comparably large distances from the surfaces are apparent: If the advantages of the high tailoring resolution of steep potentials created by microstructures are to be exploited to an extent that allows accurate control at the quantum level, approaching the surface to single micron distances is inevitable. This was already discussed in chapter 2 (introduction and Sect. 2.2) where the basic scaling laws were given. The main consequence is that the spatial resolution of the potentials is not limited by the fabrication but rather by the distance between atoms and surface.

A full control over the atoms also implies that the quantum state inside the trap is known and addressable. This is virtually impossible for relatively hot thermal atoms as hundreds or even thousands of trap levels are populated statistically (according to the Boltzmann distribution). Bose-Einstein condensates (BEC), in contrast, occupy a single trap state, namely the ground state of the trap. In some cases, it is also interesting to work with thermal atoms at temperatures just above the critical condensation temperature T_C, so that already several states are involved but complicated many-body effects can be neglected.

The experiments presented in this chapter were performed in order to explore the possibilities of trapping and manipulating Bose-condensed and ultracold thermal atoms in micropotentials close to the surface. As the cooling of atoms to BEC is known to be straightforward for rubidium atoms in conventional setups, we chose to use the ^{87}Rb isotope of this element in our experiments. Even though the condensation of ^{7}Li atoms is possible [24, 175], the experimental requirements are more severe than for ^{87}Rb, especially because of the lower s-wave scattering length and its negative sign. The consequence of the attractive interactions is a maximal possible atom number in a BEC. To date, ^{87}Rb is the only element that has been condensed in a microtrap[1]. Therefore it seemed worthwhile to construct a new apparatus. As part of this thesis work, this apparatus was designed, built and operated. The various parts of the basic setup have been presented

[1] In one atom chip experiment, sodium BECs created elsewhere could be loaded to a microtrap [77].

comprehensively in the diploma theses [15, 67, 86, 25]. A short summary of the main features is given in appendix B.
This chapter is divided into two sections: The first section (Sect. 3.1) gives an account of the experimental procedure of loading atoms close to the chip surface and cooling them to BEC or to temperatures just above T_C. Emphasis lies on the special features of our approach, i.e. those elements that are different from standard BEC experiments.
The second part of the chapter deals with disorder potentials very close to the surface of (imperfect) microwires. The effects of such potentials have been one of the major concerns over the past two years in the growing field of atom chip research. Several groups have reported irregular potentials to start to have a dominant effect at surface distances as high as $\sim 50\mu$m [63, 123, 107, 60]. These effects were already believed to severely limit the possible applications of the whole atom chip concept. We could now show that our different chip fabrication technique (Sect. 2.2) strongly reduces unintended potentials [117]. In Sect. 3.2, the results of our experiments with thermal atoms and BECs close and very close to surfaces of different wires are given and compared to the data measured in other groups. In the course, it turns out that BECs are an extremely sensitive tool to measure local magnetic fields to a precision that is difficult to reach by other methods (Sect. 3.2.6).

3.1 Atom cooling and BEC production near surfaces

In this section, the steps of the experimental procedure we use to prepare ultracold atomic ensembles near surfaces are introduced. A more detailed documentation will be given in [98]. The setup consists of a laser system supplying light beams of the various frequencies needed throughout the experiment [67, 86], a vacuum chamber [86] that contains the atom chip assembly [15], numerous coils for external magnetic field adjustment, a detection system, and an experimental control unit [25]. Since these components and their properties have already been covered in the cited diploma theses, it suffices to give a short wrap-up in the appendix (appendix B). Certain properties of the setup that are directly important for the actual experiments presented in this chapter are discussed in the main text. An example is the special imaging technique to detect atoms close to the (reflecting) surface ($h < 100\mu$m) [6] which we have used to calibrate the height above the surface h (Sect. 3.2.3).

3.1.1 Integrated U-MOT

A magneto-optical trap (MOT), whose operation principle is part of standard textbooks by now [140], forms the starting point of every experimental cycle. Experiments near surfaces suffer from the difficulty that material objects partly

obstruct the optical access to the experimental region. This means that either the cold atom cloud has to be formed in situ or at a different location and then be transported to its final position.
We have significantly simplified this process by customizing an intermediate size copper wire structure that is mounted directly underneath the atom chip [197]. In the following, our scheme is outlined and the experimental implementation as well as the obtained parameters are discussed.

Wire geometries and quadrupole fields

A MOT requires laser light forces from all directions. Consequently, placing a MOT close to a surface implies that either the surface and the laser beam diameters have to be small enough relative to the height of the MOT above the surface or that the surface is transparent or reflecting. The problem of a material object (partially) obstructing the access of the six beams used in a conventional MOT has also been circumvented by producing the MOT [151] or even a condensate [122] elsewhere and transfer it to the chip by means of dynamic magnetic fields [151] or optical tweezers [122]. The alternative is to directly load a *mirror MOT* [124, 159, 166, 61] only millimeters away from a reflecting surface that acts as a mirror. In this configuration, at least one of the MOT beams is reflected off the mirror. In the simple version used in many atom chip experiments [166, 61, 107], two of the regular six MOT beams are replaced by reflections of two beams impinging upon the mirror (the chip) at an angle of 45 degrees. To ensure the correct quadrupole field orientation with respect to the helicities of the light beam pairs, the quadrupole field axis has to coincide with one of the 45 degree light beams. Up to now, this had to be considered a drawback since the coils usually employed to provide the field are bulky, dissipate a large amount of power, and deteriorate the optical access to the MOT itself and to the region where the experiments are carried out. As experimental setups are likely to grow more complex in the future, including quadrupole coils in the setup will present a major obstacle. Apparatus involving cryostats aiming at a significant reduction of thermal current noise in conducting surfaces [90] are just one example.
A way of approximating a quadrupole field is to use a current carrying wire that is bent in a U-shape together with a homogenous bias field parallel to the wire plane and perpendicular to the central bar of the U (Sect. 2.4.8). Fig. 3.1b shows the field configuration obtained in comparison to a field created by external coils in the common anti-Helmholtz configuration (Fig. 3.1a). But a MOT based on a simple U-shaped wire cannot be used for an efficient collection of a large number of atoms (for example from the background Rb-vapor). This is caused by the fact that the U-wire field is only a true quadrupole field near the field center (point of vanishing field). Further out there is a a non-vanishing angle between the quadrupole axes and the field lines (Fig. 3.1d). This angle increases at larger distances from the field zero, i.e. the MOT center, and eventually the direction of

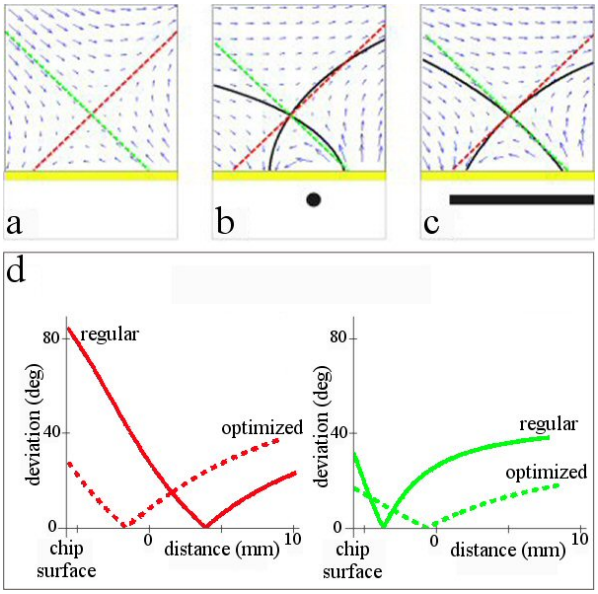

Figure 3.1: Vector plots of different field configurations. The black (green and red) lines indicate the axes of the approximated (ideal) quadrupole fields. (a) ideal quadrupole field, (b) regular U-wire quadrupole field with untilted bias field, (c) optimized U-wire quadrupole field. The wire cross sections are shown at the bottom of (b) and (c). (d) Angular deviations from the ideal quadrupole axes are plotted as a function of the distance from the MOT center along the two 45 degree light beam paths (green and red lines in (b) and (c)). The parameters chosen in these examples were $I = 55\text{A}$, $B_{\parallel} = 14.5\text{G}$ (12.8G) and $B_{\perp} = 0\text{G}$ (3.0G).

the field vectors is even reversed. As the operation principle of a MOT relies on the correct orientation of the fields with respect to the polarization of the laser light in each beam, the effective capture region of the trap and thus the loading rate and the maximum number of atoms in the MOT are limited. Consequently, the U-MOT has to be loaded from a regular quadrupole coil MOT in order to collect a large number of atoms. This simple type of U-MOT is typically used as an intermediate experimental stage because it can be aligned to surface patterns by construction and it allows a simple compression of the atomic cloud as it is lowered towards the surface by increasing the homogenous bias field.

However, by altering the geometry of the U-shaped wire, a much better approximation of a quadrupole field can be obtained: The bent field lines in the case of a simple U-wire can be attributed to the fact that a thin wire produces a field whose field lines are circles. Consequently, the simplest way to overcome this is to fan out the current flow through the central part of the U by replacing the thin wire by a broadened plate. Inclining the bias field with respect to the plane formed by the outer leads of the U improves the field configuration further. If the plate is inclined and if the shape of the current flow through the plate is adjusted properly, the resulting field will approximate an ideal quadrupole field even more closely.

We chose to set the last two possibilities aside in our experiment, mainly because they lead to only marginal improvement compared to the wide U, and they are more difficult to implement. Fig. 3.1c shows the field vectors of the quadrupole field obtained with a modified planar U-shaped wire. The various parameters (geometry, wire current, and bias field) were optimized numerically to achieve typical field gradients (10–20G/cm) of a MOT at a height of 6–8mm above the the wire center (4–6mm above the chip surface) while maintaining small angular

deviations of the field from an ideal quadrupole field throughout the maximal capture region given by a typical light beam diameter of 2cm. A comparison of the field configurations of the U-wire quadrupole field with the ideal field shows no significant differences in the planes not shown in Fig. 3.1. Only the field gradients deviate from those obtained in a conventional quadrupole configuration: In the direction parallel to the central bar of the U-shaped wires, the gradients are weak while those in the transverse directions are of approximately equal magnitude. The gradient ratios for the regular (optimized) U-wire are $\sim 1:4:5$ ($\sim 1:3:4$), for the ideal quadrupole field $1:1:2$. Gradient ratios, however, are not critical for a MOT operation. In fact, this can even be an advantage because the aspect ratio of the MOT cloud is better matched to the magnetic microtraps. With our configuration, it turns out that moderate wire currents of 50–70A at small (calculated) power consumptions ($<$ 1W) and small bias fields of 7–13G are sufficient to create a near to ideal quadrupole field at a variable height above the chip surface. To produce homogenous fields of this strength, currents of a few amps in Helmholtz-coils outside the vacuum chamber are sufficient. We are currently developing a second generation structure in which these coils are completely replaced by an integrated current sheet. The residual angles of the field vectors are small enough to lie within the tolerance of a MOT, as was tested by rotating the light polarizations in an external MOT experiment[2]. The MOT remained unimpaired for elliptical polarizations corresponding to deviations of the field line direction of up to 40 degrees from the ideal situation.

Implementation and experimental characterization

In our experimental implementation we use a U-wire structure that has been machined out of a single copper piece. This copper structure is incorporated in a MACOR ceramics block holding an atom chip. Between chip and central part of the U, a small space was left to allow the placement of another copper structure that contains several Z-shaped wires forming magnetic traps for BEC production (Fig. 3.2b, Sect. 3.1.2). In order to keep ohmic heat dissipation as low as possible while allowing currents of up to 100A, a wire cross section of at least 7mm^2 is maintained all over the U-wire structure. The 3mm $\times$ 3mm leads are thicker than the plate (thickness $\times$ width $\times$ length = 0.7mm $\times$ 10mm $\times$ 18mm) to ensure a homogenous current density in the plate (Fig. 3.2c). Isolated by a thin (100μm) Kapton foil, a 1mm thick additional structure for purely magnetic trapping is positioned on top of the plate (Sect. 3.1.2). The geometry of this structure resembles an H with two extra leads connected to the central bar. The U- and the H-shaped structures were designed in such a way that their surfaces lie in a common plane so that an atom chip can be mounted directly on top of both structures. The copper structures are connected to high current

[2]For this purpose we tested both a conventional six-beam MOT (student's lab course setup) and the other ^{87}Rb mirror MOT setup in our group [173, 109].

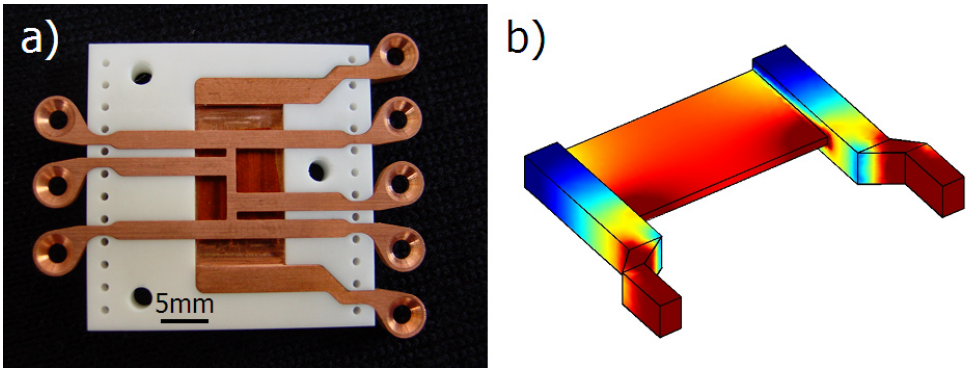

Figure 3.2: (a) Photograph of the wire structures fitted into a MACOR ceramics holder. (b) Results of a numerical calculation of the current density distribution in the U-wire. Dark red (blue) shades correspond to high (low) current densities. The thick connecting leads ensure a homogenous fanning out of the current through the central plate as it is needed to improve the quadrupole field for the MOT.

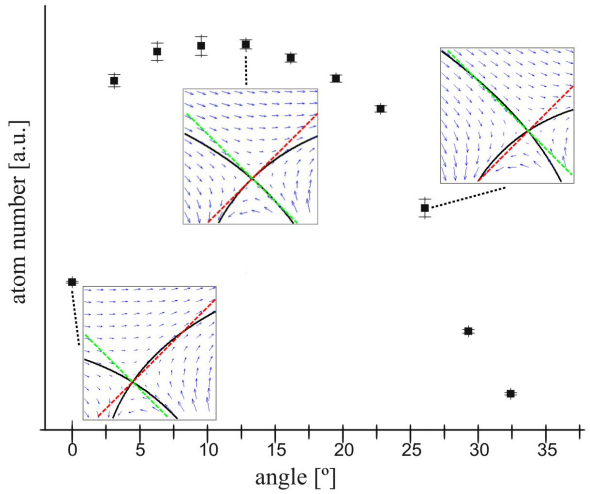

Figure 3.3: The number of atoms is plotted versus the tilting angle between the bias field and the plane of the broad U-shaped wire. For these measurements the U-current was 55A, the bias field strength 13G. *Inserts*: Corresponding vector field plots for three different angles (0 deg, 13 deg, 26 deg). The maximum number of atoms is trapped at a bias field angle of 13 degrees where the shape of the field is closest to an ideal quadrupole field. Note that this optimal trap position is not centered above the wire.

vacuum feedthroughs by simple screw contacts, the chip wires are attached to pin connectors by a bonding technique [15].

The complete assembly with the current connections, the wire structures for the MOT and magnetic traps, and the atom chip (Fig. B.2 in appendix B.2) is built into a ultra-high vacuum (UHV) chamber that was constructed to allow good optical access to the experimental region directly above the surface of the chip (see appendix B).

As a source for rubidium atoms we use three dispensers that are connected in parallel. A high pumping speed in combination with a pulsed operation mode of the dispensers facilitates sufficient loading rates of the MOT of typically 3×10^7 atoms/s while the rubidium background vapor is quickly reduced in the purely magnetic trapping phase of the experiment. A careful adjustment of the dispenser

currents during the MOT loading phase of the experiment can significantly decrease the cycle time; we have been able to reduce the repetition rate of the experiment from more than 70s to 40s solely by optimizing the dispenser currents [98].
Typically, we operate the MOT at a U-wire current of 60A and a bias field of 13G, i.e. at magnetic field gradients of 5G/cm (20G/cm) along the axis of weakest (strongest) confinement. In order to confirm the effect of the improved quadrupole field on the MOT, we have compared a MOT formed by a thin U-shaped wire with the broad wire U-MOT. The change in geometry yielded an improvement factor of 10 in atom number in the MOT in our experiment. Inclining the bias field further enhances this number by a factor of 2–3. Fig. 3.3 shows the measured atom number in the MOT as a function of the angle between the bias field and the plane of the modified U-shaped wire. The corresponding quadrupole fields for specific angles are shown. The dependence of the number of atoms on the quality of the approximation of a true wide range quadrupole field is clearly visible: The MOT contained the highest number of atoms (3×10^8) for the optimal quadrupole field that is obtained at a 13 degrees inclination of the bias field. To compare the results of the U-MOT, we carried out test experiments with a conventional 6-beam MOT before introducing the atom chip assembly in the apparatus. Neither the loading rates nor the maximum number of trapped atoms exceeded those measured with the U-MOT under similar UHV conditions.

3.1.2 Magnetic Cu-Z wire trap

Though very efficient, optical cooling techniques are limited to ultimately reachable temperatures that do not allow to reach the BEC phase transition directly. This fact and the limits of the various refined optical cooling methods are extensively discussed in the literature [140]. The solution to this problem is to transfer optically cooled cold atoms to conservative trapping potentials and to further cool the clouds after the (dissipative) resonant light has been switched off.
As our actual experiments are based on potentials mainly produced by magnetic fields, we chose to use a magnetic trap for the cooling beyond the limits of optical cooling. The trap is based on a copper Z-wire (Sect. 2.4.8) that is part of the H-shaped structure integrated in the same chip holder as the U-wire used for the MOT (Fig. 3.2).

Trap loading and characterization

In contrast to other atom chip experiments (for example [166]), our copper Z-trap allows us to not directly load the chip potentials from the MOT. Though possible, a direct loading means that only comparably small numbers of atoms can be cooled to BEC because the chip potentials trap a limited phase space volume. This is a consequence of the scaling given in Sect. 2.4.2, namely that larger

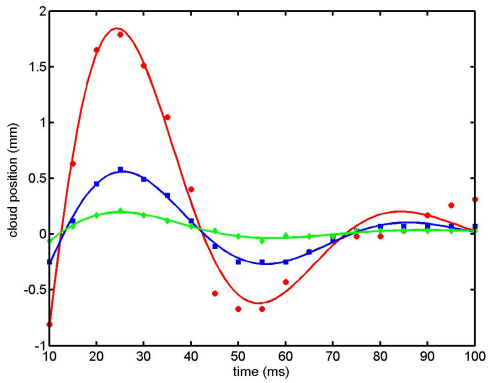

Figure 3.4: Effect of relative displacement of the center of mass of the atom cloud and the magnetic potential it is loaded to. The (quickly damped) oscillatory motion is an effect of poor mode matching. The different data sets correspond to different displacements of the cloud along the longitudinal trap axis. The solid lines are fitted damped oscillations, consistently yielding frequencies of $\nu = 31(1)$Hz, in agreement with the calculated longitudinal trap frequency.

currents in the wire forming the trap allow deeper traps with larger (trapped phase space) volume. Even though we cannot form a trap arbitrarily close to the chip surface, the advantage of the larger currents (60A vs. $\approx$ 2A in chip wires) dominates.

In order to load a maximal number of atoms to a magnetic trap of a given trap *volume*, the phase space *density* before loading should be large. For this reason, we compress the MOT during the final 100ms of near resonant (Doppler) cooling (at the cost of a temperature increase), then turn off the MOT-quadrupole field and again cool the cloud by molasses cooling to 20-50μK. The atom densities at this stage[3] are above 10^{10}cm^{-3} at typical atom numbers of 2×10^8.

After polarizing the cloud by optical pumping to the $|F = 2, m_F = 2\rangle$ state, more than 10^8 atoms can be transferred to the magnetic trap. In the configuration used, the current runs through the innermost possible Z-shaped path where the length of the central bar of the Z is 4mm. This trap is operated with a current of 60A through the wire and a bias field of initially 41G. The bias field is rotated within the plane parallel to the Z-wire by approximately 42 degrees in order to compensate the strong longitudinal field of the two leads of the Z-wire so that only a small Ioffe-field $B_\parallel$ remains at the trap minimum position. The strength of the bias field was chosen so that the finite barrier to the chip surface (1.2mm below the wire center in the direction of gravity) and the barrier against the gravitational potential (equivalent to 15G/cm field gradient for ^{87}Rb) are approximately equal.

Optimal loading (highest atom number at a maximal phase space density) of this trap requires that the molasses cooled cloud is centered with respect to the magnetic potential prior to ramping up the trapping fields (*mode matching*). This is done by adjusting the appropriate field components already during the MOT compression stage. Fig. 3.4 shows examples of a signature of non-perfect mode matching: Once the trapping potential is ramped up, the trapped cloud starts to oscillate at the trapping frequency. In this case, a displacement along

[3] Densities of the order of 10^{11}cm^{-3} are the highest experimentally achieved when additional (more sophisticated) techniques are used [110].

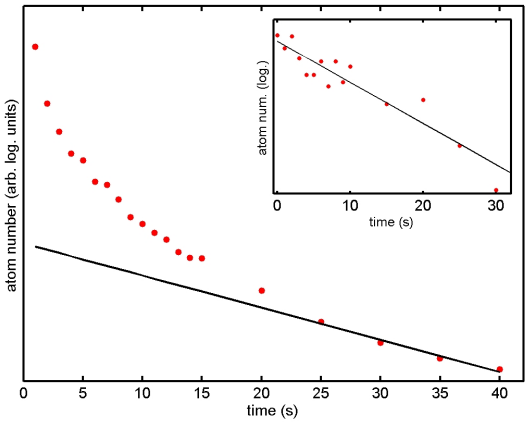

Figure 3.5: Lifetime measurements in the copper Z-trap. An over-exponential loss dominates during the first 10s after loading the trap. This effect can be attributed to evaporation effects as indicated by a coinciding drop of temperature (350μK...150μK, not shown). After 25s only the exponential loss (fitted by the solid line) due to background collisions plays a role. For comparison, the insert shows a lifetime measurement performed in the same trap with colder atoms ($T = 25\mu$K), showing a purely exponential decay of atom number ($\tau = 45$s).

the longitudinal trap axis was induced, so that the slow oscillation frequency of $\nu = \omega/2\pi \sim 30$Hz could easily be resolved.

Even in the case of optimal mode matching, the cloud is severely heated in the trap; the observed temperatures exceeded those measured during the molasses phase by almost an order of magnitude. Yet, the corresponding phase space density is roughly constant ($n_{ps} = \lambda_{dB}^3 n \sim 10^{-7}$) which indicates that the trapping potential is ramped up (almost) adiabatically. The heating effect can be explained by comparing the trap shape to the density profiles of the cold clouds before loading. Both an analytic model calculation and Monte Carlo simulations confirm the observations (details will be given in [81]). As the mismatch of trap shape and atom density profile is most severe in the transverse direction, choosing a Z-configuration with a longer central wire (the H-structure offers various possibilities between 4mm and 10mm) hardly improves the situation. We are currently developing an alternative copper structure to be mounted underneath a next generation atom chip (Sect. 5.3) in which a transverse broadening of the current distribution in the central Z-bar will lead to a transversely broadened large volume trap.

In order to enhance the trap lifetimes to time scales longer than the time needed for the entire experimental sequence, the dispensers are turned off already during the MOT phase and care is taken that the vacuum is pumped to low pressure before the cooling light is extinguished (Sect. 3.1.1). This keeps background gas collision loss rates low. Fig. 3.5 shows typical results of lifetime measurements in the trap. During the first $\sim$ 10s, an over-exponential loss dominates that coincides with a drop of temperature. The effect here is the trap is initially completely filled in the sense that all atoms moving at sufficiently low kinetic energies are trapped but the trapped ensemble is not in thermal equilibrium. Inter-atomic collision events then lead to a thermalization of the cloud, expelling a fraction of hot atoms (*evaporation*). After the thermalization time (25s), the

temperature stays constant, and an exponential decay of the atom number at the vacuum limited rate of $\tau = 1/\gamma > 30$s is restored.

Forced evaporative cooling: BEC formation

To date, the only method that has been used to further cool thermal cold atomic clouds trapped in conservative potentials to BEC is *evaporative cooling*. This simple technique [136] was developed during the years preceding the breakthrough of the first experimental demonstration of Bose-Einstein condensation [1, 42, 24]. The mechanism of evaporation has already been sketched above. By a selective removal of the hottest atoms of an ensemble, the remainder of the cloud is cooled after rethermalization. The procedure works most efficiently, if the condition of expulsion from the trap is isotropic, unlike the above case where the barrier heights are direction dependent. A necessary condition for efficient cooling is also that thermalization happens fast enough, i.e. elastic collision rates are sufficiently high. The collision rate depends on density, thus an adiabatic compression (no loss of phase space density) of the trapping potential allows an effective and fast application of evaporative cooling.

We compress our trap by increasing the bias field to 60G while forced evaporative cooling through a linear radio frequency sweep over typically 5-10s is applied. The radio frequency isotropically induces spin flip transitions to untrapped states for atoms moving with a sufficiently large kinetic energy to reach locations of magnetic fields at the strength necessary for resonant transitions. The trap frequencies are $\omega_\perp = 2\pi \times 150$Hz ($\omega_\perp = 2\pi \times 1.5$kHz) and $\omega_\parallel = 2\pi \times 35$Hz ($\omega_\parallel = 2\pi \times 50$Hz) for the uncompressed (compressed) trap along the transverse and longitudinal[4] axes, respectively. The highest reasonable compression is limited by counter-productive inelastic collisions (mostly three-body molecular recombination processes) that scale strongly with density (Sect. 4.1.1). In our trap the compression is limited by the finite barrier at the chip surface (see above), that can be partially enhanced by passing an auxiliary current through one of the chip wires. During the compression, the transverse trap gradient is increased from 190G/cm to 450G/cm.

After the evaporative cooling, a Bose-Einstein condensate of approximately 10^5 atoms forms at a distance of 400μm from the chip surface. Fig. 3.6 illustrates the increase of phase space density during a typical cooling sweep. As soon as even at the unavoidable loss of atoms, the atom density rises, the so called *runaway* regime of evaporative cooling is reached, and the phase space density increases rapidly as the cooling becomes increasingly efficient. The phase transition to BEC occurs when the phase space density reaches a value on the order of unity.

[4]The longitudinal frequency is naturally higher than it would be if a Z-geometry with a longer central wire had been chosen; higher elastic collision rates thus justify the use of the smallest possible Z.

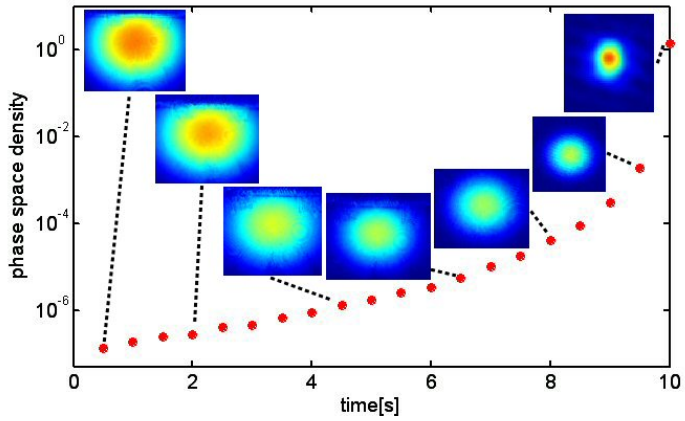

Figure 3.6: Phase space density increase over more than 7 orders of magnitude during a 10s cooling sweep to BEC in the Cu-Z-trap. The inserts show absorption images (10ms time-of-flight) at equal scales (except magnified BEC in first insert from the right). In this example, the trap contained initially $\sim 4 \times 10^7$ atoms at $\sim 360\mu$K. The final BEC contains $\sim 3 \times 10^4$ atoms. The trap changes from essentially linear ($\partial B/\partial r = 400$G/cm) for hot atoms to harmonic ($\omega_\perp = 2\pi \times 440$Hz, $\omega_\parallel = 2\pi \times 40$Hz) for cold atoms.

For our chip experiments, it has turned out that aborting the cooling at temperatures above the critical condensation temperature T_C before the transfer of the cloud to the chip potentials is preferable (Sect. 3.1.3).

3.1.3 Ultracold thermal clouds and BEC in chip potentials

To perform experiments in the immediate vicinity of the surface, we load atoms to various potentials created by wires of different sizes mounted on the atom chip (layout see appendix C). This section summarizes the procedures we use to load these traps with cold thermal and BEC atoms, a detailed account will be given in [98].

Transfer of pre-cooled thermal atoms

Cold atoms ($T \sim 1-10\mu$K), even BECs, can be transferred directly from the Cu-Z-trap (Sect. 3.1.2) to potentials created by currents in chip wires. In (almost) all our experiments we have used one of two basic wire configurations (Fig. 3.7) as intermediate or final trap. Exceptions and other potentials employed in the further course of the experiments are specifically mentioned where appropriate. One of the two basic configurations is based on a broad Z-wire with a cross section of $3.1 \times 100\mu$m^2 and a center to center length of the central wire of 2mm ('100μm-trap'). The other configuration is comprised of two different wires, namely an L-shaped and a U-shaped wire that are arranged in such a way that an elongated Ioffe-type trap very similar to a Z-trap (Sect 2.4.8) is formed ('10μm-trap').

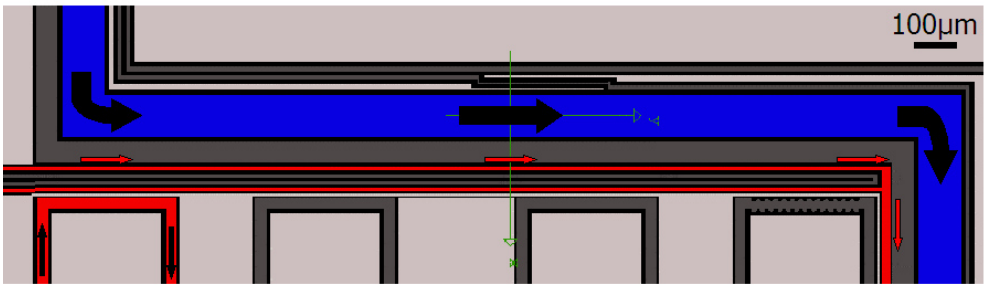

Figure 3.7: The two basic chip traps: The broad (100μm wide) wire (blue) forms a Z-trap, a combination of thin (10μm) wires (red) a similar Ioffe-type trap. Either one of the two parallel thin wires could be used to form a side guide potential, the lead on the right provides one potential endcap in the longitudinal direction, the additional U-shaped wire (bottom left) the other. The parallel current flow (indicated by arrows) in the innermost two leads ensures the Ioffe-configuration without field zero at the trap minimum. The dark gray regions are parts of other wires that are used to form potentials in subsequent stages of various experiments, the light gray areas are grounded parts of the chip's reflecting gold layer. The gold has been removed from the black lines so that the wires are electrically isolated.

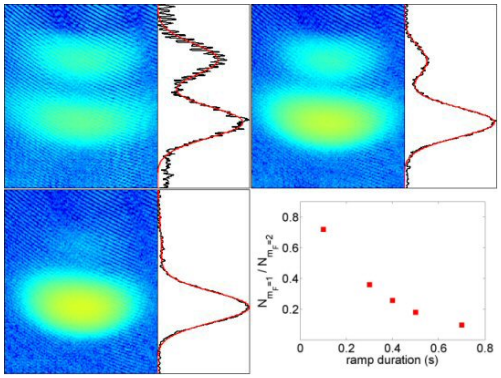

Figure 3.8: Time-of-flight (12ms) images of atomic clouds released from the chip trap directly after the transfer from the Cu Z-trap in the presence of a field gradient (Stern-Gerlach experiment). The fraction of atoms having undergone non-adiabatic transitions to a different spin state ($m_F = 2 \rightarrow m_F = 1$) is plotted as a function of transfer speed. The shown absorption images and density profiles with double Gaussian fits correspond to transfer times of 100, 400, and 700ms, respectively. Using transfer times of 1s safely avoids any unwanted transitions.

Initially, the 100μm-trap was always loaded from the copper-Z trap and the atoms were subsequently transferred to the 10μm-trap if desired. In the course of our experiments it has turned out that the simpler procedure of directly loading the 10μm-trap exhibits no apparent disadvantage.
Regarding the current and bias field ramps and their timing during the transfer process, the principles established in the preceding experiments with ^{7}Li atoms could in general be adopted. As for the pre-cooled atoms ($T < 10\mu$K) all potentials are sufficiently deep, it is usually possible to transfer clouds without losses in atom number. In order to also minimize losses in phase space density, extreme care has to be taken to ensure adiabaticity at all times during the transfer process. This is illustrated in Fig. 3.8: In this experiment, the atoms were released from the chip trap immediately after the transfer by switching off the homogeneous bias field of the trap. The wire current was left on so that the atoms fall

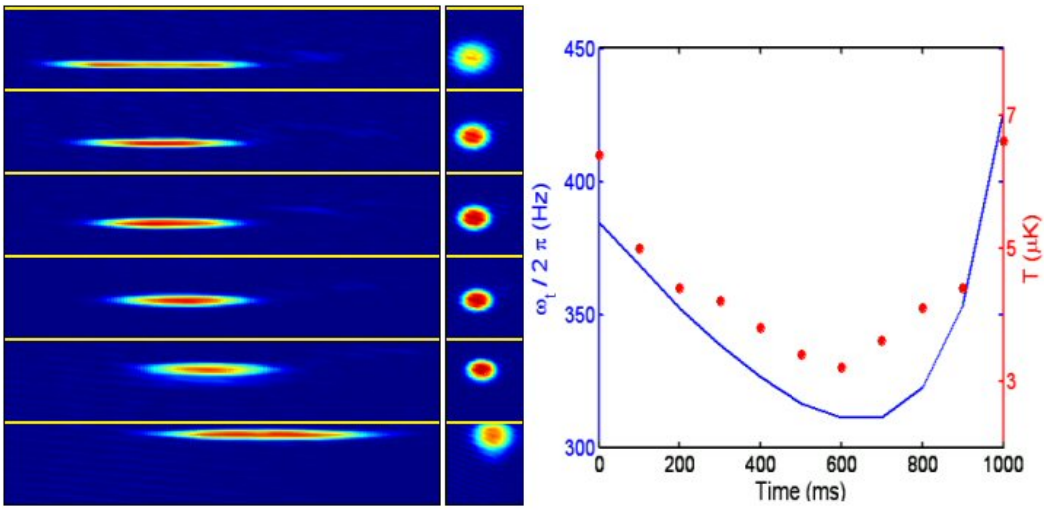

Figure 3.9: Absorption images taken in situ (*left*) and after 5ms time-of-flight (*center*) during the transfer from Cu-Z-trap to the chip. The in situ images are magnified and the transverse direction is scaled up by a factor of 4 with respect to the longitudinal direction. (*right*) Transverse trap frequencies $\omega_\perp$ (blue line) during the transfer and corresponding temperatures (red circles). The adiabatic cooling and heating due to slight changes in $\omega_\perp$ are clearly visible. During the transfer, the atoms are moved towards the chip surface and, due to a $\sim 200\mu$m misalignment between Cu and chip wire, to the right.

in an inhomogeneous magnetic field under the influence of gravity. Like in the Stern-Gerlach experiment [181], atoms in different spin states experience different accelerations and are thus detected at different locations after a time-of-flight period. The experiment was performed for various transfer speeds; too fast potential changes clearly lead to a projection of a fraction of the polarized sample onto other spin states.

In practice, it turns out that moderate losses in phase space density of up to an order of magnitude caused by a slight non-adiabaticity of the transfer are acceptable as the evaporative cooling in the highly compressible chip traps is very efficient. In fact, we are routinely able to produce BECs in both chip traps that contain as many atoms (up to 10^5) as the BECs formed directly in the copper-Z-trap. This is possible even though a rather simple straightforward transfer procedure is used:

First, a parameter set for the target trap is chosen so that the final transverse trap frequency roughly matches that of the initial trap. The ramps are always designed in a way that the current in the chip wire is fully on before the strong current in the copper wire is ramped down. This avoids that the trap minimum is located too close (or even below) the chip surface at any time during the transfer. The adjustment of the bias field components $B_\parallel$ and $B_\perp$ turns out to be quite uncritical with one exception: Care has to be taken that the field at the trap minimum is never so low that Majorana spin flip losses (see Sect. 4.1.2) become

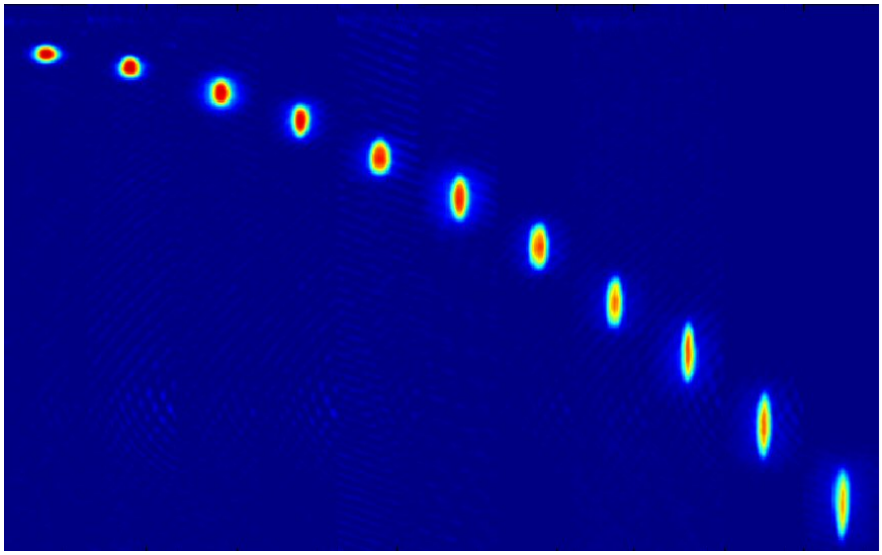

Figure 3.10: Time-of-flight sequence (2ms...22ms, 2ms steps, from left to right) of a BEC released from a chip trap, falling under the influence of gravity. The change in aspect ratio between the extensions in the horizontal and vertical directions, respectively, is characteristic of an expanding BEC. In this example, a current of 2A was driven through the 100μm-Z-wire, the bias fields were $B_\perp = 25$G, $B_{\parallel,\mathrm{ext}} = 1$G which leads to $\omega_\perp = 2\pi \times 1.6$kHz and $\omega_\parallel = 2\pi \times 23$Hz. The number of atoms in the almost pure condensates was $\sim 10^5$.

important; ideally, trap bottom and trap frequencies are held as constant as possible throughout the procedure, but moderate deviations have turned out to be tolerable. A typical transfer sequence from the copper-Z-trap to a chip trap is shown in Fig. 3.9.

Second cooling stage: Chip BEC

The above described transfer procedures can also be applied to BECs. This has been experimentally verified for the 10μm-trap. But as even small residual non-adiabaticity of the process causes loss in phase space density, the transfer is fragile and the conversion of a fraction of a pure condensate into a thermal background is virtually unavoidable. Furthermore, the duration of the transfer (typically a few 100ms) effectively has to be subtracted from the condensate's lifetime (typically $\sim$ 1s).
The transfer of a cold thermal cloud is much more robust and the application of a second radio frequency (RF)-sweep of a duration of 1-2s to reach T_C in situ is unproblematic as the measured lifetimes in the chip traps exceed 10s. The RF can be swept so rapidly because the (transverse) trapping frequencies in the chip traps are tuned to comparably high values of $2\pi \times 1 - 2$kHz by increasing the bias field $B_\perp$. Even higher values would lead to lossy three-body collision events (Sect. 4.1.1). Fig. 3.10 shows a time-of-flight sequence of a BEC released from

the 100μm-trap where it was formed.
It has turned out that the cooling process is quite insensitive with respect to the temperature of a thermal cloud during the preceding transfer. If the starting frequency of the second RF-sweep[5] is adapted appropriately, clouds of different temperatures between $\sim 1\mu$K and $\sim 10\mu$K can be condensed equally well.

3.2 Fragmentation

Shortly after the first BECs had been produced in wire based microtraps [151, 82], the availability of ultracold atoms near current carrying wires lead to the observation of surprisingly large unintended potential modulations [63]. Whenever an atom cloud, either just above T_C or as BEC, was brought close to the surface ($h \approx 100\mu$m), the cloud started to fragment along the longitudinal trap direction. This fragmentation is attributed to irregular current flow in the wire producing the trapping fields.
In the following, an overview of the various experimental findings and their interpretations is given (Sect. 3.2.1). Different models of the origin of the irregularities are compared (Sect. 3.2.2). All the early experiments were carried out near wires fabricated by the wet-chemical technique of electroplating which results in relatively rough wire surfaces and edges. In contrast, our chip fabrication process is purely lithographic, and results in significantly smoother structures (see Sect. 2.2). Consequently, our own measurements of disorder potentials near current carrying wires show a strong reduction of disturbing potentials. In fact, cold thermal atoms ($T > T_C$) are not sensitive enough to show a detectable reaction to potentials stemming from wire imperfections (Sect. 3.2.4). Only if BECs are brought close to the wires ($h < 20\mu$m), small residual disorder is observed (Sect. 3.2.5). It turns out, that BECs near surfaces are such a sensitive tool that the precision of spatially resolved probing of magnetic field variations is at least comparable to conventional methods if not better (Sect. 3.2.6).

3.2.1 Previous experiments

A number of different groups have measured fragmentation effects near current carrying wires. Here, a summary of the published results is given[6].

Tübingen experiment

The first observed fragmentation effects occurred near a standard copper wire ($\varnothing = 90\mu$m) and electroplated copper microwires [63]. The analysis of the

[5] For safety, the RF is kept at a value of 20MHz which does not affect the atoms during the transfer.

[6] The Stanford group (V. Vuletić, now MIT) and the JILA group (E. Cornell) have also reported to have observed fragmentation effects.

data [114] showed a periodically structured potential roughness (main period $\sim 200\mu$m with substructures of higher frequency at closer distances) whose amplitude roughly scaled as $1/h^2$ with distance form the surface (rather than from the wire center) h. The magnitude of the additional disorder field relative to the trapping field amounted to $\Delta B/B \approx 3 \times 10^{-4}$ at $h \approx 100\mu$m. The effect was observed both for cold thermal clouds and BECs at surface distances ranging from 50μm to 150μm. Its origin could be attributed to the wire currents as a reversed current lead to an inversion of the potentials. The same is true for an inversion of an externally applied homogeneous field $B_{\|}$, so that longitudinal field components are necessarily responsible for the disorder potentials.

MIT experiment

Almost simultaneously, a similar effect was reported [122] for sodium BECs that were brought close to current carrying copper conductors ($h = 150...55\mu$m). The typical spacing between the fragmented lumps was $100 - 150\mu$m without a recognizable periodicity. As in all other experiments the local structure of the fragmentation was completely stable in time, so that any experimental fluctuations and drifts cannot be the origin of the additional potentials.

Later, the atomic clouds in traps of nominally identical parameters were compared [123]: A cloud trapped in an optical dipole potential exhibited a homogenous density profile while a magnetically trapped cloud fragmented. This was a clear proof of a magnetic origin of the effect since both traps were separated by an equal distance from a wire, with the only difference that the wire carried a current in one case but not in the other.

Sussex experiment

In this experiment, the fragmentation of cold clouds ($T \sim 1 - 5\mu$K) near a macroscopic copper wire ($\varnothing = 500\mu$m) with outer aluminum and ceramics coatings has been measured [107]. The Gaussian spatial distribution of atoms inside the trap as expected for a perfectly homogenous current flow was observed only if the atoms were separated by more than 100μm from the wire surface. Below that distance, fragmentation effects become increasingly important. The modulation strength of the disorder potential at the lowest measured $h = 27\mu$m amounted to $\sim 4\mu$K, corresponding to a fraction of irregular fields of the order of $\Delta B/B \sim 10^{-3}$. Even at these values of h that are still high if compared to the target value for true quantum control experiments on atom chips (1μm or less), the potential roughness is much higher than tolerable for a controlled manipulation of ultracold, preferably BEC atoms.

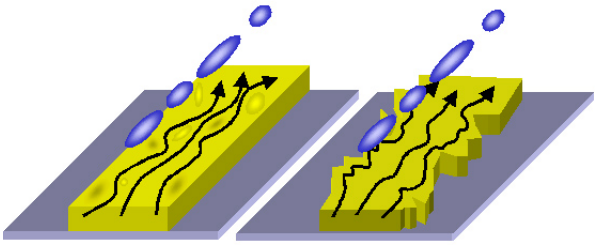

Figure 3.11: Different models for the origin of currents deviating from a straight path. (*left*) Inhomogeneous conductivity of the bulk material leads to locally bent current paths. (*left*) Corrugated wire edges (and homogeneous conductivity of the bulk) lead to strong deviations of the current flow near the wire borders and to a damped influence near the center.

Orsay experiment

A rigorous analysis of disorder potentials measurements has been performed very recently [60]. In these experiments, carried out near electroplated gold microwires, a similar behavior as over the other metals has been found. This makes a material specific origin of the potential roughness unlikely. Measured with thermal atom clouds of varying temperature ($T = 0.4 - 2.2\mu$K), the disorder potentials are observed for $h < 100\mu$m and increase with reduced distance (measured down to $h = 33\mu$m). A spectral analysis shows no pronounced frequencies, so that periodicities can be ruled out. The amplitude of the potentials is slightly lower than in previous experiments ($\Delta B/B \approx 6 \times 10^{-4}$).
For the first time, the origin of the disturbing potentials was not left to speculations in this case. Rather, the very wire above which the fragmentation had been measured was removed from the apparatus and carefully characterized by means of a scanning electron microscope (see images in Fig. 2.2 in Sect. 2.2). Assuming a model of disorder fields arising from a current flow that is slightly altered by wire edge roughness [190], the experimental data could be accurately reproduced in a numerical calculation based on the measured waviness of the wire's boundaries.

3.2.2 Edge versus bulk effects

The above described experiments give strong indication that the observed anomalous potentials can be reduced to an irregular current flow in the wire producing the trapping potentials. Moreover, the disorder has to be attributed to a magnetic field modulation in the direction *parallel* to the path of regular current flow, i.e. to *orthogonal* (planar) components of the current density. The origin of the current flow deviations is not yet fully understood but is likely to stem from fabrication imperfections rather than from specific fundamental material properties.
There are two main effects that can cause non-straight current flow in a straight wire (Fig. 3.11): The first is due to local conductivity fluctuations in the (bulk) metal the wire is made of, the second is roughness of the wire edges.
In [190] results of analytical calculations according to the second model are given.

The assumptions made are small deviations of the wire boundaries from the ideal position, homogeneous material conductivity, and negligible height fluctuations of the wire whose contribution is much smaller than that of width variations. For surface distances $h > W/2$ the relevant integrals simplify and the (root mean square) disorder potential scales as

$$\Delta B(h, F_0) \propto \frac{I}{h} \left(\frac{F_0}{h^3} \right)^{1/2} . \tag{3.1}$$

F_0 is the wire boundary fluctuation correlation function, here assumed to be a constant (white noise). At a constant current, $\Delta B \propto h^{-5/2}$ drops off quickly with distance from the wire, whereas the disorder field in units of the trapping field scales only as $\Delta B/B \propto h^{-3/2}$ under the assumption of a side guide potential (Sect. 2.4.2).
The frequency spectrum of the disorder potential in this model is peaked at non-zero wave vectors k even under the assumption of white noise correlations in the wire roughness. The peak position varies with surface distance and is given by $k = 1.3/h$. The reason is that high frequency fluctuations are damped more quickly with distance than slow ones; long wave length fluctuations are suppressed because uniform shifts to not contribute to the disorder potential.
This scaling behavior is only valid as long as $h > W/2$. For a closer approach of the wire center, the disorder potentials should increase not as strongly since the distance to wire edges, assumed as source of the disorder in this model, decreases less rapidly. In the calculations [190], this effect enters in a geometry factor that can only be calculated numerically.
This model could quantitatively explain the observations reported in [60]. In our case, however, we have strong indication that this is not the case and conductivity fluctuations in the bulk material have to be considered as well (Sects. 3.2.5 and 3.2.6). We have hence embarked on more detailed studies of the edge, bulk and surface studies of our lithographically fabricated wires. We will use such data to develop a refined model which considers both wire edge and bulk conductivity fluctuations.

3.2.3 Height calibration

For all measurements of quantities that depend on (scale with) the distance from the surface h, it is necessary to know h as accurately as possible. Therefore, our method of calibrating h is discussed here, before the experiments investigating disorder potentials in wire traps created by lithographically fabricated wires are described.
For wire potentials, the parameters controlling h are the wire current I and the bias field $B_\perp$ (in the single wire case, Sect. 2.4.2).
In our experiments, we have typically varied I rather than $B_\perp$ to scan h for two reasons: The scaling laws presented in Sect. 2.4.2 imply that the trap frequency

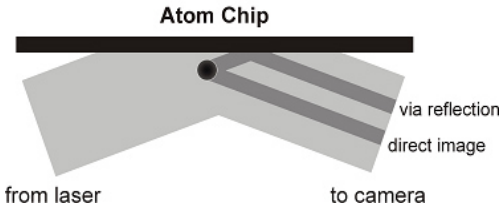

Figure 3.12: Principle of absorption imaging via a reflecting surface. A single atom cloud absorbs two parts of the illuminating light beam, one before the reflection and one after. The distance between the detected direct and reflected images is $2h$ (times the imaging magnification). The angle between light beam and chip surface is exaggerated in this schematic drawing. In the experiments we have worked with angles of the order of 20mrad ($\approx$ 1deg).

$\omega_\perp$ is increased as the surface is approached in any case, but more strongly if $B_\perp$ is increased than if I is reduced. For the measurements of disorder potentials as a function of height (Sects. 3.2.4 and 3.2.5) as well as the lifetime measurements presented in Sect. 4.3 it was advantageous to limit the variation in $\omega_\perp$. Otherwise, $\omega_\perp$ dependent effects, such as three-body recombination processes, potentially mask h-dependent effects.
The other reason is of a more technical nature: The wire current is directly measurable to a high precision by simple means while the bias fields applied by external coils are not. The known currents through the coils and the distance between two coils of a pair together with previously performed calibration measurements [86, 25] only give a rough estimate. Also stray fields in the laboratory are not exactly known (even though they are roughly compensated when optimizing the molasses cooling phase). If $B_\perp$ is fixed and I is varied, an accurate calibration of h is still possible. In the following, our method is described and some examples are given.

Imaging near reflecting surfaces

If h is sufficiently large, that is larger than the imaging resolution (see appendix B), h can directly be measured: If the axis of a horizontal (close to parallel to the chip surface) absorption imaging is slightly inclined with respect to the surface, both atom cloud and its reflection from the gold layer become visible. Fig. 3.12 illustrates this mechanism.
The inclination of the imaging beam results in a standing wave type interference pattern at the atom plane. In addition, Fresnel diffraction from the sharp mirror (chip) edge modifies the intensity profile. For certain h this effect leads to vanishing absorption signals because the light level is too low in dark fringes. This is not problematic as a slight rotation of the imaging axis results in a shift of the interference pattern so that the formerly dark regions become bright and vice versa. At the imaging plane (the CCD plane), the beam that is reflected before the absorption and that reflected after the absorption interfere again.
We use a numerical wave propagation taking into account all effects of Fresnel diffraction and standing wave interference as well as the specific properties of

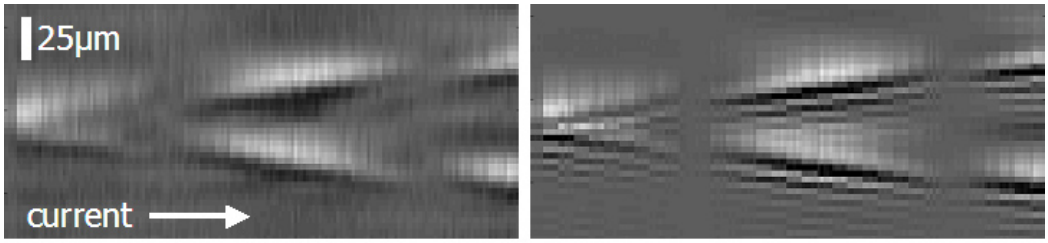

Figure 3.13: (*left*) Experimentally observed in situ transverse absorption profiles of BECs during a current (height) scan. Every column corresponds to a different current, the profiles are obtained by an integration over the longitudinal direction (parallel to the surface). The location of the chip surface is in the center of the image for every column. (*right*) Numerically determined profiles with atomic density and atom position h as only free fitting parameters. The good agreement to the experiment allows to use the fitted values of h as height measure. The higher resolution in the calculated image can be attributed to limited resolution of the imaging.

the imaging lenses to calibrate the exact illumination beam inclination angle α. Once α is known, the measured density profiles can be compared to numerical wave propagation simulations that are calculated for an absorber (atom cloud) positioned at varying h. Fig. 3.13 shows an example of transverse absorption profiles obtained during a scan of h (by scanning I). The experimental data is compared to the simulation where only the atomic density (atom number) and h are left as fitting parameters. The values of h derived from the fit together with the known values of I and the wire width W can now be used to calibrate the bias field $B_\perp$. Currently, we are preparing a publication on the details of the specialties of imaging near surfaces by the technique of inclining the illumination beam [6].

Fitting the bias field

Even though h cannot be measured directly if it is comparable to or smaller than the imaging resolution, the calibration of $B_|$ allows to infer h even for small atom–surface separations using Eq. 2.19. To enhance the accuracy of the fitting procedure and the extrapolation to small h derived form it, we include a number of corrections. These corrections account for specific details of the wire geometry used to form the trap. Fig. 3.14 illustrates an example of the fitting procedure and the effect of the corrections. In this case, the trap was the 100μm Z-trap described above (Sect. 3.1.3). If the heights are fitted to a simple broad wire side guide model (Eq. 2.19), systematic errors are clearly visible in the residuals plot (Fig. 3.14 left). The corrections applied to arrive at a more accurate fit (Fig. 3.14 right) include the finite length of the central wire (Eq. 2.16; changes h by up to $\sim 1.5\%$ for the largest measured h) and field contributions from the leads that connect the Z-shaped wire to the contact pads on the chip edge. The essentially

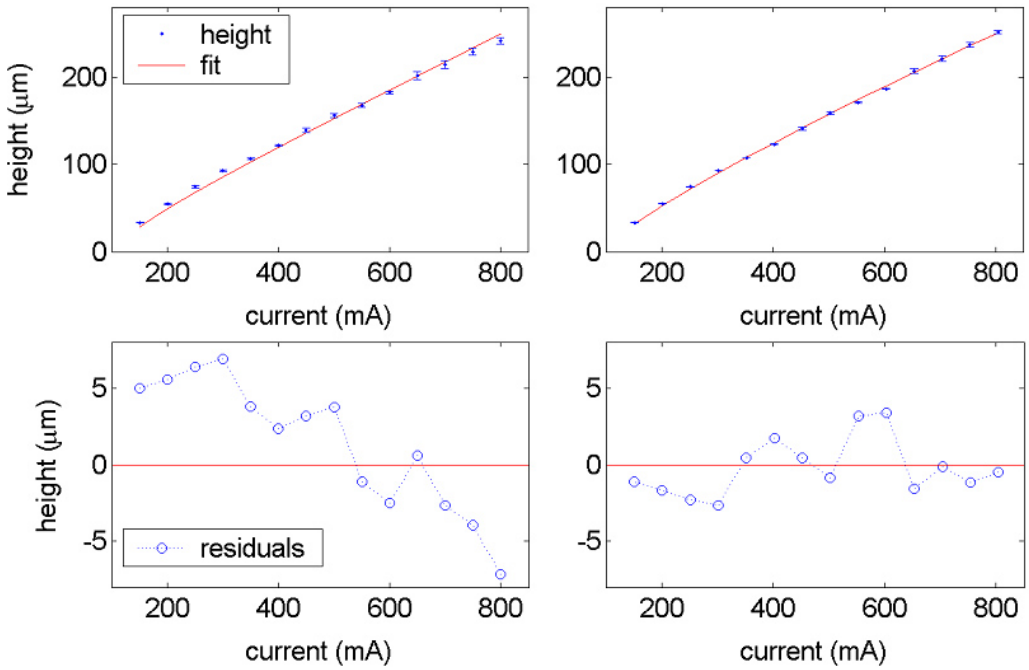

Figure 3.14: Examples of bias field calibration scans. A constant bias field is fitted to the atom–surface distances measured as a function of wire current. (*left*) Simple fit based on a broad infinitely long wire. The residuals (bottom) clearly show a systematic deviation of the data from the model. (*right*) Improved model accounting for the specific geometry of the 100μm Z-trap used in this example (see text).

vertical currents in the wires connecting the chip to the vacuum feedthrough have also been considered, but it turns out that their contribution is negligible. The values we find for $B_\perp$ always agree with the estimates obtained from coil geometry, spacing and currents. A detailed account of the height calibration methods and results will be given in [81].

3.2.4 Thermal atoms near surfaces

In order to characterize the disorder potentials near lithographically fabricated wires, we have moved both cold thermal atom clouds and BECs (Sect. 3.2.5) trapped in the 100μm-trap (connections T–H, see appendix C) and the 10μm trap (connections X–G and A–B for the endcap, see also Sect. 3.1.3) towards the surface by gradually reducing the wire current I. This was preferred over an increase of $B_\perp$ for reasons mentioned in Sect. 3.2.3.
In contrast to the previous experiments (Sect. 3.2.1), we observe homogeneous longitudinal absorption profiles of the trapped thermal atoms, with no detectable dependence on the surface distance h (Fig. 3.15). In both traps no indication of abnormal potentials was found. In order to derive an upper bound for any dis-

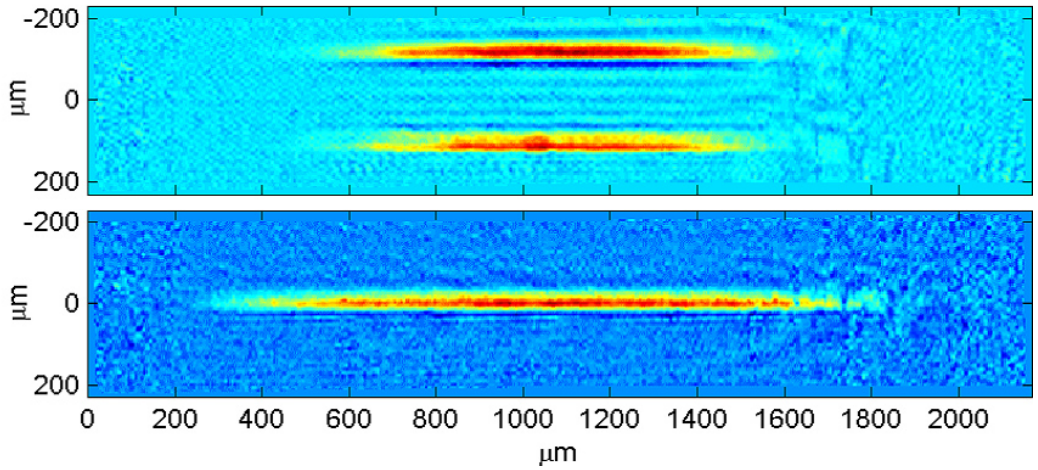

Figure 3.15: Clouds of cold atoms near a lithographically fabricated wire (100μm-Z in this example). (*top*) At large surface distances ($h = 100\mu$m), two images are visible due to the reflection from the surface (Sect. 3.2.3). (*bottom*) Even for cold thermal atoms ($T < 2\mu$K) at $h = 1\mu$m, the density is homogeneous throughout the trap. This cloud is elongated relative to the distant cloud (top) due to the reduced longitudinal confinement in traps near the surface. The fluctuations of the absorbtion signal on the right hand end of the cloud stem from bonding wires obstructing the imaging light rather than from atomic density modulations.

order potentials, we assume a relative atomic density profile following the Boltzmann distribution $n \sim \exp(-V/kT)$. Where possible, we measure the temperature T of the clouds by the regular time-of-flight technique. At low atom numbers this method cannot be used because the densities of the expanding clouds become too small too quickly to yield reliable fitting results. In these cases, T is determined by the cloud's extension inside the calculated trapping potential. This method was compared with the conventional method in traps with sufficiently high atom numbers at various temperatures. The results agreed very well in all cases, so that we conclude that the in situ method is valid. As an additional check, we have calibrated our measured temperatures with the calculated value for T_C and the observed onset of condensation in some cases and found again good agreement.

From the measured temperatures and longitudinal density profile the potential profile is derived. After subtraction of the trapping potential calculated from the wire geometry, any additional potentials should become directly visible. In our case, we find a flat zero line with a residual random experimental noise. The root mean square of this noise can be considered as measure of the detection sensitivity.

At the closest approach of $h = 1\mu$m from the surface of the 10μm wire, where the disorder potentials are expected assume the largest values, a cloud at $T = 1.7\mu$K remains unfragmented within our detection resolution. From the measured residual rms-noise of less than 200nK, we derive the fraction of longitudinal field

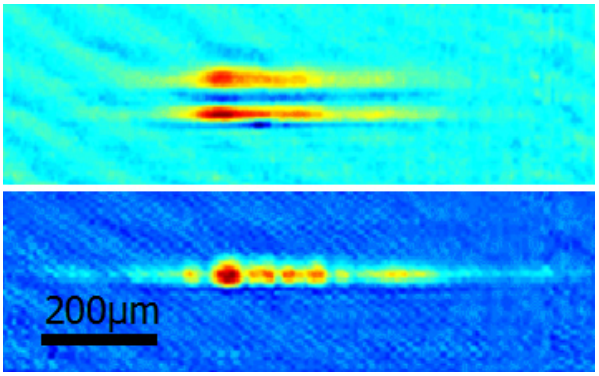

Figure 3.16: In situ absorption images of BECs near the surface of the current carrying 100μm-Z-wire. (*top*) Even a BEC remains essentially unfragmented at a distance of 15μm from the wire. (*bottom*) For close distances ($h < 5\mu$m), fragmentation becomes clearly visible. The detection sensitivity of a BEC is given solely by its chemical potential.

components ΔB to vary by less than $\Delta B/B < 3 \times 10^{-4}$ in units of the trapping field produced by the wire B. By construction, the wire field equals the external bias field at the trap location $B = B_\perp = 10$G. For the 100μm wire we find similar numbers.
Our upper bound for $\Delta B/B$ is significantly smaller than the magnitude of the disorder potentials observed near electroplated wires (Sect. 3.2.1). If the predicted and experimentally confirmed scaling with h is considered, the fact that our upper limit is valid for $h = 1\mu$m while the fragmentation was measured at $h \sim 30\mu$m implies a reduction of the disorder potentials by roughly two orders of magnitude at least.

3.2.5 BEC near surfaces

We use Bose-condensed clouds as more sensitive probes of potential roughness. Fig. 3.16 shows an example of the measured absorption profiles for two surface distances h. As the surface is approached, the trapping potential becomes flatter and the clouds extend over a longer stretch of the wire. For both investigated wires (10μm and 100μm width), the BEC starts to fragment roughly at $h < 20\mu$m. In the Thomas-Fermi approximation, the condensate density is given by the difference of the (global) chemical potential μ and the external potential V. In our case this approximation is only valid in the longitudinal direction of the trap since the transverse single particle ground state energy far exceeds μ throughout the height scan. For this type of one-dimensional condensates, the transverse cloud extension is given by the transverse single particle ground state size. We obtain μ from the overall atom number N derived from the absorption profile (calibrated with ballistic expansion images in some cases), the (global) longitudinal density profile and the calculated transverse ground state sizes. After conversion to the potential and substraction of the trapping potential we obtain the disorder potential profiles.
We have measured the h dependent absorption profiles for BECs near both wires. For these scans, a series of images was taken at each h for statistics. The results for the narrow wire ($W = 10\mu$m) are depicted over a surface distance range from

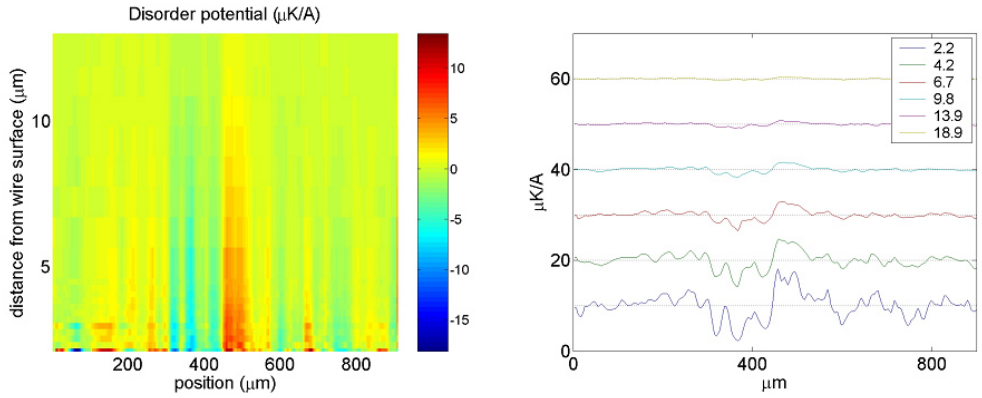

Figure 3.17: Disorder potential profiles for various heights over the narrow (10μm wide) wire surface. For comparison with previously published data, the units are given in μK/A and not in the universal $\Delta B/B$. (*left*) False color image of the disorder potential as a function of position along the wire and height above the wire center. (*right*) Longitudinal profiles of the disorder potential for selected h (given in μm in the legend). Each curve has been shifted by 10μk/A, the dotted lines represent the respective zero potential level.

$2 - 15\mu$m in Fig. 3.17. In this calculation a constant atom number was assumed for all h, even though the integrated absorption signal dropped for low h. This happens due to decreased imaging light intensity near the surface and leads to noisy signals for $h < 2.5\mu$m.

Like in the previous experiments (Sect. 3.2.1), the fragmentation potentials are both stable in time and position. We have verified this also by altering the longitudinal confinement (changed current in the endcap U-wire A–B), thus probing a longitudinally shifted part of the wire. The gradual damping of the disorder potentials as the distance from the wire grows is observed as expected.

For a detailed understanding we have analyzed the spectral properties of the measured disorder potentials (Fig. 3.18). The spectrum shows that high frequency components are only relevant for small h and drop off more quickly with h as the larger scale (small k) variations. This behavior corresponds to the prediction by [190]. Fig. 3.18 also shows that the magnitude of the root mean square (rms) disorder potential strength drops off with increasing h. We find good agreement to a power law behavior where the best fit yields $\Delta B/B_{\mathrm{rms}} \propto h^{-1.2}$ which is close to the predicted $\Delta B/B_{\mathrm{rms}} \propto h^{-3/2}$. An extrapolation[7] to the heights where disorder potentials were previously observed ($h \sim 30\mu$m) shows a $\sim$ 100-fold reduction of the influence of wire imperfections for our purely lithographic fabrication process. We do not clearly observe the expected levelling off, i.e. less rapid scaling with h for $h < W$. This hints at an effect that cannot exclusively be explained by wire edge roughness, but is rather (at least partially) due to bulk conductivity fluctuations. Because the data taken near the narrow wire might not be fully

[7] A direct measurement is not possible since the fragmentation is too small to be detectible.

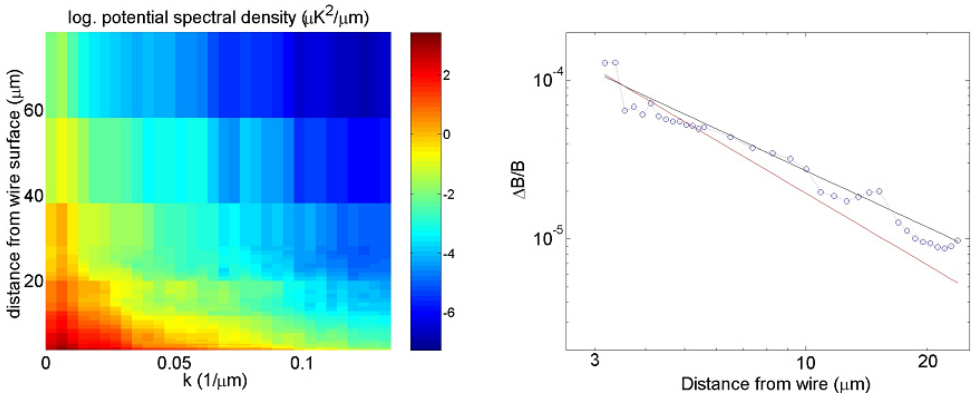

Figure 3.18: (*left*) Power spectral density of the observed fragmentation potentials as a function of surface distance h (scaled to $I = 1\text{A}$). The high frequency components are damped more quickly when h is increased than the slow ones. (*right*) Integrated (rms) disorder potential strength as a function of h in the universal units $\Delta B/B$. The scaling according to the best fit to a power law (black line), yields an exponent (-1.2) close to the predicted $-3/2$ [190] (red line).

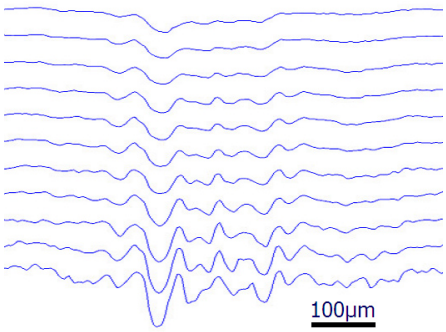

Figure 3.19: Longitudinal absorption profiles for equidistant heights between 15μm and 3μm (top to bottom) over the center of the 100μm wide wire. Even though $h \ll W$ is fulfilled and hence the distance to the wire edges is almost constant, the disorder potential roughness increases. This points to a significant influence of a bulk effect.

conclusive in this respect, we compared the results with those obtained for the broad (100μm wide wire). Fig. 3.19 shows longitudinal density profiles measured for a surface distance range for $h \leq 15\mu$m, i.e. far below the wire width. In this regime, neither the (transverse) trapping parameters nor the global longitudinal density vary significantly. Hence the absorption density profile is a direct measure of the disorder potential. The observed strong increase of the modulations near the wire even at a virtually constant distance from the wire *edges* when the (central) wire *bulk* is approached clearly speaks against a pure edge effect in our case. The applicability of the model outlined in [190] to our case is also discouraged by the fact that we see no qualitatively different behavior of the disorder potentials near the wire edge from that observed over the wire center as was confirmed in a separate measurement.

Currently we are finalizing our analysis on the measured data; the complete analysis results will be summarized in [117] and further publications. At this stage, we

can already conclude that the fabrication process significantly affects the disorder potentials near current carrying conductors and that lithographically fabricated wires have clear advantages over electroplated conductors (several orders of magnitude).

3.2.6 BEC as ultra-sensitive magnetic surface microscope

The high sensitivity of a BEC to extremely small potential variations make it an attractive tool to locally probe slight magnetic field variations. Such microscopic measurements require to approach the surfaces to be investigated to distances on the order of the target spatial resolution. In our experiments we have shown that surface distances of a few microns or less are experimentally accessible (Sects. 3.2.4, 3.2.5, and 4.3). For $h < 1\mu$m, attractive surface potentials start to dominate [131, 138] (Sect. 4.3). The other factor limiting the spatial resolution is the optical imaging. The diffraction limit of our imaging system (appendix B.5) is $\sim 3\mu$m. A 1μm resolution is reachable if appropriate optics with smaller working distances are used. This is currently impossible without changing the vacuum setup. One may speculate to enhance the spatial resolution even further by analyzing interference patterns that arise from optically unresolved BEC density modulations during time-of-flight expansion when the condensate is released from the trap.

The resolution of this microscopy technique regarding the detectable magnetic field variations is only limited by the chemical potential μ of the BEC. In our experimental situation ($\omega_\perp \sim 2\pi \times 3$kHz, $\omega_\parallel \ll \omega_\perp$, $N = 10^3 - 10^4$ atoms at $n_{1\mathrm{d}} = 10 - 100\mu\mathrm{m}^{-1}$), μ can be as small as $k_B \times 100$nK at $h \sim 1\mu$m from a 100μm wide wire which corresponds to a magnetic field difference of $\Delta B_\mu \approx 1.5$mG. Field variations of about a tenth of ΔB_μ are still produce sufficiently large density modulations to be detected; hence relative magnetic field inhomogeneities of $\Delta B/B \sim 10^{-5}$ are resolved. Near broader current sheets BECs with even smaller μ can be held in a less compressed trap, so that the detection limit is further reduced. Translated to current densities, the current sensitivity is sufficient to resolve angular deviations of the current flow of $< 10^{-2}$mrad which corresponds to a current path that differs from the nominal path by a single micron over a length of 10cm.

We have tested this microscopy method by scanning the surface of the broad 100μm wide wire. This is possible by approaching the surface through a wire current reduction as described above (Sect. 3.2.4). Different off-center transverse final positions of the BEC are reached by rotating the bias field during the surface approach. The mapping of the vertical (normal to the chip) bias field component B_v to transverse position is given by Eq. 2.17. In addition to the calculation, we confirm each position of the scan by a direct observation with the vertical imaging (Fig. 3.20, see also appendix B.5). Care has to be taken in adjusting the total bias field strength if the surface distance h is to be kept constant for all

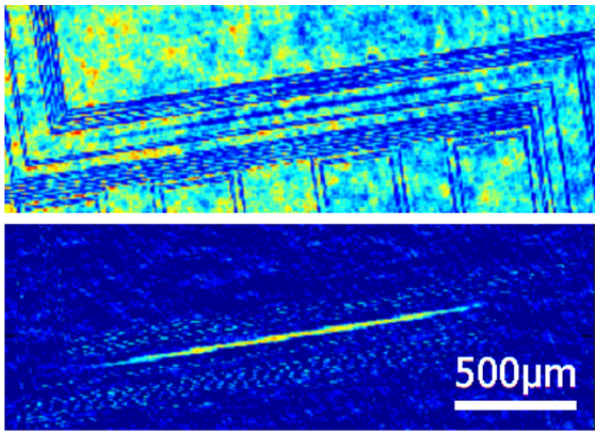

Figure 3.20: The transverse position of an atomic cloud above a broad wire (100μm-Z in this case) can be directly determined by vertical absorption imaging. (*top*) The direct image reveals the features on the chip, the atom cloud is just visible in the center of the central broad wire. The random structures on the mirror surface are speckle patterns. (*bottom*) Processed absorption picture (divided by reference image without atoms): The atoms are clearly visible and the speckle patterns are reduced.

transverse positions. Close to the wire edge, corrections to a constant bias field become particularly important. If h is not constant during the scan, the known scaling behavior of the various frequency components of the disorder potentials (Sect. 3.2.2) can still be used to correctly reconstruct the potential.

Fig. 3.21 gives an example of a scan over the central wire of the 100μm-Z (connections T–H, see appendix C). The images show a reconstructed potential measured at a height of $h \approx 3\mu$m from the wire surface. The fact that the potential is structured over the whole measured range in a similar way points at a true bulk effect that cannot exclusively be explained by a model along the lines of [190]. Wire edge roughness and homogenous conductivity of the wire would rather result in a strongly structured edge region and a decay of the features towards the wire center. The specific properties of the random surface potentials can potentially be exploited, if certain microscopic atom-optical tools are found 'by accident'. For instance, splitting geometries as they are visible in the example image are discussed in Sect. 4.4.4.

Currently we are developing tomography methods to reconstruct local current densities from the measured potential structure. The experimental data contains only information about the changing modulus of the magnetic field that is essentially given by the longitudinal field component $B_{\|}$. Hence a unique mapping to a current density vector field is not possible and the tomography will have to rely on certain model assumptions. The model will be based on a detailed (conventional) microscopic analysis of the wires and their surfaces and more extensive data sets obtained with BECs near various wires at various h.

The combination of good spatial and ultra-high relative magnetic resolution has the potential to make this type of BEC microscopy a useful tool for precision measurements of conductor or magnetic material quality. Even very small local impurities are detectable to an accuracy difficult or even impossible to achieve by alternative methods. Applications could reach as far as the quality control of semiconductor materials where local dopant concentrations could be precisely

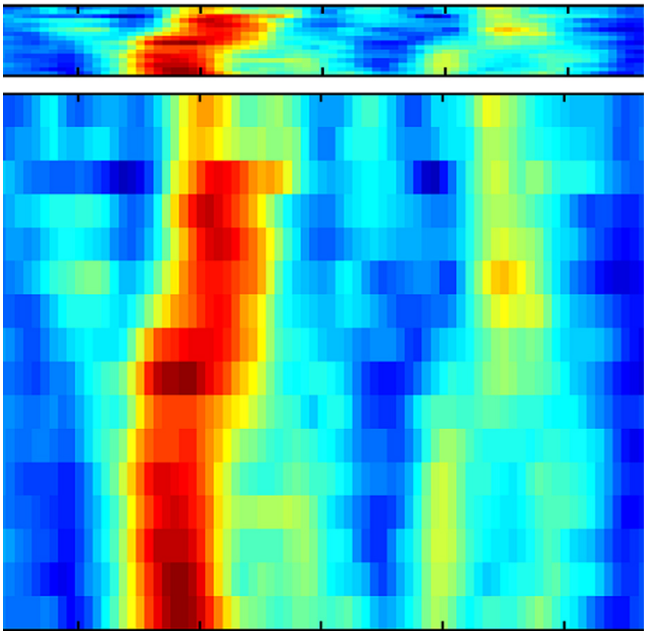

Figure 3.21: Example of a potential reconstructed from a transverse BEC scan of a wire surface at $h = 3\mu$m. Red false color shades correspond to potential wells, blue shades to barriers. The size of the shown scanned area is $30 \times 250\mu\text{m}^2$. (*top*) Image to scale. (*bottom*) The same image with exaggerated transverse (up-down) direction. Note that there are locations where single potentials are apparently split into double wells. Such random features are potentially usable for interferometry (Sect. 4.4.4.)

measured. Existing methods either have the disadvantage of low $\Delta B/B$ resolution (magnetic force microscopes) or of low spatial resolution (high precision magnetometers).

4 Noisy potentials

When ultracold atoms are brought close to the structures that are used to manipulate them, a number of potentially problematic issues needs to be addressed. The role of fabrication imperfections and the resulting disorder potentials are covered in chapter 3. In addition to these static disturbing fields, various coupling mechanisms between the (hot) manipulating structures and the cold atoms have been investigated theoretically [92, 93, 91, 90] and experimentally [107, 84, 131]. We have reviewed and extended the theoretical research and adapted it to the experimental situation [62, 90]. In this chapter, the results are summarized (Sect. 4.1), an overview of the experimental confirmation found in other groups is given (Sect. 4.1.4), and the status of our own experiments that are currently being performed is reported (Sects. 4.3 and 4.4). At this stage, it is possible to combine the results regarding achievable trapping parameters discussed in chapter 2 with the loss, heating and decoherence rates encountered near surfaces. Scaling laws taking the known effects into account are discussed in Sect. 4.2.

Neutral atoms are chosen as physical system for the atom chip experiments mainly due to their intrinsicly small coupling to the environment and the resulting small decoherence rates and small influences of other disturbing mechanisms hindering the ability of a controlled quantum evolution. Still, any remote coupling mechanism between hot surface and cold atom will lead to an energy exchange due to the extreme temperature difference. In fact, the temperature gradients in our experiments where Bose-condensed atoms at a temperature of the order of $T \sim 100$nK are separated from a $T \sim 300$K surface by a micron or less, i.e. a temperature difference of 15 orders of magnitude or more per meter, are probably the largest ever created in a laboratory. Even if no energy is exchanged, disturbances of the phase evolution of matter waves can be induced by a coupling to the surface, leading to decoherence.

4.1 Rate equations

There are three main destructive mechanisms disturbing the matter wave evolution on atom chips that have to be controlled:

- *Trap losses*: It is crucial that we are able to keep the atoms inside the trap for a time that exceeds that of the respective experiment being attempted.

- *Heating*: Transfer of energy to our quantum system may result in excitations of motional degrees of freedom (e.g. trap vibrational levels), and consequently in multi-mode propagation which would render the evolution of the system ill-defined. In extreme cases, heating also results in trap losses if the thermal energy gained is high enough to allow the atoms to leave the (shallow) trapping potentials.

- *Decoherence* or (irreversible) dephasing as it is sometimes referred to also originates from coupling to the environment. While heating requires the transfer of energy, decoherence is more delicate in nature [180]. Nevertheless, the effect is just as harmful because superpositions with a definite phase relation between different quantum states are destroyed.

Quantum optics with neutral atoms has the advantage that the behavior of the atoms regarding these processes is favorable over other systems in free space. The proximity of the surface, however, changes this to some extent. In the following, the various loss, heating and decoherence rates due to different mechanisms are elaborated upon. It turns out that most effects, especially those not related to surface induced processes, are controllable by simple means (Sects. 4.1.1 and 4.1.2). The dominant remaining mechanisms stem from thermal current noise in metallic surfaces that couples to the spin of the atom via oscillating magnetic fields (Sect. 4.1.3).

4.1.1 Negligible effects

A number of harmful processes may play a role under certain circumstances but are unimportant if the experimental conditions and parameters are set correctly. Some of these effects are mentioned here and their respective relevance is discussed.

Finite trap depth

If a trapping potential is compressed without increase of trap depth or in general altered in a way that the trapped phase space volume is reduced, care has to be taken regarding (classical) *spilling* of atoms over the potential barrier. This loss mechanism concerns the hottest atoms, and can thus be used as a technique for (low dimensional) evaporative cooling [132]. In most of our experiments with ultracold thermal atoms ($T < 5\mu$K) and BECs, the traps are typically much deeper than needed to avoid spilling effects. At very close distances to the surface, however, the barrier to attractive van der Waals potentials can become so small that this is not true anymore (Sect. 4.3). In such a case, if the barrier is small and narrow, *tunnelling* to the surface potential may also play a significant role. In [160, 172] it has been estimated that tunnelling effects are negligibly small down to surface distances of $\sim 1\mu$m.

Trap loading and transfer

During an experimental cycle, typically many changes of the confining potential take place. The small chip traps are loaded in a sometimes complex procedure containing whole series of different steps in order to smoothly transfer a cloud to the actual experimental site (Sect. 3.1). Whenever the atoms experience a change of potential, the ensemble temperature is altered. In this context, a compression of a trap leads to heating and a relaxation to cooling. These processes are not harmful as long as the potential changes happen *adiabatically*, i.e. slowly on the timescale given by the slowest trap eigenfrequency. In this case every atom maintains its quantum (vibrational) state, and neither decoherence nor heating in the sense of destruction of the controlled quantum evolution take place. If the potentials are changed too fast, uncontrolled excitations to higher vibrational levels or even transitions to other internal atomic hyperfine states can take place (see example in Sect. 3.1.3).

Collisional losses

Collisions of trapped atoms both with background gas atoms in the vacuum chamber and with other trapped atoms can cause loss and heating processes. Background gas collisions are completely avoided for all practical purposes if the pressure inside the vacuum chamber is sufficiently reduced. We have observed background gas limited trap lifetimes of > 30s, i.e. times that are long compared to any timescale of the experiments. This corresponds to pressures of $\leq 10^{-11}$mbar in our chamber [9].
Cold collisions between trapped atoms is a field of research in itself [191] that cannot be thoroughly covered in the framework of this thesis. In summary, there are *spin exchange* collisions, i.e. total m_F (but not F) conserving binary inelastic collisions, *spin relaxation* collisions (inelastic binary collisions without total m_F conservation) and three-body recombination processes. The spin exchange collisions are forbidden for polarized samples as used in our ^{87}Rb experiments ($|F = 2, m_F = 2\rangle$). They are even not important for spin mixtures of this isotope due to an accidentally small difference between the singlet and triplet s-wave scattering lengths. This fact has for example been exploited in experiments with mixed hyperfine species condensates [143, 108, 113] and spinor condensates [170]. Spin relaxation is also forbidden to first order and can only happen if the nuclear spin is flipped. The corresponding rates are accordingly small [32, 108, 185, 191]. While the binary processes result in loss rates proportional to the density (n), losses due to three-body recombination scale with n^2. This implies that even though the cross sections for three-body collisions are much lower than for binary collisions, three-body processes dominate at high densities. The mechanism here is the formation of a molecular dimer assisted by a third atomic collision partner that is needed in order to assure energy and momentum conservation [191]. We

have not yet observed this type of process as the main loss mechanism for ultracold thermal and BEC samples[1]. However, it is likely that three-body processes play in important role for these atoms in confined traps near the surface.

Stray light

All magnetic and electrostatic potentials on atom chips are so shallow that the energy of only a few resonant or near resonant photons absorbed by a trapped atom is sufficient to cause significant heating and even to remove the atom from the trap. As near resonant laser light of an intensity in excess of the saturation intensity is used in the experimental cycle to cool the atoms before they are loaded to the chip traps, extreme care has to be taken to extinguish all cooling light completely during the magnetic trapping.
In our experiments, the reduction of the resonant light level by a factor of $\sim 10^{-6}$ by means of a double pass AOM (appendix B) in addition to a mechanical shutter was not enough to reach magnetic trap lifetimes τ of more than 10s. Only after the vacuum chamber was entirely separated by completely opaque material from the laser and acousto-optic frequency preparation setup of the apparatus, $\tau > 30$s was reached.

Blackbody radiation

Turning to effects specific for the surface proximity, the cold atom-hot surface coupling could be induced by blackbody radiation. However, it turns out that the blackbody radiation is completely negligible with respect to the magnetic near field radiation (Sect. 4.1.3). This is due to the fact that the wavelengths corresponding to the relevant coupling frequencies are much larger than typical atom-surface separations ($d \ll c/\omega$)[2] [90]. Only at large frequencies with corresponding wavelengths smaller than the trap-surface distance ($\lambda < d$) the Planck spectrum becomes dominant. At and above these frequencies (typically THz), possible transitions are rare and the rates negligibly low for room temperature substrates.

4.1.2 Majorana spin flips

In chapter 2, several ways of removing magnetic field zeroes in various trapping potentials are presented. Here, the reason why this is necessary is given.
If the atomic magnetic moment is not able to follow the change in the direction of the magnetic field, the spin flips and a weak field seeking atom can be turned

[1] The experimental signature of three-(or multi-)body losses is an over-exponential decay of the trap population.

[2] Deviating from the convention in chapter 2, the distance of the trapped atoms to the surface is denoted as d throughout this chapter in order to avoid confusion with Planck's constant h.

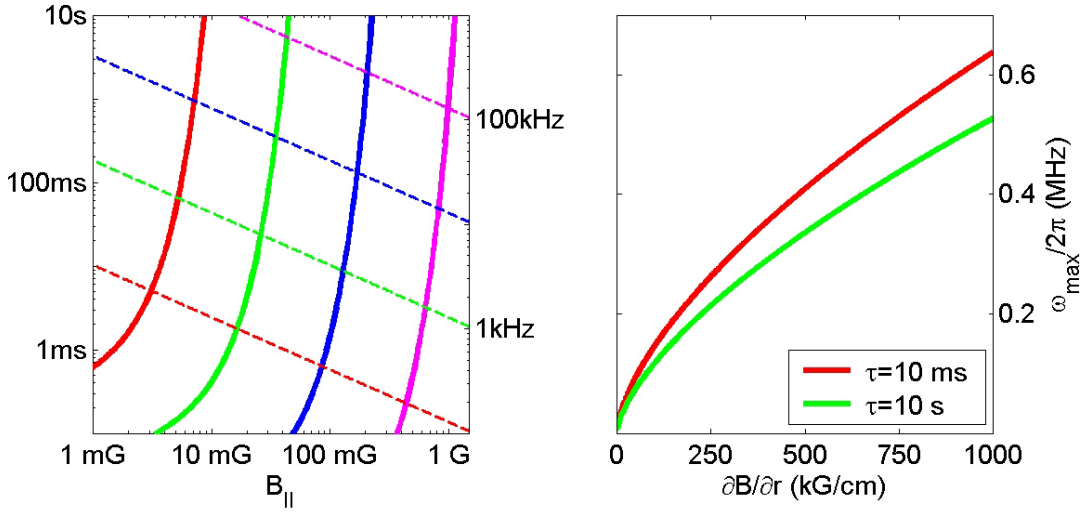

Figure 4.1: (*left*) Lifetimes (solid lines) limited by Majorana spin flips (Landau-Zener transitions) are plotted as a function of $B_\parallel$ for various gradients (100G/cm, 1kG/cm, 10kG/cm, and 100kG/cm; shown as red, green, blue and magenta curves from left to right, respectively). The corresponding trap frequencies ($\nu = \omega/2\pi$) are depicted for comparison (dashed lines). (*right*) The maximally achievable trap frequencies depend on the field gradient at the trap minimum. The scaling is shown for two different target lifetimes.

into a strong field seeker which is not trapped [134, 70]. This occurs when the adiabatic approximation ($\omega_{\mathrm{Lar}} \gg \omega_{\mathrm{trap}}$) does not hold. $\omega_{\mathrm{Lar}} = \mu B/\hbar$ is the Larmor frequency at which the atomic magnetic moment precesses about the direction of the external magnetic field. Majorana flips thus happen at or near zeros of the magnetic field.

For a magnetic field configuration with a zero, losses can be reduced if the atoms circle around it. The loss rate is then inversely proportional to the angular momentum because the latter determines the overlap with the minimum region [19, 95, 129].

In Ioffe-Pritchard traps with nonzero field minimum[3] $B_\parallel$, there is a finite residual loss rate that has been calculated by [183]. For a model atom with spin 1/2 in the vibrational ground state, one gets

$$\gamma_{\mathrm{Maj}} = \frac{\pi\omega_{\mathrm{trap}}}{2\sqrt{\mathrm{e}}}\mathrm{e}^{-\omega_{\mathrm{Lar}}/\omega_{\mathrm{trap}}} \tag{4.1}$$

where $\mu_\parallel$ is the component of the magnetic moment parallel to the trapping field. Note the exponential suppression for a sufficiently large plugging field $B_\parallel$, typical of nonadiabatic (*Landau-Zener*) transitions.

Fig. 4.1 shows some examples calculated according to Eq. 4.1. Even for high gradients and corresponding high trap frequencies (also shown in Fig. 4.1), a

[3] In a time-orbiting potential (Sect. 2.4.7), the average field at the minimum of the average potential $B_{\mathrm{TOP}}(0)$ is equivalent to $B_\parallel$.

value for $B_\parallel$ on the order of 1G is sufficient to suppress Majorana spin flips completely on typical experimental time scales. However, if $B_\parallel$ drops below the respective safe values, the lifetime drops very rapidly. This limits the achievable trap frequencies to a value given by the respective maximal gradients (Sect. 4.2). Eq. 4.1 is strictly valid only for the ground state, excited states have longer lifetimes. This means that the rates given are an upper bound for thermal atoms which are virtually unaffected for ensemble temperatures of $> 10\mu$K.

4.1.3 Current fluctuations in conducting surfaces

When all the effects discussed in Sects. 4.1.1 and 4.1.2 are controlled and the corresponding loss rates are low, the dominant contribution to the atom-surface coupling arises from magnetic field fluctuations. This has been thoroughly discussed in the literature [189, 66, 92, 93, 94, 89, 91, 90], so that here the focus can be put on the consequences for the experiments.
Fluctuating fields couple to the magnetic moment of a trapped atom and can change both its center-of-mass motion (scattering) and its magnetic quantum number m_F (spin flips). Rate equations for these processes can be derived from Fermi's Golden Rule [90]:

$$\Gamma_{\mathrm{i}\to\mathrm{f}} = \frac{1}{\hbar^2} \sum_{\alpha,\beta=x,y,z} \langle m_\mathrm{i}|\mu_\alpha|m_\mathrm{f}\rangle\langle m_\mathrm{f}|\mu_\beta|m_\mathrm{i}\rangle S_B^{\alpha\beta}(\omega_\mathrm{if}). \tag{4.2}$$

The initial and final states are denoted as $|m_\mathrm{i}\rangle$ and $|m_\mathrm{f}\rangle$, respectively, and the transition frequency between them as ω_if. The states can either be different spin states (losses) or different vibrational states (heating). The relevant quantity responsible for the coupling strength is the magnetic field fluctuation (noise) power spectrum

$$S_B^{\alpha\beta}(\omega) = 2\int_{-\infty}^{+\infty} d\tau\, \mathrm{e}^{i\omega\tau} \left\langle B_\alpha(t+\tau)B_\beta(t)\right\rangle, \tag{4.3}$$

at the appropriate frequency ω. $\langle\ldots\rangle$ is a time average (experiment) or an ensemble average (theory). In the following, different sources of this spectrum are discussed and the corresponding rate equations are given.

Thermal noise

Inside a conducting surface at finite temperature, there are fluctuating thermal currents (Johnson or Nyquist noise [106, 147]). These currents induce fluctuating magnetic fields that can couple to nearby atoms in the vacuum. Close to the surface, the fields have substantial non-propagating components that exceed the blackbody spectrum dramatically by many orders of magnitude at low frequencies. This near-field spectrum is comparably flat (white noise) in the relevant

spectral regions, so that the rates are mainly dependent on the atom-surface distance d and on the matrix elements of the respective transitions (Eq. 4.2).
Explicit calculations based on the thermal noise spectrum above a flat conductor surface (half space bulk) result in a *loss rate* given by a fairly complex expression [Eqs. (16), (17), (18), (22), and (35) in [92]] which simplifies in the limits of large and small surface distances [$d \ll \delta(\omega_{\mathrm{Lar}})$ or $d \gg \delta(\omega_{\mathrm{Lar}})$]. The distance setting the scale is the *skin depth*

$$\delta(\omega_{\mathrm{Lar}}) = \sqrt{\frac{2\rho}{\mu_0 \omega_{\mathrm{Lar}}}}, \tag{4.4}$$

i.e. the frequency dependent depth of penetration of electromagnetic radiation into a conductor, or rather the depth out of which radiation emerges from a conductor, in our case. The relevant frequency is the spin flip transition frequency ω_{Lar} (Larmor frequency), ρ is the resistivity of the conductor material. At typical experimental Larmor frequencies, the resulting skin depths are so large (for example $\delta = 75\mu$m for $\omega_{\mathrm{Lar}} = 2\pi \times 1$MHz and room temperature gold[4]) that the interesting distances of single microns and below lie practically always in the low distance limit. Only for cooled substrates (lower ρ) and high ω_{Lar}, a suppression of losses by reduction of δ below d can be hoped for. For example, in the extreme case of $T = 4$K and $\omega_{\mathrm{Lar}} = 2\pi \times 100$MHz, δ is reduced by two orders of magnitude to 750nm. But a strong increase of ω_{Lar} means sacrificing large trapping frequencies and therefore counteracts the drive for strong confinement and localization. The lifetime scaling for surface distances near the skin depth has also been studied experimentally [107, 84] (Sect. 4.1.4), and the theoretical prediction [92] was verified. In particular, the loss rate for $d < \delta(\omega_{\mathrm{Lar}})$ does not depend on ω_{Lar} and is simply given by

$$\Gamma_{\mathrm{loss}}(d) = \frac{\mu_0^2 \mu_B^2 g_F^2 k_B T}{8\pi\hbar^2 \rho} \, |\langle m_{\mathrm{i}}|\hat{S}_z|m_{\mathrm{f}}\rangle|^2 \, \frac{1}{d} \approx 23\mu\mathrm{m/s} \, \frac{1}{d}, \tag{4.5}$$

where $\hat{S}_z$ is the spin operator perpendicular to the (quantization) axis of the trapping field (assumed to point parallel to the surface). The numerical approximation is given for an alkali atom $|F = 2, m_F = 2\rangle \rightarrow |2, 1\rangle$ transition ($|\langle m_{\mathrm{i}}|\hat{S}|m_{\mathrm{f}}\rangle|^2 = 1$) above a gold surface at room temperature.
Eq. 4.5 implies that lifetimes very close to the surface ($d \sim 1\mu$m) are limited by near field noise in the conductor to $\tau \sim 10 - 100$ms. Cooling the chip does not enhance the lifetimes since ρ is roughly proportional to the temperature T and the two effects cancel. Choosing a higher resistivity material, though, does help; in that case, cooling can help to reduce ρ and T simultaneously to allow for the same current densities that were tolerable for the high conductivity material (Sect. 2.3).

[4]Note the error by a factor of $\sqrt{2\pi}$ in Eq. (23) in [62].

Another remedy for short lifetimes is not to change *resistivity* but *resistance* of the current carrying structures by altering the geometry. If the amount of used metal is cut to the minimal amount necessary to drive the needed currents, the loss rates can be significantly reduced. In [91] it has been shown that the term $1/d$ in Eq. 4.5 needs to be replaced by the trace of a tensor that depends on the specific conductor geometry (see appendix of [91]). For a thin conducting layer (thickness $H \ll \delta(\omega_{\mathrm{Lar}})$), for example, a closed expression is obtained and the replacement

$$\frac{1}{d} \rightarrow \frac{H}{d(d+H)} \tag{4.6}$$

needs to be made. For surface distances much smaller than the layer thickness ($d \ll H$), the bulk behavior is recovered, but for larger distances ($d \gg H$), a stronger loss rate scaling of $\sim H/d^2$ takes over. This implies a tenfold enhancement of the lifetime at a distance of 1μm over a 100nm thin metal layer relative to the bulk value. As further improvement is possible if the two-dimensionally large layer is replaced by a wire (scaling $\Gamma \sim R^2/d^3$, R is the wire radius), the use of tolerably small amounts of metal should allow reasonable experimental time scales of the order of seconds even at a surface distance as small as a micron.
The thus far discussed spin flip rates depend on the coupling of oscillating fields to the atom at the Larmor frequency. These losses correspond to atomic transitions with a change in the magnetic quantum number m_F. In principle transitions with higher energy exchange, for example F changing microwave transitions (the hyperfine splitting in ^{87}Rb between the $F = 1$ and $F = 2$ ground states is $\Delta_{\mathrm{hfs}} = h \times 6.8\mathrm{GHz}$), can also be driven, but the rates are substantially lower than for the spin flip rates [92][5].
More important are transitions at typically much lower frequencies, namely transitions to excited vibrational levels of the trapping potential (*heating*). In a harmonic oscillator model (which is approximating the realistic trapping potentials very well if the atoms are sufficiently cold), heating can occur as a result of a fluctuating trap. These fluctuations can either change the trap frequency (*parametric heating*) or the trap position [66, 188]. For sufficiently small surface distances ($d \ll \omega_{\mathrm{Lar}}$), the heating rate (in temperature units) is given by [93]

$$\dot{T}_{\mathrm{atoms}} = \frac{\mu_0^2 g_F^2 \mu_B^2 T_{\mathrm{surf}}}{16\pi M \rho} \; |\langle m_{\mathrm{i}}|\hat{S}_z|m_{\mathrm{f}}\rangle|^2 \; \frac{1}{d^3}. \tag{4.7}$$

This expression has been calculated for traps above planar surfaces of (half plane) bulk conductors and is further reduced for geometries with a smaller amount of metal. But even for the bulk, the phonon absorption rates derived from Eq. 4.7 are smaller than $1\mathrm{s}^{-1}$ for $d \geq 1\mu$m for trap compressions of $\omega = 2\pi \times 100$kHz and

[5] Losses observed close to the surface of fairly high ρ titanium have been attributed to microwave transitions [84].

drop rapidly with increasing heights. The trap frequency does not appear in Eq. 4.7 and enters only through the phonon energy $\hbar\omega$; this means that in compressed traps transitions are suppressed due to the large vibrational energy level spacing. Parametric heating rates are much smaller and only play a role in presence of (relatively strong) technical noise (see below). In conclusion, the influence of loss rates is more severe than that of heating rates, at least for distances on the order of microns and above.

Technical noise

Fluctuating magnetic fields arise not only from thermal electric properties of conducting materials as discussed above. The electric currents generating the trapping fields are also subject to fluctuations that drive spin flips and vibrational excitations. The impact of technical noise can be reduced using active and passive electronic filtering, "quiet" drivers, by correlating the currents for the wire and the bias field etc. This works down to the most fundamental level where the noise due to the discrete value of the electron charge comes into play ('shot noise'). For a current I in free space, shot noise has a frequency-independent spectrum given by

$$SN_I = eI \approx 0.16\,\mathrm{nA}^2/\mathrm{Hz}\frac{I}{\mathrm{A}}, \tag{4.8}$$

where e is the charge quantum. Note that currents in a solid wire can have fluctuations below the shot noise limit because the Coulomb interaction correlates the electrons.
If the wire current in a side guide has a noise spectrum $S_I(\omega)$, the spin flip induced loss rate is given by

$$\Gamma_{\mathrm{loss}}(d) = \frac{g_F^2\mu_B^2\mu_0^2}{h^2}\ |\langle m_\mathrm{i}|\hat{S}_z|m_\mathrm{f}\rangle|^2\ S_I(\omega_{\mathrm{Lar}})\ \frac{1}{d^2}. \tag{4.9}$$

This corresponds to a lifetime of $\tau \sim 100$s for shot noise limited current noise ($I = 10$mA) and a surface distance of $d = 1\mu$m. As the shot noise level scales with the current I (Eq. 4.8), τ grows only linearly with d if d is tuned by adjusting I at a constant bias field $B_\perp$ in a side guide potential (Sect. 2.4.2) and if S_I is always at the shot noise level or a constant multiple thereof. Usually this is not the case because typical power supplies produce currents with a constant noise level S_I that does not depend on I. In this case or if d is tuned by varying $B_\perp$ instead of I, τ grows quadratically with d.
The experimental data available to date indicate that the used current supplies have a quality sufficient to suppress technical noise induced losses to a level below the level of thermally driven spin flips. Our preliminary data (Sect. 4.3) seems to validate this statement also for our setup down to surface distances of $d \sim 4\mu$m. Reducing the losses due to thermal current fluctuations by reducing the amount of metal used (see above) will enforce the requirement for extremely low noise

current sources since the rate given in Eq. 4.9 is independent of the type or amount of material used. For this reason, custom designed ultra-quiet battery driven current drivers have been designed and fabricated in our group [109] and the development of high quality feedback loops is underway.
Eq. 4.7 shows that vibrational excitations (heating) due to thermal current fluctuations take place at relatively low rates, even close to the surface. For such processes, technical noise is dominant since a typical spectrum has a $1/f$ shape, and the relevant frequencies are the trap eigenfrequencies ω that lie in the Hz-kHz range (additional peaks at those frequencies in the noise spectra are not uncommon [25]). Noise at the Larmor frequency (typically MHz) is usually much weaker, so that spin flips are less likely to be driven than vibrational excitations. In a harmonic oscillator model [169, 66] based on the parameters of a side guide potential (Sect. 2.4.2), a transition rate of

$$\Gamma_{0\to 1} = \frac{\mu_0^2 M \omega^3}{4\pi^2 B_\perp^2} S_I(\omega) \tag{4.10}$$

can be derived [62]. Multiplying with $\hbar\omega/k_B$ yields the experimentally measurable quantity $\dot{T}$. Our measured data (Sect. 4.3) of $\dot{T} \sim 300\text{nK/s}$ exceeds the rates predicted by Eq. 4.7 by far and thus has to be attributed to technical noise, either coming from our current drivers or from ambient electromagnetic noise radiated from external sources such as radio transmitters. The data is very similar to that observed in other experiments, for example in [63, 82].
A substantial reduction of the rates given by Eq. 4.10 can be expected if the noise in all wires and coils producing the fields can be correlated (for instance by running all currents in a single serial circuit). This leads to a suppression of center of mass fluctuations inside the trap. The remaining fluctuations translate into fluctuating trap frequencies and can now only cause parametric heating for noise at a frequency twice as high as ω. The corresponding rate has been calculated in [169, 66, 62] and leads to negligible heating rates of approximately $3 \times 10^{-7}\text{s}^{-1} S_I(2\omega)$ for $\omega = 2\pi \times 100\text{kHz}$ and $I = 100\text{mA}$.

Decoherence

Finally, not only loss and heating rates are induced by technical and thermal current fluctuations in the conducting surfaces, but also the coherence of the quantum evolution of matter waves is affected. Uncontrolled transitions to different internal atomic or external trap states naturally imply loss of coherence, too. But in addition to these energy changing processes (*amplitude noise*), field fluctuations can randomize the relative phases in quantum superposition states even without energy transfer (*phase noise*) [180].
The appropriate mathematical treatment makes use of a density matrix formalism where the diagonal elements contain the state populations whose evolution has been discussed above (spin flips and heating). The off-diagonal elements,

sometimes called coherences, describe the quantum correlations of superpostion states and are only measurable as contrast in an interference pattern (Sect. 4.4). The gradual transition from a quantum superposition to a statistical mixture is the decoherence process that is equivalent to a decay of the off-diagonal density matrix elements.

Regarding trapped magnetically polarized atoms, magnetic fields fluctuating in the direction perpendicular to the polarization axis (the trapping field direction) affect the diagonal density matrix elements and lead to losses and heating while fluctuations along the axis cause pure phase noise. It turns out that the near field noise induced by thermal currents is essentially isotropic so that the decoherence rates for internal and motional state superpositions are of the order of the spin flip (loss) and heating rates (see above), respectively, and exhibit the same scaling behavior [90]. For the internal state coherences, the relevant part of the noise spectrum is now the low frequency limit (DC to $1/t$ where t is the time the wave function is in the superposition state). This is less important for the thermal noise that is essentially white, but can be critical for technical noise with a typical $1/f$-scaling (frequency f) and resonance peaks at multiples of the AC-power line frequency.

There are situations in which the decoherence rate can be substantially reduced: Superpositions of internal states with a vanishing differential magnetic moment are insensitive to magnetic field noise because both spin states are equally affected. It was shown in a recent experiment that coherence times in excess of 1s can be reached for superpositions of the $|F = 2, m_F = 1\rangle$ and $|F = 1, m_F = -1\rangle$ of cold thermal ^{87}Rb atoms [187]. The atoms were trapped at a 'magic' field of ~ 3.2G (at the trap minimum) where the magnetic moments of the two states are exactly equal and the residual quadratic Zeeman effect is only $\Delta\nu = 431\text{Hz/G}^2\ \Delta B$. The experiment was performed at a surface distance of only 6μm where the loss rates are on the same order as the measured coherence time.

Spatial coherence is an issue when a wavefunction is delocalized over a distance s. When s is comparable to or smaller than the *noise correlation length* l_c, the exponential decay of the off-diagonal density matrix elements is slowed down by a factor of $1 - C(s;0)$. $C(s;0)$ is the low-frequency limit of the noise correlation function [91, 90]. For a splitting greater than the correlation length, $s \gg l_c$, the correlation function $C(s;0)$ is zero and the superposition decays into a statistical mixture on a time scale given by $1/\gamma$, comparable to the spin lifetime. Superpositions with smaller splitting s decay more slowly, with a rate scaling like

$$[1 - C(s;0)]\gamma \approx (s/l_c)^2\gamma \ll \gamma. \tag{4.11}$$

This behaviour was also found in a decoherence model based on a master equation in Fokker-Planck form [201]. For thermal noise we have shown that l_c is on the on the order of the distance d from the fluctuating currents in the conducting

surface in analogy to the electric near field treated in [89]. In a simple shot noise model where the electrons are assumed to move independently and ballistically, we have found the same to be true for technical noise in a current carrying wire [90].
The status of our experimental efforts regarding the various aspects of coherence and decoherence processes are presented in Sect. 4.4.

4.1.4 Experimental confirmation of predicted loss rates

Over the last two years, the theoretically predicted loss rates of atoms trapped near surfaces have been confirmed in a number of experimental situations. The first published data on lifetime dependence on surface distance [82, 63] already indicated that the lifetimes are reduced as the surface is approached more closely. In the following, a survey of the relevant experiments that have since quantitatively verified the theory is given.

Tübingen experiment

The lifetimes reported in [63] dropped by more than two orders of magnitude with a close to linear scaling from 100s ($d \approx 2$mm) to less than 1s ($d \approx 20\mu$m) as the surface of a microstructure or a macroscopic copper wire is approached. Effects like worse vacuum near the surface or too small potential barriers could be excluded as well as three-body recombination, but relatively strong technical noise might have played a role.

MIT experiment

In the experiments published in [123], such a strong lifetime dependence on the surface distance d was not observed, at least not down to $d \geq 70\mu$m. In order to detect possible effects of technical noise, an optical dipole trap was brought to the same distance from the conductor producing the magnetic trap for comparison. In this case, no different behavior was found, but spin flip transition rates to magnetically untrapped states were directly detected by applying a Stern-Gerlach type technique after releasing trapped clouds from the optical trap. The measured time dependent rates agree well with the scaling predicted for technical current noise. These rates were too small ($\gamma < 0.05\text{s}^{-1}$ at $d > 100\mu$m) to be detected as loss rates from the traps whose vacuum limited lifetimes were of the same order ($1/\gamma \approx 20$s).

Sussex experiment

Thermal noise as source of reduced lifetimes near surfaces could be identified in another set of experiments which were performed close to a aluminum coated copper wire [107]. This wire was large enough to be essentially treated as bulk

metal. It was not only possible to distinguish thermal noise from technical noise by the scaling of the lifetime as a function of d, but also to distinguish two different skin depths (60μm and 110μm). The data that was measured for surface distances ranging between $d \approx 25\mu$m and $d \approx 80\mu$m agrees fairly well with the theory prediction for a flat surface half space bulk. Surprisingly, the experimental data shows *longer* lifetimes than theoretically expected (for example $\tau \approx 2.5$s at $d \approx 25\mu$m). Recently, an improved calculation taking the cylindrical wire shape into account reversed this behavior [167].

JILA experiment

In two experiments performed more recently, clearly thermally induced losses were observed by approaching the surfaces of solids that do not carry currents themselves and thus cannot contribute to fluctuating magnetic fields via technical current noise. In the first experiment [84], cold thermal atoms and BECs trapped in a macroscopic magnetic trap were brought close to different large (bulk) solids of varying material. After subtracting the vacuum (background gas collisions) limited loss rates ($\approx 0.01\text{s}^{-1}$), the conductivity dependence of the lifetimes was observed. Down to $d < 10\mu$m, the lifetime near silicon remained nearly unaffected (> 300s) while the lifetime near titanium and copper exhibited the predicted scaling and magnitude (for example, $\tau \approx 1$s at $d \approx 10\mu$m for copper). No difference between condensates and thermal clouds was detected, the skin depth dependence could again be verified. At $d \leq 10\mu$m, anomalously short lifetimes were measured which probably have to be attributed to additional short range surface potentials. In a later experiment near the same surfaces ($d \leq 10\mu$m), effects of electric fields induced by adsorbed rubidium atoms were observed through resonance frequency shifts of narrow BEC excitation lines [138].

Stanford experiment

A thin metal film (thickness $\approx 2\mu$m) rather than bulk material was approached with condensed and thermal atoms of varying temperatures in the second experiment [131]. After correction for vacuum limited loss rates, the theory is also confirmed in this environment for both a metallic and a dielectric surface. For $d \leq 3\mu$m, a cloud temperature T dependent rapid decrease of lifetimes, particularly above the dielectric surface (Si_3N_4), was measured. The lifetimes at larger d were temperature independent. The observations are consistent with a surface-induced one-dimensional evaporation. Measurements of the T and d dependent fraction of atoms remaining after a fixed evaporation time were consistent with the assumption of a short-range surface potential of the Casimir-Polder type [34, 182].
Table 4.1 summarizes the various experiments, the investigated height ranges and the results obtained.

group	d (μm)	τ (s)	material	noise tech./therm.
Munich [82]	100	1.3	Au wire +	tech.(?)
[187]	5–20	1.6–11	Ag layer	
Tübingen [63]	20–300	0.7–100	Cu wire	tech.(?)
MIT [123]	70–500	25	Cu wire	–
	100–500	20–300	(opt. trap)	tech.
Sussex [107]	25–90	2.5–50	Cu/Al bulk (cylindr.)	therm.
JILA [84]	10–200	1–300	Si,Ti,Cu bulk	therm. (I=0)
Stanford [131]	1.5–11	0.1–1 (2.5)	Cu layer (Si_3N_4)	therm. (I=0)

Table 4.1: Summary of experimentally measured lifetimes near various surfaces. The source of the magnetic field fluctuations responsible for the expulsion of atoms from the trap via spin flips is given as reported in the respective publication. The MIT lifetime data is inferred from a directly measured spin flip rate, the JILA data is corrected for vacuum limited lifetimes. In the Sussex and JILA experiments, the predicted dependence of loss rates on the Larmor frequency (skin depth) was confirmed.

4.2 Wire size scaling

The theoretical considerations and their experimental confirmation discussed above have shown that surface distances down to 1μm can realistically be used for atom chip experiments. Even for the worst case assumption of a half space bulk of metal, lifetimes of the order of $\sim$ 100ms are expected (confirmed by our preliminary data presented in Sect. 4.3) at this distance. For $d \leq 1\mu$m, additional effects related to short range surface potentials play a role (Sect. 4.3) and might hamper the surface approach. These effects include residual disorder potentials due to fabrication imperfections (Sects. 3.2 and 2.2), attractive Casimir-Polder potentials (Sect. 4.1.4 [131]) and inhomogeneous electric fields due to surface adsorbed alkali atoms [138].

Under the assumption of a minimal tolerable surface distance $d_0 \sim 1\mu$m, the results from chapter 2 regarding thermal behavior (Eq. 2.5 in Sect. 2.3) and achievable trap gradients (Eq. 2.20 in Sect. 2.4.10) of realistic rectangular cross section wires can be combined to estimate the limitations on atom chip traps. The resulting scaling of the maximal trap gradient for a given wire (height H, width W) in side guide configuration (Sect. 2.4.2) is

$$\frac{\partial B}{\partial r}(H, W, d_0) \propto \frac{1}{\sqrt{H}} \left[\arctan\left(\frac{W}{2d_0}\right) - \arctan\left(\frac{W}{2d_0 + 2H}\right) \right]. \tag{4.12}$$

For a given d_0, the optimal wire geometry regarding the strongest possible confinement can now be calculated. A numerical solution of the transcendent equations

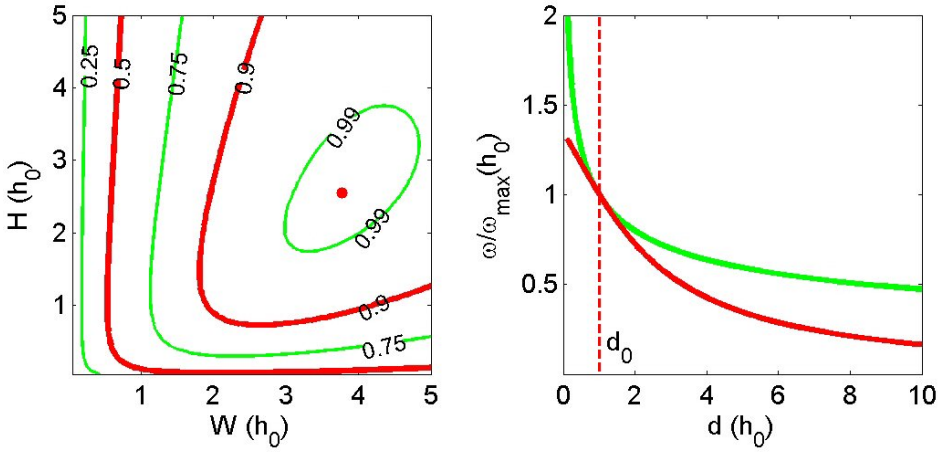

Figure 4.2: (*left*) Dependence of the maximally achievable trap frequency on the wire geometry. The width and height of the wire are given in units of the (minimal) surface distance d_0. The contour lines correspond to suboptimal wire geometries that allow to reach trap frequencies of 99%, 90%, 75%, 50%, and 25% of the maximal frequency that can be achieved for an optimal geometry (red dot). (*right*) Dependence of the maximal trap frequency on d_0 for an optimal wire geometry for each d_0 (green) and for a fixed wire geometry that is optimized for $d_0 = 1\mu$m (red). The distances are given in units of d_0 (red dashed line).

yields

$$\begin{aligned} H_{\text{opt}} &\simeq 2.55 d_0. \\ W_{\text{opt}} &= 2d_0\sqrt{1+\tfrac{H}{d_0}} \simeq 3.77 d_0 \end{aligned} \tag{4.13}$$

Assuming a realistic value of $k = 2.5 \times 10^7 \text{W/Km}^2$ for the thermal conductance from wire to substrate and a safe $\eta \approx 1.5$ in Eq. 2.5 leads to a maximally achievable gradient of

$$\left(\frac{\partial B}{\partial r}\right)_{\text{max}}(d_0) \approx 300 \ \frac{\text{G}}{\mu\text{m}} \times \frac{1}{\sqrt{d_0/\mu\text{m}}}. \tag{4.14}$$

The corresponding maximal trapping frequencies ω_{max} are derivable from Eq. 4.1 (Sect. 4.1.2). Fig. 4.2 shows the scaling of ω_{max} both as a function of d_0 and of the wire sizes for a Majorana spin flip limited lifetime of 1s. For $d_0 = 1\mu$m, ω_{max} exceeds $2\pi\times$1MHz (^{87}Rb) and even for $d_0 = 10\mu$m, $\omega > 500$kHz is possible. These numbers can be enhanced if material conditions are improved and higher current densities are possible as discussed in Sect. 2.3. These results are in agreement with the (differently derived) estimates made in [165].
The use of exactly the optimal wire geometry might turn out to be unfavorable since the influence of thermal noise will be close to that of the bulk (Sect. 4.1.3) and the relatively wide wires prevent small wire to wire spacing. As small deviations from the optimal geometry are not critical (Fig. 4.2), both issues should

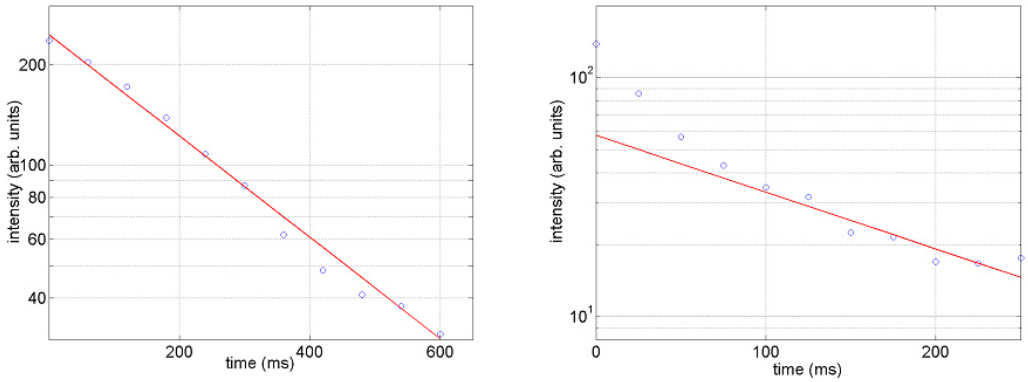

Figure 4.3: Lifetime measurements close to the surface of a current carrying wire. (*left*) For sufficiently large d (here $d = 4.3(6)\mu$m), the decay of atom number is purely exponential. The red line shows a fit with a time constant of $\tau = 286(12)$ms. (*right*) For small distances (here $d = 3.0(6)\mu$m) an initial over-exponential decay, probably due to 'spilling' into attractive surface potentials, plays a role.

not be problematic.

4.3 Lifetimes and heating rates: first experiments

Recently, we have started to measure lifetimes and heating rates as a function of distance from the surface also in our laboratory. In contrast to the previous experiments, the low influence of disorder potentials when the surface of a current carrying wire is approached enables us to accurately investigate the small d regime. Unlike in the experiment presented in [131], the wire producing the trap itself can be approached. This allows to investigate the influence of technical noise in addition to thermal noise. For reference, the influence of thermal noise can still be measured independently when a trap far from the current carrying wire but close to a grounded part of the gold surface is loaded. Such a trap can be formed by rotating the bias field used in a side guide potential to point (almost) perpendicular to the surface.

4.3.1 Lifetimes

Fig. 4.3 shows typical results of our lifetime measurements obtained during a scan of d by varying the current I in the 100μm-trap. The trap and the loading procedure are described in Sect. 3.1.3. So far, we have worked only with thermal atoms at temperatures around 5μK and not with BECs in order to avoid the influence of specific condensate effects that could lead to a more rapid depletion of the trap. The lifetimes are measured at each current by measuring the atom

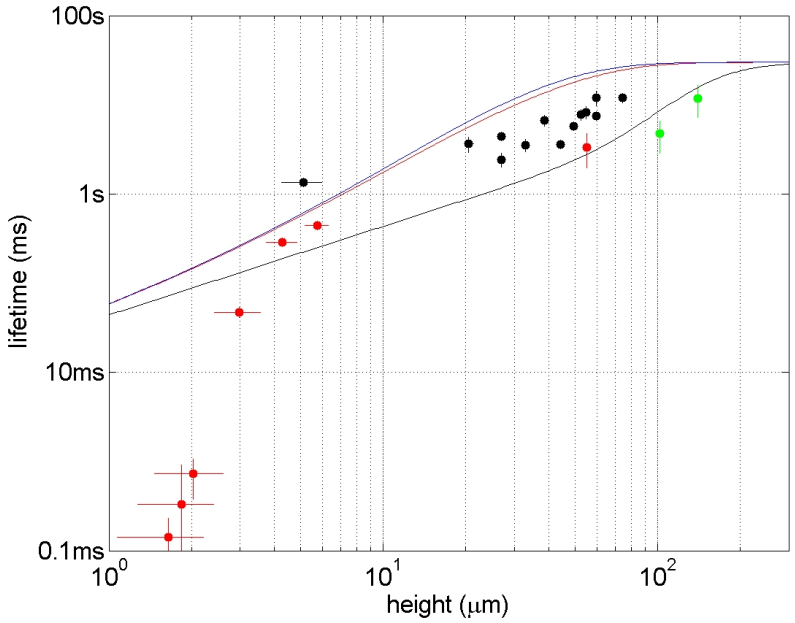

Figure 4.4: Lifetimes measured as a function of distance d from the surface of a 100μm wide and 3.1μm tall wire. The different colors indicate data belonging to different measurement series. The four points representing to the shortest d correspond to (initially) over-exponentially fast decays that can probably be attributed to attractive surface potentials. The solid lines are calculated rates assuming only thermal current noise and a background gas collision limited lifetime of 30s. The calculations were done for bulk (black), layer(red), and wire (blue) geometries. The behavior near the skin depth ($\delta = 75\mu$m, $\omega_{\mathrm{Lar}} = 2\pi \times 1$MHz) is included.

number as a function of hold time in the trap. As the lifetimes vary over many orders of magnitude, the measured time span has to be adapted for every value of d. We have taken care to observe the atom number decay over at least a full decade. The values of d corresponding to the respective currents are determined according to the procedure described in Sect. 3.2.3.

At sufficiently large $d > 3\mu$m, we observe purely exponential decays (Fig. 4.3) that point at a loss mechanism that does neither depend on atom number nor density nor temperature. For $d < 3\mu$m, this behavior changes and an initially over-exponential decay takes over. This effect is likely to be induced by an evaporation towards the surface or rather a spilling into attractive short range surface potentials. Such potentials (Casimir-Polder potentials [34, 131]) have been reported to play a significant role for $d < 3\mu$m. The reason for the initially over-exponential decay is that the hottest atoms are more likely to overcome the small barrier than cold atoms, so that the decay probability is not homogeneous throughout the atom cloud anymore. Unfortunately, the signal to noise ratios in our initial measurements were not large enough to measure the exponential decay that should take over after the hottest atoms have been removed from the trap.

The complete lifetime data set we have measured so far is illustrated in Fig. 4.4. The rapid decay of lifetimes for $d < 3\mu$m is likely to be caused by short range surface potentials (see above). In order to roughly estimate the decay timescales involved, an exponential decay model has been fitted to the atom number decay in spite of the clear deviation of the observation from the model. For comparison, the theoretical predictions of lifetimes limited by thermal current noise have been included in the plot. The different lines correspond to a half space bulk, a layer, and a wire model[6]. The effect of the Larmor frequency for $d > \delta(\omega_{\mathrm{Lar}})$ and the vacuum limited lifetime have been included.
Even though there is no perfect congruence of data and ab initio calculation (no fitting parameters), the data agrees fairly well with the theory. The fact that the measured lifetimes are longer than expected according to the bulk model indicates that an effect of the layer/wire geometry indeed influences the lifetimes positively. The influence of the highly doped, i.e. conductive silicon substrate is neglected in our model and could be responsible for the tendency of the measured lifetimes to be shorter than predicted by the layer model.
Currently, we are acquiring larger data sets of lifetimes near wires of different geometry and near non-current carrying metal surfaces for comparison. We have now implemented an imaging system with higher magnification which allows a more accurate calibration of d so that short range surface potentials can be studied in detail.

4.3.2 Heating

We have also started to investigate heating effects in traps near surfaces. Comprehensive data sets are not yet available, but there are first indications of technical noise induced rates. Fig. 4.5 shows a series of temperature measurements that were obtained by a time-of-flight technique in traps at two different surface distances ($d = 103(1)\mu$m and $d = 142(2)\mu$m). The linear temperature rise observed over a duration of 1.5s (3s) implies a constant heating rate in both cases. The two measured rates differ according to the expectation of a stronger influence of technical noise at higher transverse trap frequencies ($2\pi \times 1.2$kHz versus $2\pi \times 0.9$kHz; see Eq. 4.10).
Future measurements will allow a more quantitative data analysis and theory verification. The source for measurable heating is expected to be virtually exclusively of technical nature (Sect. 4.1.3). A comparison of heating rates near current carrying conductors and metal layers at $I = 0$ should therefore yield significant differences.
As soon as heating effects turn out to limit the experiments, noise correlation techniques as discussed in Sect. 4.1.3 can be implemented to overcome this prob-

[6] In the wire model, the geometry of a rectangular wire is accounted for by the replacement $d \to d(d+H)(d+W)/HW$.

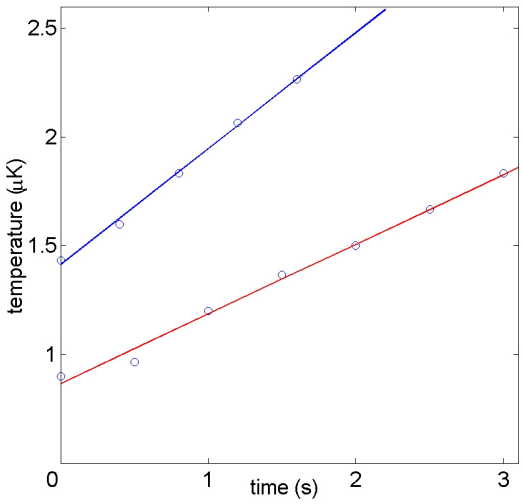

Figure 4.5: Measured heating rates at two different surface distances $d = 103(1)\mu$m and $d = 142(2)\mu$m with linear fits (blue and red lines, respectively). The linear behavior points at constant rates of 530(25)nK/s and 320(24)nK/s, respectively. This difference is predicted for technical noise induced heating in traps with different frequencies.

lem.

4.4 Interferometers

Matter wave interferometry is a large field by itself, thoroughly covered for example in [20]. Atom interferometers have been used for fundamental studies of decoherence mechanisms [38] and interference experiments with molecules of growing size and complexity are undertaken in order to probe the quantum-classical boundary [7]. On the other hand, matter wave interferometers have very practical applications and can be used in precision metrology and as highly sensitive acceleration and rotation sensors [126, 155].

Miniaturized interferometers integrated on atom chips have the advantage of the robustness of the fabrication. This facilitates fundamental experiments and in particular practical applications which are naturally much simpler to be based on microchips than on meter-long atom beam apparatus. Furthermore, experiments in more complex situations can be performed and thus more complex phenomena can be studied. For example, coherence properties in complicated networks may be investigated. By coupling microtraps (atomic quantum dots) to one of the interferometer arms, similar to mesoscopic electron experiments [31], subtle interaction terms such as $1/r$ second-order dipole interactions [149] may be measured.

In the context of the noisy potentials discussed in this chapter, interferometers are planned to be used to study coherence and decoherence effects in the atom chip environment close to conducting (metallic) surfaces. While the first goal is certainly to prove the possibility of coherent manipulation on an atom chip by establishing an interference pattern, the influence of thermal currents in the surface can be studied in detail by observing the visibility (contrast) of the fringes as a

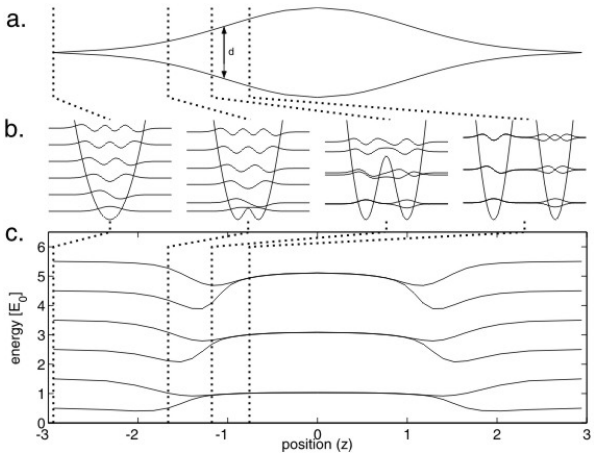

Figure 4.6: Guided matter wave interferometer: (*a*) Two Y-beam splitters are joined together to form the interferometer. (*b*) Transverse eigenfunctions of the guiding potentials at different locations along the first beam splitter. When the two outgoing guides are separated far enough, i.e. no tunnelling between left and right occurs, the symmetric and the antisymmetric states become degenerate. (*c*) Energy eigenvalues for the lowest transverse modes as they evolve along the interferometer.

function of various experimental parameters. These parameters include the surface distance d, substrate type and temperature T, spatial spread of the atomic wave function (delocalization) and additional perturbations that can be introduced in a controlled way. Depending on the type of superposition, i.e. internal hyperfine state superpositions or external vibrational state superpositions, the expected decoherence rates are comparable to spin flip rates or heating rates, respectively (Sect. 4.1.3). While spin flip and heating processes coincide with a transfer of energy, the more subtle effects of phase noise without energy exchange only affect the coherence properties. These effects are exclusively measurable in interference experiments.
The following discussion is focussed on an interferometer designed to probe the coherence of motional (vibrational) states of a guiding potential. First, the concept of a guided matter wave interferometer based on Y-shaped beam splitters (Sect. 2.4.9) is outlined. An implementation on an atom chip and the results of experimental tests of the potentials are presented in Sect. 4.4.2. The section concludes with an overview of implementations of other types of interferometers (Sect. 4.4.4).

4.4.1 Guided matter wave interferometer

In [52], the realization of an interferometer potential based on micro-structured optical dipole potentials has been reported. This configuration has also been investigated theoretically, and the observation of interference patterns even in a multi-mode operation (i.e. with thermal ensembles as inputs) is predicted under certain constraints [115]. In our case, we aim at an implementation of an interferometer for guided atoms based on magnetic potentials. As proposed in [3], two Y-beam splitters can be joined back to back (Fig. 4.6a) for this purpose. The first Y acts as splitter and the second as recombiner.
Concerning the quantum behavior of an (ideal symmetric) Y-beam splitter, co-

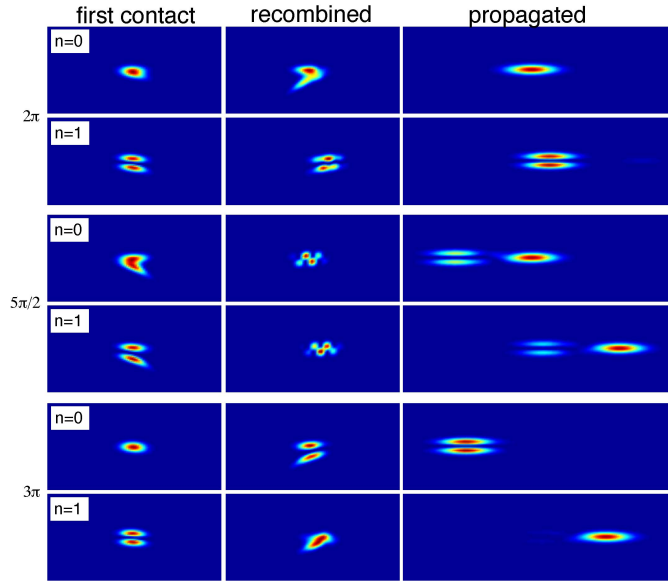

Figure 4.7: Basic properties of a wave packet propagating through a guided matter wave interferometer for $|0\rangle$ and $|1\rangle$ incoming transverse modes calculated by solving the time-dependent Schrödinger equation in two dimensions (x,z,t) for realistic guiding potentials, where z is the longitudinal propagation axis. The probability density of the wave function just before entering, right after exiting the interferometer, and after a rephasing time t are shown for phase shifts of 2π, $5\pi/2$, and 3π. One clearly sees the separation of the two outgoing packets due to the energy conservation in the guide, e.g. for $n = 0$ the first excited outgoing state is slower than the ground state. The slight misalignment between $|0\rangle$ and $|1\rangle$ stems from the different propagation velocities inside the interferometer.

herent splitting for all transverse modes should be achieved due to the definite parity of the system [37]. This was confirmed by a numerical 2-dimensional wave packet propagation for the lowest 35 modes. The 50/50 splitting independent of the transverse mode is an important advantage over four way beam splitter designs relying on tunnelling such as the X-beam splitter described in Sect. 2.4.9. For the X-beam splitter, the splitting ratios for incoming wave packets are very different for different transverse modes, since the tunnelling probability depends strongly on the energy of the particle. Even for a single mode, the splitting amplitudes, determined by the barrier width and height, are extremely sensitive to experimental noise.

The eigenenergies of the lowest transverse modes along an interferometer based on two Y-beam splitters in 2-dimensional geometry[7] are depicted in Fig. 4.6c. From the transverse mode structure one can see that there are many disjunct interferometers in Fock space. Each of them has two transverse input modes ($|2n\rangle$

[7] In two-dimensional confinement the out of plane transverse dimension is either subject to a much stronger confinement or can be separated out. For experimental realizations see [65, 179, 97]

and $|2n+1\rangle$, n being the energy quantum number of the harmonic oscillator) and two output modes. In between the two Y-beam splitters, the waves propagate in a superposition of $|n\rangle_l$ and $|n\rangle_r$ in the left and right arm, respectively. With adiabaticity fulfilled, the disjunct interferometers are identical.
Considering any one of these interferometers, an incoming transverse state evolves after the interferometer into a superposition of the same and the neighboring transverse outgoing state (Fig. 4.6c), depending on the phase difference acquired between $|n\rangle_l$ and $|n\rangle_r$ during the spatial separation of the wave function[8]. While the propagation remains unchanged if the emerging transverse state is the same as the incoming state, a transverse excitation or de-excitation translates into an altered longitudinal propagation velocity ($\Delta v \simeq \pm\omega_\perp/k$ where $\hbar k$ is the momentum of a wave packet moving through the interferometer and $\omega_\perp/2\pi$ is the transverse trapping frequency), since transverse oscillation energy is transferred to longitudinal kinetic energy, and vice versa.
As presented in Fig. 4.7, integrating over the transverse coordinate results in a longitudinal interference pattern observable as an atomic density modulation. As all interferometers are identical, an incoherent sum over the interference patterns of all interferometers does not smear out the visibility of the fringes.

Imperfections of the idealized model

In the model outlined above, a number of idealizations have been made. In the ideal situation, interference patterns with unity visibility are expected even for an incoherent sum over many input momentum states (wave packets of thermal atoms). An implementation of an interferometer cannot meet all of the requirements perfectly. In the following, the assumptions made in the model and the implications for a realistic experiment are briefly discussed:

- The beam splitters should be truly *symmetric*. The scheme relies on the pairwise degeneracy between symmetric and antisymmetric states inside the interferometer where the wavefunctions are delocalized. An asymetric splitting would result in localized states propagating through one or the other arm of the interferometer. In this case which-path information becomes available and the interference contrast is reduced or destroyed. As a Y-wire geometry provides a symmetric beam splitter only if the bias field is perpendicular to the splitting plane (Sect. 2.4.9), we have chosen such a design for our implementation (Sect. 4.4.2).

- The time scales for the eigenenergy changes in the rest frame of the atom are important. On the one hand, *adiabaticity* with respect to the

[8]The relative phase shift $\Delta\phi$ between the two spatial arms of the interferometer can be introduced by a path length difference or by adjusting the potentials to be slightly different in the two arms. In general, $\Delta\phi$ is a function of the longitudinal momentum k.

transverse energy level splitting $\hbar\omega_\perp$ needs to be fulfilled, i.e. the rate of transverse guide displacement $\frac{d}{dt}dz$ (Fig. 4.6a) has to be sufficiently small ($E_{\rm kin}[\frac{d}{dt}dz]^2 \ll \hbar\omega_\perp$). On the other hand, $E_{\rm kin}$ has to be larger than any residual splitting due to tunnel coupling or asymmetry of the pairwise degenerate states inside the interferometer ($E_{\rm tun} \ll E_{\rm kin}$). An analysis based on the multi-wire guide treatment (Sect. 2.4.4 [67]) shows that $\frac{d}{dt}dz$ always diverges near potential splitting points. This problem can be overcome if the region of too fast splitting is small on the scale of the extension of the atom's wavefunction.

- The exactly equal behavior of the multiple interferometers in Fock space relies on equal energy splitting between all input, split, and output modes. This behavior is strictly true only if the potentials are perfectly *harmonic*. Another condition is that the transverse oscillation frequency in the split interferometer arms is twice as large as in the input and output guides ($\omega_{\rm split} = 2\omega_{\rm comb}$) so that the eigenenergies of the pairwise degenerate delocalized states is always the mean of the two corresponding single well eigenenergies. The unavoidable residual anharmonicities in realistic potentials are likely to limit the number of input modes and thus the temperature of the multi-mode sample.

- The model is based on a *pointlike source* of the wave packet. The finite size of realistic traps used as source from which atoms are released to traverse the interferometer leads to a smearing of the interference pattern. Numerical calculations have shown that for a source of 100μm extension, high contrast fringes should still be observable [3].

- The *coherence length* of the wave packet should be longer than the (effective) path length difference between the two interferometer arms. The coherence length is on the order of the thermal de-Broglie wavelength $\lambda = h/p \sim h/\sigma_p$. The relevant momentum spread σ_p is small in this scheme because the sudden release of the wave packet from a pointlike source and the subsequent time of flight detection ensure that the (spatially resolving) detector 'sees' only a narrow momentum class.

- Possibly the most severe deviation of the model from currently performed experiments is the restriction to a single relevant transverse dimension in the model. A realistic level scheme for *two transverse dimensions* is significantly more complex than the one-dimensional scheme shown in Fig. 4.6. In particular, the influence of possible non-adiabatic transitions at (avoided) level crossings remains to be investigated. Again, restricting the number of input modes by using cold atomic samples just above the critical temperature of condensation is expected to facilitate the observation of an interference pattern. 'Freezing out' one of the two dimensions by applying a

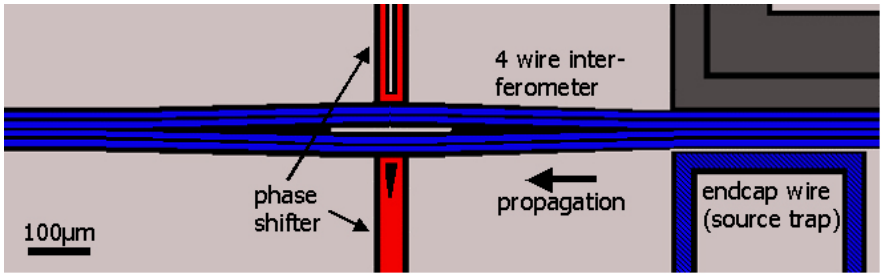

Figure 4.8: Design of a guided matter wave interferometer. This image is directly taken from the design software (DW2000) that is used to operate the ebeam machine writing the lithography masks. The interferometer potential is produced by four current-carrying wires (blue), the red wires are used as electrostatic and/or magnetic phase shifters. The U-shaped wire visible in the lower right hand corner of the image (hatched blue) is used to provide an endcap for the reservoir trap from which the interferometer is loaded. The light gray areas are part of the grounded reflecting gold layer, the dark gray wires are part of the loading region, the black areas indicate regions from which the gold has been removed to define and isolate the wires.

potential with much stronger confinement along that direction, for instance by means of a one-dimensional optical lattice, is an experimental option.

4.4.2 Implementation and potential testing with thermal atoms

In order to be able to perform interference experiments following the guided matter wave proposal outlined above, we have designed the atom chip that has been used in all experiments presented in this chapter and in chapter 3. The design includes a loading region with a number Z- and U-shaped wires of different sizes (10, 50, and 100μm width). The flexibility for the formation of a variety of different Ioffe-Pritchard type traps (Sect. 2.4.8) is large and the longitudinal and transverse confinement can be tuned independently to a certain extent. This is accomplished by a set of additional U-shaped wires on the side of the main wires responsible for the transverse confinement (see Sect. 3.1.3).
Various interferometer structures are accessible from the central trapping region where the atoms are cooled to the desired temperature to be used in the actual experiments (Sect. 3.1). One of the interferometer structures is a guided matter wave interferometer, the other geometries are explained in Sect. 4.4.4.
The gold layer containing the wires was evaporated in two stages, and most current carrying structures have a height of $1.3 + 1.8\mu$m$= 3.1\mu$m. For details of the chip see Sect. 3.1.3 and appendix C where the full design of the chip is shown.
The guided matter wave interferometer we have constructed according to the considerations expressed above (Sects. 4.4.1 and 4.4.1) is described in all details in [67]. The Y-shaped beam splitters are designed as four wire geometry without

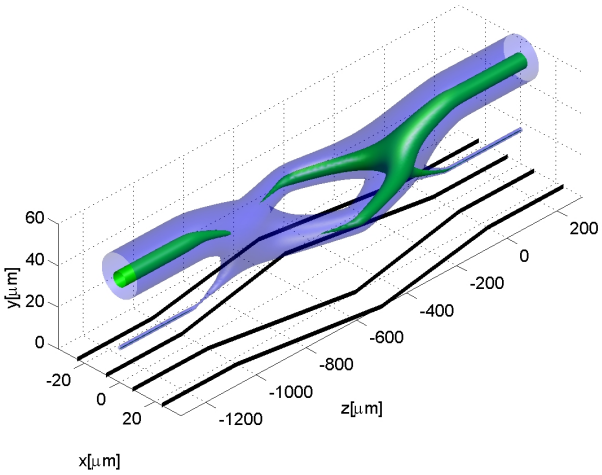

Figure 4.9: Potential of the interferometer. The black lines indicate the current paths, the shown equipotential surfaces have been calculated for $k_B \times 100\mu$K (blue) and $k_B \times 20\mu$K (green). A variation of the longitudinal field component $B_\parallel$ of $\sim \pm 1$G/A (in units of the wire current) leads to the formation of a barrier that prevents cold atoms from traversing the interferometer (hence the closed green equipotential surfaces). The parameters used in this calculation were $I = 0.4$A, $B_v = 8$G, and $B_\parallel = 1$G.

merging wires (Fig. 2.21, Sect. 2.4.9), so that loss channels to the chip's surface are avoided. The interferometer consists of two beam splitters, connected back to back. Two wires approach the split guides near the connection points on both sides of the interferometer. These wires can be charged to apply a tunable momentum dependent phase shift $\Delta\phi = k/2E \int U_{\mathrm{el}}(z)dz$ via the electrostatic interaction (Sect. 2.5). Alternatively, a current can be passed through one of the wires and shift the relative phase by $\Delta\phi = k/2E \int U_{\mathrm{mag}}(z)dz$ via the magnetostatic interaction (Sect. 2.4). The wire layout is depicted in Fig. 4.8.

A thorough discussion of the interferometer potential can be found in [67]. The main properties can be understood on the basis of the general behavior of multiwire (in this case four) guides (Sect. 2.4.4). In the vertical bias field configuration there are always two potential minima above the chip surface that can either be aligned horizontally or vertically, depending on the strength of the vertical bias field component B_v with respect to a critical bias field determined by the (changing) wire separations. The beam splitters are the points where the wire separations change in such a way that a constant B_v becomes overcritical and the vertical splitting is changed to a horizontal splitting[9].

Introducing a longitudinal bias field component $B_{\parallel,\mathrm{ext}}$ avoids field zeroes in the magnetic guides without destroying the symmetry of the beam splitters. It does, however, change the symmetry *between* the two splitters: Around the splitting regions where different non-parallel wires produce the fields, there are non-vanishing varying contributions to $B_{\parallel,\mathrm{wire}}$ from the wires (Fig. 4.9). Together with an external homogeneous $B_\parallel$ this leads to a potential barrier near one beam splitter and a trap near the other, depending on the sign of $B_{\parallel,\mathrm{ext}}$. The height of the barrier

[9] The input and output guides are strictly speaking double guides, but the separation is large enough that the lower guide with its strong compression is practically inaccessible.

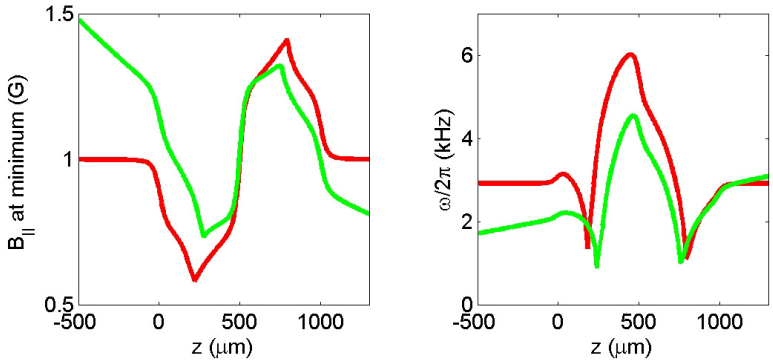

Figure 4.10: (*left*) Inhomogeneities of the longitudinal field $B_{\|}$ lead to a potential barrier inside the interferometer (red curve) that can be overcome by a 'pushing' field induced by a current I_{push} through an additional Cu wire mounted underneath the chip (green curve). The graphs show the remaining (longitudinal) field at the (split) potential minimum along the path of the interferometer ($z = 0$ marks the position of the first beam splitter, negative numbers correspond to the input guide). (*right*) The trap frequency varies over the interferometer and reaches a value approximately twice as large as in the input guide at the position of maximal separation inside the interferometer ($z = 500\mu$m). This behavior (red curve) is altered in the presence of a pushing field (green curve) which slightly changes the compression inhomogeneously. The parameters used for these calculations were $I = 0.4$A, $B_v = 8$G (13G), and $B_{\|} = 1$G (0.1G) in the case of $I_{\mathrm{push}} = 0$A (20A).

only depends on the wire current and the (fixed) splitting angle α, not on $B_{\|,\mathrm{ext}}$. In our case ($\alpha \approx 50$mrad), the value is approximately 1G per Ampere current through each of the wires. In the experiments we used currents of 400mA, hence only atoms with a kinetic energy corresponding to a temperature $T \geq 27\mu$K could pass through the interferometer (see closed equipotential surface for $k_B \times 20\mu$K in Fig. 4.9).

A solution to this problem of cold atoms being prevented from traversing the interferometer is to apply a an *inhomogeneous* additional longitudinal field. In our setup, the simplest way to create such a field was to drive a current through one of the copper wires contained in the structure mounted directly underneath the chip in order to assist the loading procedure (Sect. 3.1). We used a straight wire that runs perpendicular to the propagation direction of the interferometer. This 'pushing wire' is located 6mm from the interferometer (first beam splitter) in the longitudinal direction and 1.2mm below the chip plane. The pushing effect is illustrated in Fig. 4.10 where the field at the potential minimum is plotted as a function of location along the propagation direction.

Results of a test of the potentials with thermal ^{87}Rb atoms ($T \approx 20\mu$K) are presented in Fig. 4.11. The experimental procedure was equal to that described in Sect. 3.1. Cold atoms were transferred from the 100μm-wire Z-trap to the upper minimum of the four wire guide representing the interferometer input guide (Fig.

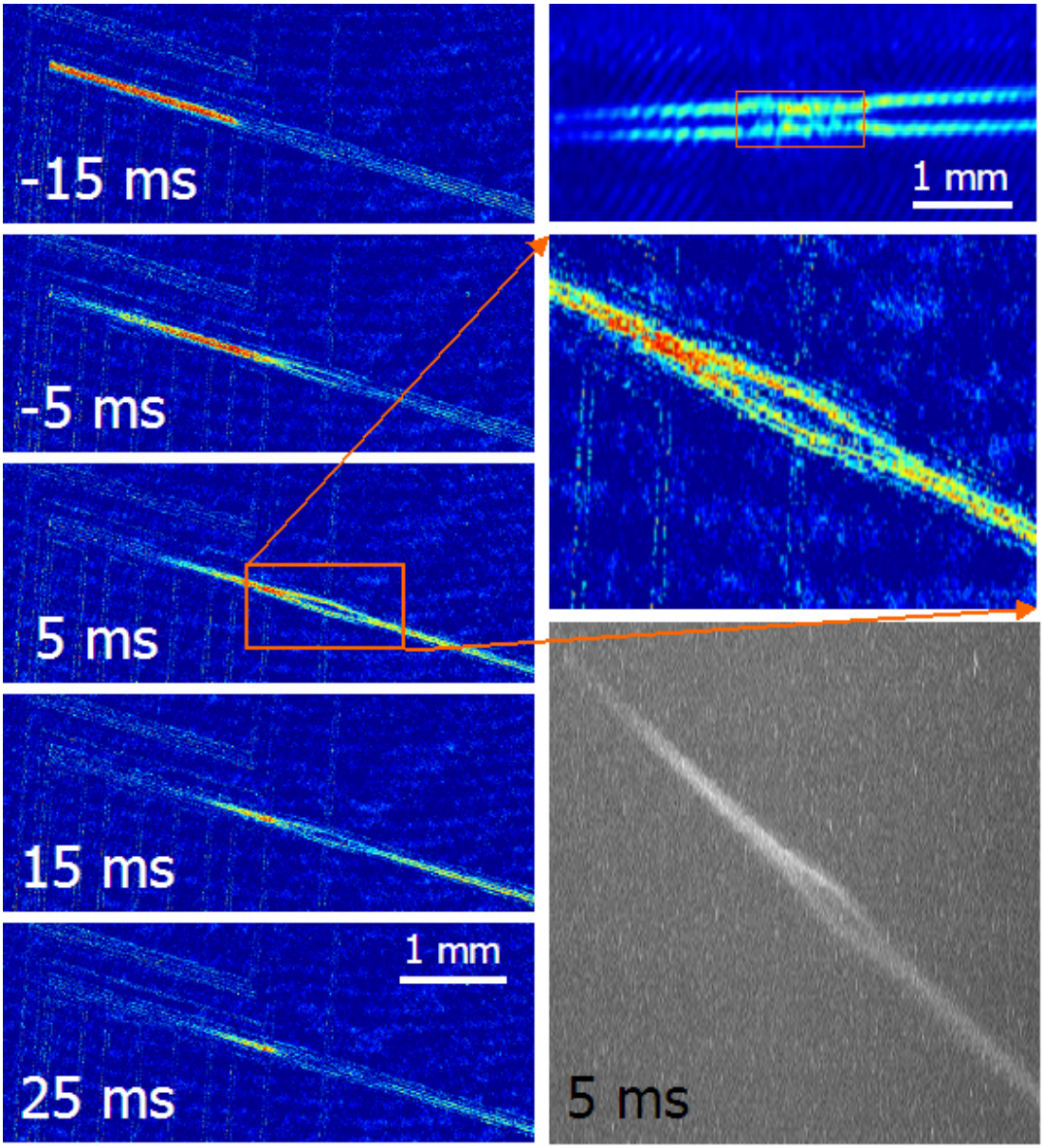

Figure 4.11: Thermal ^{87}Rb atoms ($T \approx 20\mu$K) propagating through an guided matter wave interferometer potential. (*left*) Time sequence of absorption images taken from a direction close to orthogonal to the chip surface. (*top right*) Absorption image taken from a direction (close to) parallel (horizontal) to the chip surface while most atoms are inside the interferometer. Two images are visible due to reflection from the chip surface. The distance to the surface is slightly lower for the split guide than for the recombined potential. The optical access is partly obstructed by bonding wires in the splitting region of the interferometer (orange box). (*bottom right*) Fluorescence image of an atomic cloud propagating through the interferometer. The imaging light is the same as for the horizontal absorption image, the fluorescence light is collected from the direction perpendicular to the chip surface. (*center right*) Enlarged detail of one of the images shown on the right. The direction of propagation in all images is from left to right.

4.8). This potential is closed on the far side (seen from the interferometer) by the wires connecting the four guiding wires and on the near side by an additional current through one of the U-shaped wires on the side of the guiding wires (connections A and B in the full chip design shown in appendix C). The atoms were subsequently released to the interferometer by ramping down the current in the U-wire within 10ms, after a current of 30A through the pushing wire[10] was ramped up. This current was subsequently increased to 45A (within 5ms) so that in fact the complete bias field B_v was provided by the copper wire. Time 0ms in the data plots marks the time when all ramps are completed. The last image, taken 25ms after the release process had been completed, shows that a small fraction of atoms, probably those (cold) atoms that were closest to the interferometer before the cloud was released, remains trapped at the potential barrier inside the interferometer. This effect could be overcome if slightly larger pushing currents were used. An observation of an interference pattern was not expected in these experiments, mainly because the source of the atoms was not (close to) pointlike, but rather a cloud that extended over 2mm in an elongated trap (Fig. 4.11, upper left image). A longitudinally more localized source trap can either be obtained by an appropriate combination of the U-wires on the side of the input guiding wires (see appendix C) as described in [67] or by adding a longitudinally strongly confining dimple by means of electric fields (Sect. 5.1).

The general considerations regarding multi-wire geometries imply that the geometry of the wires already determines at which guide distances from the surface the condition of $\omega_{\mathrm{split}} = 2\omega_{\mathrm{comb}}$ on the trap frequency (Sect. 4.4.1) is fulfilled. In our case these fixed but experimentally accessible distances are 45μm for the input/output guides and 32μm for the split guides. This fact may limit the experimental flexibility, for example for a surface distance dependent decoherence measurement. A deviation from the correct compression (ω) ratio for varying heights, however, is likely to slightly smear out an interference pattern rather than destroying it completely. It should thus be possible to account for such effects in a height scan.

In the numerically calculated potential, the trap frequencies inside the interferometer are non-constant and $\omega_{\mathrm{split}} = 2\omega_{\mathrm{comb}}$ is only reached at the position of maximal separation (Fig. 4.10). As a current through the pushing wire not only produces a longitudinal but also a vertical field component $B_{v,\mathrm{push}}$, the potential is altered in addition to the pushing 'slope': While an adjustment of the external bias field B_v can compensate for the homogenous part, the inhomogeneous part of $B_{v,\mathrm{push}}$ results in a varying height of the guides and thus in varying compression.

[10] As this wire is connected to the copper Z-wire used for the initial evaporative cooling (Sect. 3.1.2), a relay was used as a switch.

4.4.3 BEC in a guided matter wave interferometer

The treatment of the guided matter wave interferometer presented above (Sect. 4.4.1) and in [3] has assumed single particle wavefunctions. Under certain constraints, a multi-mode interference pattern should be observable in this situation. At first sight, the situation should simplify if a BEC were used as a single mode input state. In this case, the detection of an interference pattern does not depend on the exact overlap of multiple patterns. Hence the condition $\omega_{\mathrm{split}} = 2\omega_{\mathrm{comb}}$ does not need to be fulfilled. There are principally two ways to measure the interference effect: The first is to strongly confine the BEC longitudinally before it is released to the interferometer. This leads to a large momentum spread Δk that is equivalent to a wide range of phase shifts imprinted on the propagated condensate. This phase shift translates to a longitudinal density modulation along the lines of the scheme proposed by [3]. The other method is to use a BEC with a small Δk and tune the imprinted phase shift $\Delta\phi$ from experiment to experiment, and record the condensate's position after a defined time of flight.

Regarding the potential design for a BEC interferometer, it is even more crucial to minimize all barriers that have to be smaller than the chemical potential μ of the condensate. Here, changes in the transverse trapping frequency or even changes in the gravitational potential have to be considered. Initial experiments show that even though a BEC is more sensitive to changes in the trapping potentials, it can be accelerated in gradient fields (Sect. 5.1).

The behavior of a BEC in the interferometer will depend on its many-body properties, and the single particle treatment is not valid in all cases. The dynamic splitting of an interacting quantum gas is non-trivial [139]. Similar to the well known Mott-insulator transition [71], the different energy scales need to be compared in order to assess the possibility of a coherent splitting. The relevant energies are the kinetic energy of matter wave propagation, the tunnel-coupling energy, and the on site interaction energy. In a situation of dominating on site interaction the split number state (Mott insulator) is the ground state of the system and coherence is lost.

Currently, the behavior of interacting Bose-gases in guided matter wave interferometers are being investigated [144], and one of the results is that for a relative phase shift of $\Delta\phi = \pi$ between the two parts of a split condensate, an adiabatic formation of a dark soliton excitation is predicted. This soliton is instable and can only be created for an (almost) exact π phase shift.

As the influence of any many-body effect scales with the interaction strength, it could well be possible to perform experiments along the lines of [3] with sufficiently dilute weakly interacting BECs. Tuning the interaction by tuning the atom density would then allow to study additional interaction effects in detail.

Extensions of the theory presented in Sect. 4.1.3 to the coherence of condensates are currently being developed [90, 88].

4.4.4 Other geometries

There is a wide variety of alternative interferometer configurations that can be envisioned on an atom chip. In the following, a summary of some possibilities is given.

Sagnac interferometers

In addtion to the above described Mach-Zehnder type interferometers, guided matter wave interferometers based of ring shaped Sagnac-type geometries are of special interest. Sagnac interferometers are particularly well suited as rotation sensors as the degeneracy of clockwise and counter-clockwise propagating modes is lifted for non-vanishing angular momenta. Matter wave implementations can in principle reach much higher sensitivity than currently commercially available fiber optical devices. Investigations concerning the influence of (unavoidable) residual disorder potentials stemming from fabrication imperfections (Sect. 3.2) on the experimentally achievable sensitivity are currently underway.

Dynamic bias field interferometer

Regarding interferometers in the time domain, i.e. interferometers based on time dependent beam splitters (Sect. 2.4.9), several schemes have been suggested in the literature.
In [97] it has been proposed to use a splitting geometry based on two wires with co-propagating currents as explained in Sect. 2.4.3 to form an interferometer. This scheme operates under the assumption of non-interacting atoms originally populating the trap ground state (non-interacting BEC). Starting from a population in the hexapole minimum, a differential phase shift $\Delta\phi$ is imprinted after horizontally splitting the atomic cloud by increasing $B_\perp$. $\Delta\phi$ controls the relative population of the degenerate symmetric and antisymmetric states in the split potential. The two minima are subsequently recombined and split vertically by reducing $B_\perp$ to below the critical value $B_{\perp,\mathrm{crit}}$. Now the compression of the two minima differs, so that the eigenstates are now the localized states. This implies that the antisymmetric first excited state evolves into the state localized in the lower minimum with the higher ω. The symmetric ground state will in contrast be localized in the upper minimum with the lower ω. The splitting ratio into the two minima will hence depend on $\Delta\phi$ which allows to detect an interference pattern by measuring the population in one or both of the minima as a function of $\Delta\phi$.
We have designed and fabricated an interferometer based on this concept on the chip that also contains the guided matter wave interferometer (Sect. 4.4.1). Fig. 4.12 shows our design: The two 300μm long wires with equal cross section ($1.3 \times 2\mu\mathrm{m}^2$) are connected in parallel to a broader wire configured as a Z in order to provide longitudinal confinement. The wire separation (center to center

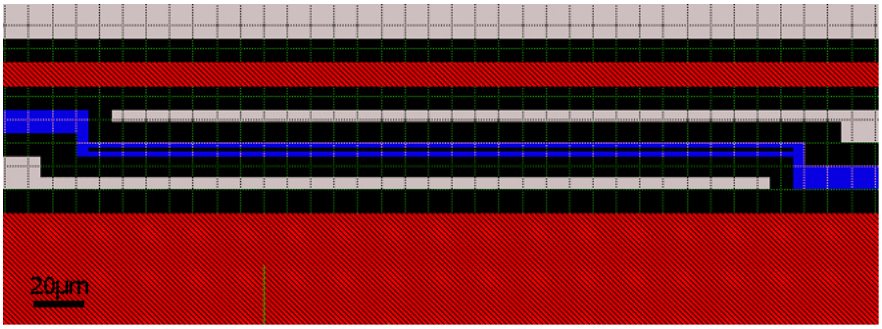

Figure 4.12: Layout for an implementation of a dynamic bias field interferometer. This image shows a design that is fabricated on a chip. The interferometer concept is based on two parallel (2μm wide) wires carrying co-propagating currents. In this design, the two wires constitute the central wire of a Z-wire, so that atoms are confined also along the longitudinal direction. The current carrying wires are colored in blue, the grounded metal patches in light gray, and the gaps defining the wires in black. Phase shifts can be imprinted by passing currents through neighboring wires (hatched red) or by applying charges to them.

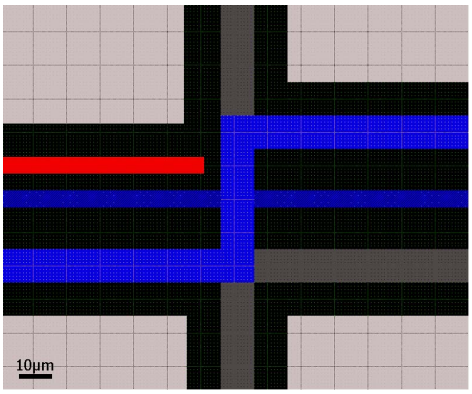

Figure 4.13: A Z-trap potential can be split and recombined by adjusting the current flowing through the central wire crossing the Z (dark blue). The current carrying wires are depicted in blue, the gaps from which the metal has been removed in black, the grounded parts of the gold surface in light gray. The wire shown in red is an electrode that can be used as phase shifter. Some auxiliary wires are not directly used in the scheme (dark gray).

4μm) was chosen to be small enough to maintain reasonable trapping frequencies in the separated wells at sufficiently large tunnelling rates. This is necessary in order to allow an operation speed of the interferometer sequence that should be fast with respect to any decoherence processes.

Split Z-trap double well

Another possibility of an implementation of an interferometer is based on a crossed wire beam splitter (Sect. 2.4.9). An interference pattern is predicted for a population of the ground state of the original trap under the assumption of negligible many body interaction effects [83]. The constraints of adiabatic potential changes that are necessary in order to avoid an uncontrolled evolution into excited vibrational trap levels, have been studied in [83]. The result is again that smaller structures are favorable.
We have also constructed a crossed wire interferometer (Fig. 4.13). As in this

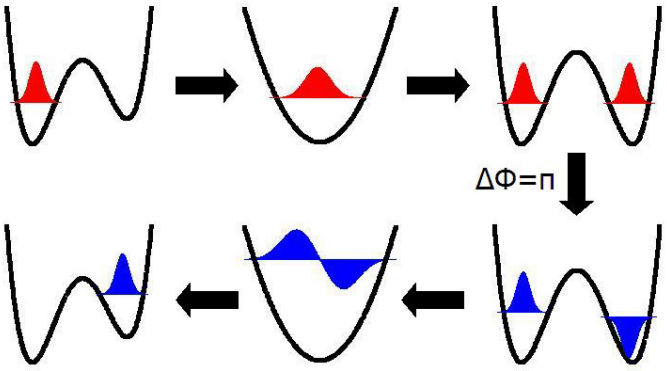

Figure 4.14: Multi-mode interferometer sequence for a split Z-trap geometry. By applying an asymmetry to the double well potential where appropriate, the whole procedure is deterministic and does not rely on accurate timing. In the shown case, a localized state (red) is split and turned into the antisymmetric state inside the interferometer by applying a relative phase shift of $\Delta\phi = \pi$. The population is hence found in the other well at the end of the sequence (see text).

case fast longitudinal trap frequencies are desirable, we chose the basic trap to be a 10μm-Z-trap with a small central wire length (center to center 40μm). This Z is crossed in its center by a thinner (5μm) wire whose current can be tuned to tune the barrier height in the double well potential. An electrically chargeable lead near one of the wells is intended to be used as a phase shifter.

The detection of the interference effect in this configuration (not explicitly addressed in [83]), requires a high imaging resolution on the order of the trap ground state size as the first excited state needs to be distinguished from the ground state by detecting the node plane.

An alternative scheme based on *adiabatic passages* has been proposed [5], and we are currently verifying its feasibility in our design. In this scheme (Fig. 4.14), the phase shifting chargeable lead is used to introduce a differential potential depth of the two split wells where necessary. The interferometer sequence operates as follows: a) One of the two wells in the split potential is loaded with atoms in the (localized) symmetric ground state of this well. b) The potential in the populated well is lowered, so that the wavefunction evolves adiabatically (and thus deterministically) into the ground state of the combined potential when the barrier is lowered. c) The potential barrier is ramped down and the chargeable lead is discharged. d) The potential is split into a symmetric double well. The wavefunction now evolves deterministically into the delocalized symmetric ground state of the double well. e) At a sufficiently high barrier, the symmetric and antisymmetric ground states become degenerate, and introducing a differential phase $\Delta\phi$ by charging the lead (now used as phase shifter) will determine the coefficients of a coherent superposition of both states. f) The potential is recombined and steps b) and c) are repeated in reverse order. g) The relative population of the two wells depends on the imprinted phase shift $\Delta\phi$ and can be detected.

While the experimentally relevant energy and time scales still need to be determined, this scheme has a number of obvious advantages: If certain adiabaticity

criteria are fulfilled, the whole sequence is completely deterministic and does not rely on an exact timing of the various processes. The scheme is based only on arguments of symmetric and antisymmetric states and is hence readily extendable to multi-mode operation as has been confirmed in numerical wavepacket propagations [5]. This means that thermal clouds could be used and many-body interaction effects do not have to be considered. The constraints on the imaging are significantly relieved as the detection of the interference pattern is possible as long as the two wells of the split potential can be spatially resolved. In the split Z-trap geometry, flexible parameter tuning is possible. In contrast to the guided matter wave interferometer, decoherence times can simply be measured by varying the hold time of the delocalized wavefunction and the surface distance can be changed without significantly altering the relevant longitudinal confinement. Finally, the transverse confinement of the potential can be made so strong that a one-dimensional treatment is fully justified.

Splitting in disorder potentials

It has been mentioned above that it is desirable to construct splitting potentials in which the confinement (trap frequency) in the separated wells of the double well potential is high even when the spatial separation is small and the tunnelling rates are high. This implies small structure sizes which are sometimes risky to fabricate because small structures limit the flexibility in the experiments regarding large volume traps and atom-surface distances. One solution to this problem is to build hybrid chips, containing both large wires to form deep trapping potentials comparably far away from the wires and small scale structures for the high resolution potential tailoring. We are currently developing such chips (Sect. 5.3).
In the meantime, the small scale disorder potentials invoked by fabrication imperfections discussed in Sect. 3.2 could be used constructively. As these potentials have random character, we will use our ability to scan the full surface of a (broad) wire (Sect. 3.2.6) to find a location where an atom cloud can gradually be split by slightly changing the trap parameters, for instance the bias field direction.

5 Outlook: controlled single and multi-particle quantum states

This thesis work was focussed on developing the tools for microscopic matter wave control (chapter 2) and to explore the possibilities of approaching the surface of atom chips. Various new methods and trapping geometries have been developed and tested, in particular electrostatic fields are now an integral part of the manipulation repertoire [119]. At atom–surface distances of a few microns it has turned out that issues of imperfect fabrication (chapter 3) and fundamental thermal current noise in conductors (chapter 4) become important. If the structures used to form the manipulation potentials are smooth, disorder potentials can be kept low, even down to $\sim 1\mu$m. The current densities in surface mounted wires can be high enough to allow a reduction of the used metal to a level where thermal current noise limited lifetimes > 1s are possible at single micron surface distances. Our experiments have already shown that with currently used lithographically fabricated wires, wire imperfections are reduced to a tolerable degree. The influence of current noise has been studied theoretically and the predictions made are experimentally confirmed. So far, the experimental tests are not complete but indications of a positive influence of a thin metal layer versus bulk material have been observed. This supports the extrapolation to possible second long lifetimes down to a micron surface distance.
In conclusion, the work presented in this thesis shows that micro-manipulation of neutral atoms near surfaces of atom chips is feasible for surface distances down to $\sim 1\mu$m and experiment times of the order of seconds are possible. At shorter distances, a set of additional problems related to short range surface potentials has to be attacked. This regime remains to be investigated in future theoretical and experimental studies.
The short to mid term plans and current developments of the experiments have been mentioned throughout the text. The purpose of this final chapter is to outline the future directions the experimental efforts are heading to. It will not be possible to pursue all possible paths in parallel, and certain priority decisions will have to be made to some extent. Some experiments are or will be carried out in other setups. The chapter is divided into three sections: The first section is concerned with correlated many-body systems in various confining geometries, the second section then deals with single and few particle control, before the more technical third section comments on the development of microtraps for experiments pursuing these directions.

5.1 Entering the one-dimensional regime

The freedom in tailoring potentials is much larger on atom chips than in any conventional macroscopic trapping arrangement. This is highlighted in chapter 2 where a variety of tools and their experimental tests are discussed. In particular, it is possible to form elongated traps with a tunable aspect ratio between transverse and longitudinal trap frequencies ($\omega_\perp/\omega_\parallel$). This opens new possibilities for studying the transition between regular three-dimensional (3D) and (quasi) one-dimensional (1D) confinement. The intermediate and fully 1D regimes are interesting because the role and effective strength of the inter-particle interactions change or are changeable in a controlled way. In analogy to condensed matter systems, highly correlated systems beyond mean-field theory can be studied, especially in low-dimensional strongly confining systems (quantum wires).
The most striking example for a profoundly altered role of the interactions in low dimensions is probably the so called Tonks-Girardeau regime [186, 68] that was very recently observed experimentally [153]. Counter-intuitively, the condition for this limit of strong interactions in 1D confinement is reached for *low* densities. In this case, impenetrable bosons are described by a symmetric fermionic wave function, and thus behave like fermions in many respects. While this and other effects have started to be experimentally accessible in optical lattice systems, atom chips provide the unique possibility of addressing individual traps with largely tunable parameters. In addition, the presence of small and tunable (via the surface distance) random potential roughness will allow to study the influence of disorder, both in static and dynamic transport situations.
In the following, some recent observations we have made in quasi-1D confining potentials are presented. The results are not yet analyzed and much deeper experimental and theoretical understanding is desirable. This section is meant to show that indeed characteristic signatures of the dimensionality change from 3D to 1D are visible.

Elongated traps with high aspect ratios

There are various energy and length scales involved in the classification of confined gases into different categories of low-dimensionality. The different regimes have been thoroughly discussed in the literature [150, 157]. In this section only certain limits are mentioned and compared to current experimental parameters.
Effects of 1D confinement are observable in degenerate quantum gases as soon as the condition $\omega_\parallel \ll \omega_\perp$ is fulfilled. A consequence is that the gas below the critical temperature T_C is not phase coherent over its whole extension (quasi condensate). Fluctuating phases and resulting random interference patterns have been studied both theoretically [158] and experimentally [49]. Only below a lower T_ϕ, full coherence is established and no more interference fringes appear in the expanding condensate.

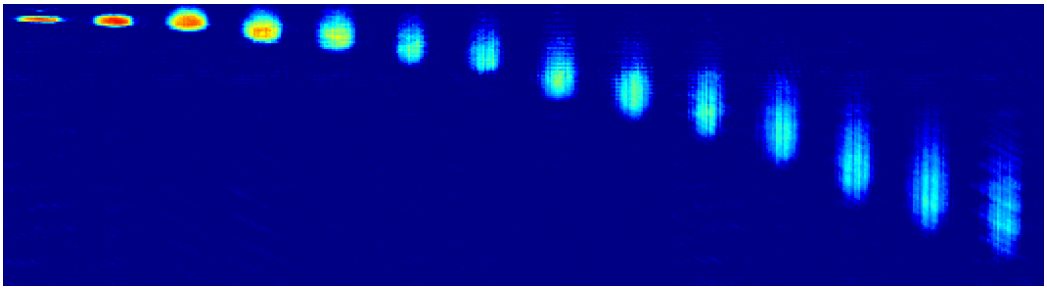

Figure 5.1: BEC expanded from a highly anisotropic trap (aspect ratio ~ 1000). The time sequence shows the expanding (quasi) condensate in situ (left) and after 2...14ms time-of-flight expansion (1ms steps, from left to right). Distinct dark lines rather than sinusoidal fringe patterns are visible after a certain expansion time.

Fig. 5.1 shows a time sequence of atoms released from a highly anisotropic trap (aspect ratio $\omega_\perp/\omega_\parallel \approx 1000$) formed near a 10μm wide wire. The dark fringes observed in our experiment can possibly be attributed to phase fluctuations like those observed in [49]. However, there seems to be a qualitative difference in the shape: Unlike the expectation for random fringes, the cloud exhibits a homogeneous profile over large regions interrupted only by distinct relatively sharp dark lines. One may speculate that this effect can be explained by the formation of solitons similar to those predicted for BECs in guided matter wave interferometers (Sect.4.4.3).
Beyond extreme trap aspect ratios, the next limit on the way to a true 1D regime is given by the transverse ground state energy $\hbar\omega_\perp$. When $\hbar\omega_\perp$ becomes larger than the chemical potential μ of the quantum gas, the Thomas-Fermi approximation is no longer valid in the transverse direction and the gas is in the transverse single particle ground state. In our elongated traps, especially very close to the surface (Sect. 3.2.5) this condition is well fulfilled. In fact, even the more severe limit of $k_B T_C \sim \hbar\omega_\perp$ is already reached. For confinement beyond this limit, transverse excitations do not play a role anymore, and the atomic motion in that direction is completely 'frozen' to the single particle zero point oscillations.

Electrostatic dimple trap

It has already been mentioned that the flexibility of atom chip based microchips in principle allows to study the crossover regimes both between 3D and lower dimensional geometries and between different 1D regimes. To illustrate such possibilities we have modified an elongated 1D confining potential by means of electrostatic fields.
The potential is realized by forming the 10μm-wire trap described in Sect. 3.1.3 far from the wire ($\sim 80\mu$m) but close to the chip surface ($\sim 10\mu$m). This is possible by rotating the bias field to point almost vertical to the chip surface.

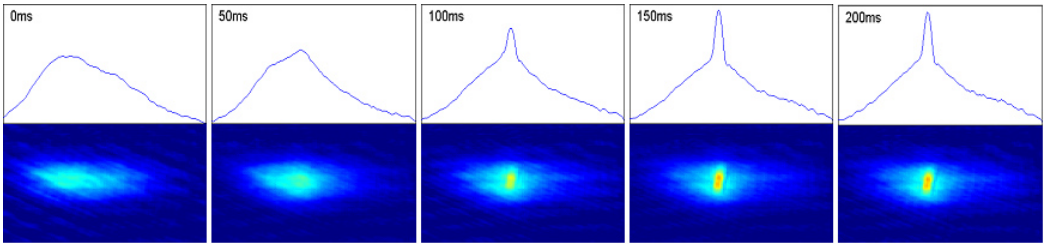

Figure 5.2: BEC formation by superimposing an electrostatically formed attractive potential ('dimple') onto a 1D magnetic trap. The time sequence shown starts with a thermal cloud in the original trap ($V_{\mathrm{dimple}} = 0$). After the dimple is switched on ($V_{\mathrm{dimple}} = 3.5V$), atoms start to accumulate near the electrode and a condensate is eventually formed, purely by means of the electrostatic potential. The signature of the BEC in the time-of-flight images (expansion time 10ms) is clearly visible as the enhanced density of thermal atoms in the dimple is much less pronounced and not detectable for thermal atoms. This was verified in a separate experiment.

The trap is placed directly above an auxiliary wire (part of the U-shaped wire D–E, see appendix C) running perpendicular to the magnetic trap wire. If this wire is charged electrostatically, a small 'dimple' potential on top of the elongated magnetic trapping potential forms near the trap center.
In a first demonstration experiment (Fig. 5.2), we have loaded the elongated trap and cooled a cloud of $\sim 10^5$ atoms to a temperature just above the critical temperature of 1D quantum degeneracy. The thermal character of the cloud is verified by a time-of-flight expansion. We then remove the cooling radio frequency and charge the auxiliary wire with a small voltage of 3.5V. At this stage, the dimple forms and atoms start to accumulate in this part of the potential. They form a condensate after $\sim$ 100ms when the density has reached a critical value. This relatively long time can heuristically be understood if the cloud's extension in the elongated trap ($\sim 700\mu$m) and the mean thermal velocity at 1μK ($\sim$ 1cm/s) are considered. The details of this trap configuration and related experiments will be discussed in [81].
The confinement inside the dimple is nearly isotropic while the trap outside has 1D geometry. This configuration should thus be well suited to study the 3D-1D crossover both statically and dynamically. It is likely that the 3D confinement in the dimple can be made strong enough to fulfill the condition $\hbar\omega \gg k_B T$ in all three dimensions so that all atoms of a condensate would be found in the 3D single particle ground state. The transition from this regime to an interaction dominated regime can then be investigated by varying the trap parameters (voltage, current, bias field) accordingly.

From a trap to a (quasi)guide

One of the key issues in mesoscopic electronics is the investigation and understanding of transport mechanisms [101]. The atom chip offers a wide range of

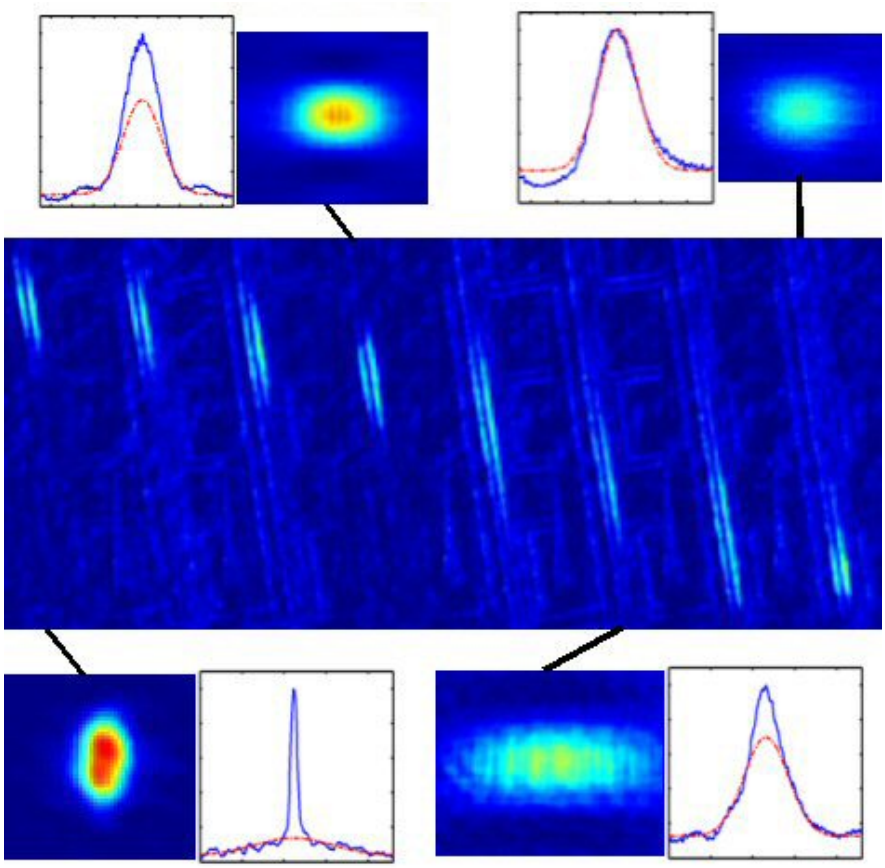

Figure 5.3: Time sequence (70ms) of a BEC released from a trap to a guide. The center row contains eight absorption images taken from a direction almost orthogonal to the chip surface. The expansion and movement of the cloud (and its reflection) along the guide (time step 10ms) is clearly visible. The additional images (top and bottom) are examples of time-of-flight (10ms) images of the expanding cloud (horizontal imaging). The 1D density profiles show that a pure condensate gradually turns into a thermal cloud during the transport (Gaussian fits to the thermal fraction plotted as red lines).

possibilities to study similar processes for bosonic and fermionic systems with varying and controllable interactions. Furthermore, external influences such as random disorder or periodic potentials of different strengths as well as controlled coupling to specifically designed perturbations can be explored. Experiments of this kind have the potential to sharpen the understanding of electronic systems where typically the various environmental influences are hardly separable. On the other hand, differences between electronic and atomic and between bosonic and fermionic systems will be highlighted.

Here, an example of a very first experiment we have conducted in this direction is given. Fig. 5.3 shows a time sequence of atoms released from a trap to a guide. The trap is formed by an L-shaped 10μm wide wire (connections X–

G, see appendix C) in combination with a U-shaped wire (connections A–B) providing an endcap (Sect. 3.1.3). In the source trap, almost all atoms are in the (3D) Bose-condensed phase. After the longitudinal barrier provided by the U-shaped wires is removed, the atoms start to move along the guide, pushed by a longitudinal field gradient provided by the lead of the L (connection G). During the transport, the thermal fraction of the cloud grows. More interestingly, the condensate is elongated and indications of abnormal density fluctuations similar to those observed previously after the release of condensates from traps with large aspect ratios (Fig. 5.1) are visible. After a transport time of $\sim$ 70ms, the atoms reach a barrier formed by a small bent in the guide where the movement is stopped, the cloud is longitudinally compressed, and all atoms become thermal.

This test experiment was performed at a surface distance of $\sim 70\mu$m where disorder potentials definitely have no influence. Repeating similar experiments closer to the surface in the presence of a tunable random potential roughness (by gradually adjusting the surface distance h) could provide a convenient environment for the investigation of a large variety of transport phenomena, for example Anderson localization effects [2].

5.2 Single atoms and qubits

The versatility and high resolution of atom chip potentials allows to specifically manipulate very small ensembles and even single atoms. This could eventually facilitate studies of the transition from systems that are best described microscopically to many-body systems that exhibit macroscopic behavior. There are two approaches: On the one hand, one can start with macroscopic quantum systems of the type discussed in the previous section and gradually gain more control over the various components involved (*top down* approach). On the other hand, an accurate control over individual particles can be the starting point from which the complexity of the system is gradually increased by adding more and more subsystems (*bottom up* approach).

The bottom up approach is the motivation for attempts at gaining full quantum control over individual atoms. This type of control is also referred to as the ability of performing quantum information processing (QIP). Building up complex networks of qubits encoded in atoms is nothing else than the bottom up approach discussed here. Typically, but not necessarily, quantum information is encoded in two-level systems (qubits) in analogy to the binary bits in classical quantum information processing. We have given a survey and assessment of the possibilities of QIP with neutral atoms on atom chips in [118]. An overview of the large field of QIP cannot be given here, nor can the atom chip approach be compared to other implementations in the framework of this thesis. This section is thus restricted to a few basic comments concerning our experimental efforts.

Single atom detection

Single atom manipulation requires the ability to address and detect single atoms. The simple absorption and fluorescence techniques we use to detect whole ensembles of atoms are not suitable since the interaction of a single photon with a single atom is not strong enough to be directly detected.
A way of circumventing this problem is to let the atom interact with multiple photons. Unlike in ion experiments [145], neutral atoms are removed from the trapping potentials after the scattering of only a few photons. Multiple photon interaction is still possible if cavities are used. In [100] it has been shown that fairly low quality cavities are sufficient to reach a reasonable signal to noise ratio in the altered photon transmission signal even for a single atom passing through the resonator.
Experiments with atoms being magnetically guided through a macroscopic cavity are currently being performed in a separate apparatus and first results have been obtained. To date, ensembles of the order of ~ 100 have been detected, a reduction of this number is expected soon [79]. Concurrently a microscopic fiber cavity and its mounting onto an atom chip are being developed. The status here is that all technical requirements are fulfilled so that an experimental test with atoms is possible in the near future [198].

Tunnelling

We are currently conceptualizing a tunnelling experiment as a first experiment of controlling a quantum state on the atom chip. In the lingo of QIP, the qubit is encoded in the localized states in a double well potential. An oscillation of the detection probability of an atom in one or the other well is a Rabi oscillation or single qubit rotation. By controlling the timing of the tunnel interaction, the atom can be put into any desired superposition state (single qubit gate). The tunnelling experiment is analogous to Josephson oscillations known from superconductor physics [12].
In a single particle picture, the tunnelling rate is given by the energy difference between the delocalized symmetric and antisymmetric eigenstates of the double well potential. Experimentally accessible (sufficiently slow) oscillation times and simultaneously maintaining a single well separation larger than the extension of the localized states are only possible if the structures forming the double well potentials are sufficiently small. Therefore we plan to use the smallest available structure on our chip (appendix C), namely a pair of 2μm wide wires with a center to center spacing of 4μm (Fig. 4.12).
For a (1D) BEC, the interactions have to be considered and the single atom picture is only valid as long as the on site interaction energy is small on a scale given by the tunnel coupling. The feasibility of a tunnelling experiment with BECs containing small atom numbers has been verified very recently in an optical

lattice experiment [148]. Our geometry should allow to work in the $k_B T \ll \hbar\omega_\perp$ regime where transverse excitations and spilling of thermal atoms between the wells can be excluded. Approximating the single atom case with a BEC is not only a valid substitution but also opens up the possibility to explore the transition between the interacting and non-interacting case in detail.

Qubit gates

There are numerous proposals for the implementation of neutral atom quantum gates (summaries can be found in [62, 171, 118]) on atom chips. The main two categories of possible qubits are *internal* state qubits where the two levels are atomic hyperfine states and *external* state qubits relying on motional states of the trapping potential.

Controlled internal qubit manipulation was recently achieved on an atom chip [187]. In this experiment, the two levels were chosen in such a way that their differential energy dependence on magnetic field fluctuations was minimized ('clock states'). This lead to extremely long coherence times of > 1s (Sect. 4.1.3). A single qubit gate based on motional states is likely to be realized soon in a tunnelling experiment of the type described above.

It has been shown that a universal quantum computer can be built using one and two qubit gates [146]. Building a two qubit gate is more difficult than the single qubit operation. The reason is that a two qubit gate requires an operation on one atom conditioned on the state of the other. This in turn is only possible if the two atoms interact in one way or another. The existing proposals include photon mediated interaction [164], dipole-dipole interaction of atoms in highly excited Rydberg states [26, 27] and controlled atom-atom collisions [102, 33].

A possibility of implementing internal state conditional controlled collisions is provided by electrostatic fields as outlined in Sect. 2.5.4. We are currently developing concepts for a simulation of a collisional two qubit gate along the lines of the proposal [184].

5.3 Next generation atom chips

The results of this thesis and related work give rise to a confidence that the micron vicinity of structured surfaces is accessible to new experiments in the directions outlined above. Consequently, we have started to develop a new generation of atom chips based on the newly gained understanding of surface effects. In the following, the design principles are outlined and examples of fabrication tests are shown.

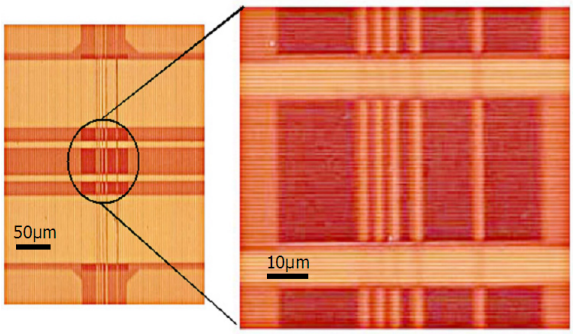

Figure 5.4: Hybrid fabrication. The images are taken with an optical phase contrast microscope. The fine wires are only 30nm high and 1μm wide. The broad wires cross this layer, but are separated by a 60nm thin SiN isolation layer. In the top layer the wires have a cross section of $10\times2.7\mu\text{m}^2$ and $100 \times 2.7\mu\text{m}^2$.

Hybrid structures for loading and manipulation

Our new chips will be based on hybrid designs combining both tall and wide wire structures to form deep large volume traps (see Sect. 2.4.2 for relevant scaling laws) and thin and flat microwires for the detailed manipulation on the quantum level (Fig. 5.4). The idea is to be able to keep large numbers of atoms trapped in a reservoir trap with moderate confinement comparably far ($> 50\mu$m) from large wires creating the potential. The confinement can still be strong enough to guaranty the elastic collision rates necessary for a fast and efficient BEC production. The loading of the reservoir trap will also be improved by a redesigned copper structure underneath the chip. This structure is conceived to feature a more efficient heat sink by use of high tech ceramics materials and a copper cooling block in direct contact with the substrate. The central bar of the Z-wire forming the initial magnetic trap will be broadened to enhance the trapping volume and to improve the mode matching (Sect. 3.1.2). Additional independent transverse wire bars at several locations will allow a flexible tuning of longitudinal confinement and 'pushing' gradients. An intermediate prototype of the new development has already been fabricated and will be described in detail in [81].

Thin wires and small trapping geometries

Single micron wide and $\sim$ 100nm tall current carrying wires and chargeable electrodes will be used to form the highly structured potentials desired for the actual mesoscopic and single quantum experiments. These potentials will be easily loaded with ultracold atoms and BECs from the reservoir trap even if they are shallow. This allows to use very small wires carrying small currents so that both thermal current noise induced loss, heating and decoherence rates and disorder potentials scaling with the wire current are suppressed. Yet, the scaling laws outlined in Sects. 2.4.2 and 4.2 allow strong confinement and localization of individual trapping sites at small inter-trap distances.
Fig. 5.5 shows a detail of a recently fabricated grid of 1μm and 3μm wide and 30nm tall wires on a silicon wafer. Such structures can also be crossed with and without an intermediate isolation layer. As such multi-layer technology needs to

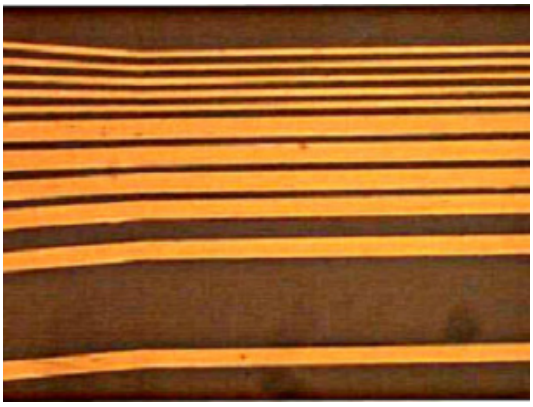

Figure 5.5: Optical phase constrast image of a grid of wires with 1μm and 3μm width and varied inter-wire spacing. For adhesion a 30Å thick Ti layer was used. The wires are widened at a distance from the planned experimental region in order to keep total resistances reasonably low.

be developed for the implementation of the hybrid designs mentioned above, the increase in complexity of the fabrication process is small if also several crossed thin layers are used.
Other current developments of the atom chip fabrication technology include the integration of fiber cavities for optical detection and manipulation of few and single atoms. This will be discussed elsewhere [198].

A ^{7}Li apparatus

The experiments exploring the tools that can be implemented with atom chips (chapter 2) have been performed with cold ^{7}Li atoms. The basic apparatus was the one originally described in [45] that was used for first experiments of guiding atoms near free standing straight, split [35], and bent [78] wires. Later we performed our first atom chip experiments with this setup [116, 61] before we moved it from Innsbruck to Heidelberg. Throughout the last three years of operation, we have applied several modifications in order to improve and facilitate the various procedures and to adapt them to the respective experiments. The whole apparatus in its final state with an emphasis on the changes made have recently been described in a PhD thesis [28]. Here, only a few comments on the main experimental components are given, highlighting the differences to Rb setups.

The laser system is not based on simple (and comparably cheap) diode lasers but on a solid state laser pumped dye laser that emits 0.5–1W of red light at the Li-D line at $\lambda = 671$nm. Both finestructure and hyperfinestructure splitting of the light ^{7}Li are much smaller than for the heavier ^{87}Rb and necessitates much larger intensities on the repumping transition. This light is provided by an electro-optic modulator (EOM) driven at a frequency of 812MHz. The relative intensity of the repumper side band relative to the carrier (cooling) frequency was tuned to up to 30% in the experiments.

Chemical properties differ between Li and Rb (for example stronger tendency for adsorption of Li) and make spectroscopy and the source of atoms in the experimental vacuum chamber technically more challenging for Li [45, 35, 28]. By replacing the original simple oven by a more complex one, we could improve the vacuum background pressure by more than an order of magnitude to below 10^{-10}mbar. This oven features a motor driven switchable atom beam stop, a differential pumping stage and a vacuum valve that facilitates atom chip replacements [195].

The atom chip holder and the vacuum chamber are similar to those of the ^{87}Rb second generation experiment (appendix B) where a few improvements have been made. The quadrupole field for the Li-MOT was not yet exclusively produced by a U-wire configuration, so that a pair of bulky water cooled coils driven at ~ 2000 Ampere windings (mass of ~ 5kg each) were needed.

The experimental control system was based on LabView programmed National Instruments analog and digital control cards integrated in a standard PC. The atoms were detected by their fluorescence imaged with a high quantum efficiency

(85%) 16bit 1340 $\times$ 400pixel ($20 \times 20\mu m^2$) spectroscopy CCD camera.

B ^{87}Rb apparatus

In the framework of this thesis, a new cold ^{87}Rb atom BEC apparatus was designed and constructed. All experiments presented in chapters 3 and 4 were performed using this setup. The details of its various components have been described in a number of diploma theses [15, 67, 86, 25], and the basic experimental procedures will be discussed in [98, 81]. Here, only the main characteristics are sketched. In general, the goal was to build a compact setup and to maintain a level of complexity that is as low as possible in order to facilitate a stable operation of the apparatus.

B.1 Laser system

Cold atom experiments rely on laser cooling techniques [140] that require deterministic driving of hyperfine transitions and hence narrow band frequency light sources stabilized to atomic lines with an accuracy much higher than the natural transition line widths [116].
In our setup, we use a commercial diode laser system consisting of a grating stabilized master laser and a tapered amplifier chip[1] that provides up to 500mW of laser light at the Rb D2-line ($F = 2 \rightarrow F = 3$) at $\lambda = 780$nm. The master laser is frequency stabilized by a frequency modulation (FM) lock technique described in [67]. As a second frequency source, we use a self-built master [86] – slave [81] diode laser combination with a peak power output of $\sim$ 100mW. This system is locked onto the repumping transition ($F = 1 \rightarrow 2$) by a standard lock in technique [86]. The basic laser system and the spectroscopy setups used to define the appropriate frequencies are housed in a mechanically (vibrations), electrically, and optically well isolated wooden box.
Outside this box in another optically isolated region on the same laser table, a frequency preparation stage is mounted. A number of acousto-optical modulators (AOM) are driven at various radio frequencies to provide, switch and tune the optical frequencies used in the experiments. These frequencies are adjusted to near the $F = 2 \rightarrow 3$ transition (variable red detuning for cooling), the $F = 2 \rightarrow 2$ transition (optical pumping), and the $F = 2 \rightarrow 3$ transition (variable tuning around resonance for imaging). A schematic drawing of the optical setup and the various beam paths is shown in Fig. B.1 that was adapted from [25], where more technical details may be found.

[1] Toptica, TA100 system.

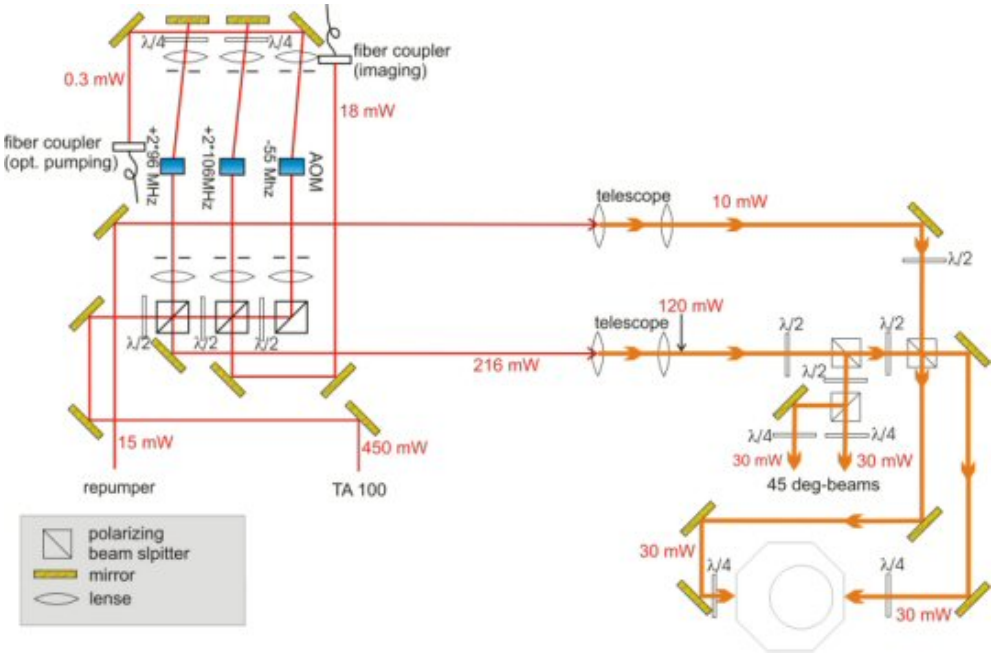

Figure B.1: Schematic overview of the optical beam path in the experiment. The necessary frequency shifts are introduced by AOMs in double pass configuration for tunable shifts (cooling, imaging) or single pass configuration for a fixed shift (optical pumping). The imaging and optical pumping light is transmitted to the vacuum chamber through optical fibers, the cooling and repumping light is widened through telescopes, split up and then (mirror) steered to the chamber directly.

B.2 Vacuum system

To date, experiments with dilute gas BECs can only be performed in ultra-high vaccum (UHV) environments. This is due to the fact that collisions of cold atoms with hot background gas particles have to be avoided to a certain extent, so that loss and heating processes do not dominate during the experimental period (Sect. 4.1.1).

Our UHV chamber (Fig. B.2, details in [86]) was constructed to allow good optical access to the experimental region directly above the surface of the chip. This was realized by including optical quality quartz windows in an octogonally shaped stainless steel body. The distance from the outer surfaces to the experimental region is 4cm and 10cm for the directions perpendicular and parallel to the chip surface, respectively. As a source for rubidium atoms we use three dispensers that are connected in parallel. A high pumping speed in combination with a pulsed operation mode of the dispensers facilitates sufficient loading rates of the MOT of typically 3×10^7 atoms/s while the rubidium background vapor is quickly reduced in the purely magnetic trapping phase of the experiment. The vacuum system reaches a base pressure of below 7×10^{-12}mbar and is pumped by a combination

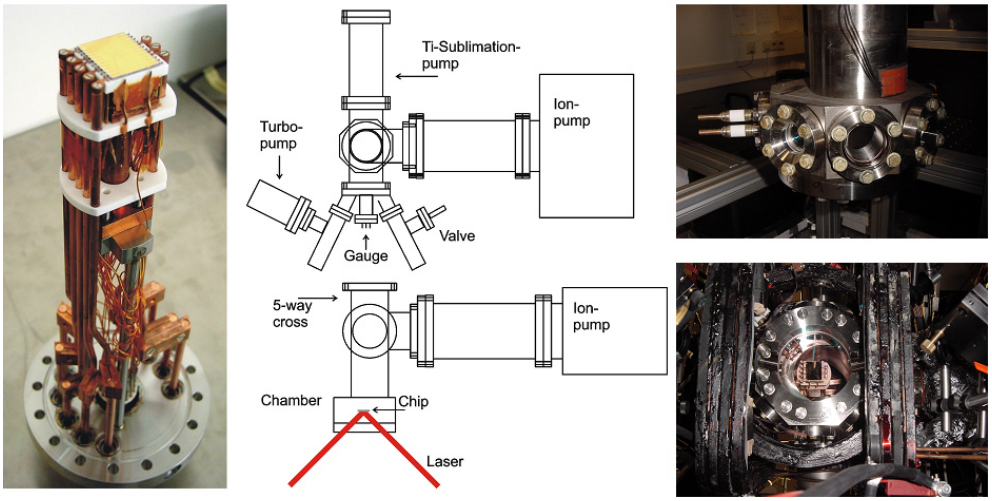

Figure B.2: (*left*) Atom chip assembly: The U-wire structure for the MOT (Sect. 3.1.1) and an additional structure containing Z-shaped wires in several sizes (Sect. 3.1.2) are connected to high-current vacuum feedthroughs. The atom chip is mounted directly on top of these wire structures. (*center*) Schematic drawing of the vacuum chamber. The actual 'science' chamber consists only of a small octogonal steel body (small rectangle at the bottom of the picture) containing the atom chip. The rest of the chamber serves mainly vacuum diagnostics and allows fast and efficient pumping. (*right*) Photograph of a clear view of the chamber before (top, side view) and after (bottom, bottom view) optics and coils were mounted.

of a Ti sublimation pump and a 300l/s ion pump.

B.3 Atom chip assembly

The central part of the experimental setup is the atom chip and the surrounding assembly. With the exception of small homogeneous external bias fields, all trapping fields in our experiments are provided by the chip itself or by the copper structures mounted directly underneath. This necessitates independent electrical access to as many as 33 different contact points inside the vacuum chamber; eight of these connections need high current tolerances of 50–100A (the others only up to $\sim$ 2A).

The resulting complex construction of various UHV-compatible ceramics and metal holders, copper connectors, special alloy pins, isolating Kapton foils etc. consists of several hundred custom made pieces and is described in detail in [15]. A photograph is shown in Fig. B.2.

B.4 Experimental control

The different steps of the experimental procedure that is cyclicly repeated at a rate of 90 experiments/hour (40s cycle time) require a sequence of accurate controlling signals with precise timing. For this purpose, we use a modular stand-alone control system based on its own fast processor[2]. The system is driven by a custom-programmed MatLab environment. To drive all current sources, light manipulating elements and diagnostic components, a total of 16 analog (16bit) and 32 digital output channels are/can be independently operated. In addition analog input signals can be read in from eight different channels. The system is modular so that additional processor modules and input/output cards can be integrated if necessary. The channel update frequency can be flexibly adapted to the experimental demand and complexity; at this time, all output channels are updated at a rate of 80kHz, the input channels are scanned at 100Hz, as they are used as monitor of slow experimental drifts.
The system and its programming, characteristics and performance is described in all details in [25].

B.5 Atom detection

Finally, the most important measurement device in all our experiments is the imaging system. Almost all information about the behavior of the cold atoms is derived from sequences of charged coupled devices (CCD) that allow to reconstruct atomic distributions.
The interaction of atoms with light of a frequency around a transition line can be exploited in various ways to gain information on the density profile of an atomic cloud. There are two main categories of imaging techniques that can be distinguished by the importance of the real or imaginary part of the complex refraction index $n(\omega)$ of the atoms. If the light is relatively far detuned from the atomic transition, the real part dominates and the atom–light interaction is *dispersive* so that little or no energy is transferred. This allows non-destructive atom detection by measuring the acquired phase shift of the light (phase contrast imaging).
The other category is comprised of techniques relying on the *dissipative* near resonant atom–light interaction where the imaginary part of $n(\omega)$ is dominant. This means that the atoms absorb photons which can be detected directly by comparing a light beam profile passing through the ensemble with the profile of an equal reference beam imaged when the atoms are absent (*absorption imaging*). For our ^{87}Rb experiments, we have mainly used absorption imaging, unless stated otherwise. An alternative (used in the ^{7}Li experiments) is *fluorescence imaging* where the re-emitted photons after the absorption are collected in a fractional

[2] ADwin-Pro system

solid angle. The different properties of the various imaging techniques and the formulae for the derivation of atom densities from the detected light signals are discussed throughout the literature, for example in [59]. We extract not only information on density profiles and absolute atom numbers from CCD-images, but also temperatures: When all trapping potentials are turned off at a specific moment, the atomic momentum distribution is mapped to a spatial density distribution after a time-of-flight (TOF) period of ballistic expansion. For accurate temperature measurements we take many images after varying TOF duration. For most purposes, though, it suffices to take a single image after an appropriate TOF of typically 5ms for hotter atoms and 10–15ms for cold thermal or BEC clouds.

In our ^{87}Rb setup we have installed absorbtion imaging optics along two axes: The first is oriented parallel to the chip surface and perpendicular to the main guiding axis of the chip (top–bottom in Fig. C.1). This *horizontal imaging* allows to observe the longitudinal density profile of atoms trapped in the elongated chip traps and of atoms expanding along the various guides. In addition, the distance from the chip surface can be directly measured to a certain extent (see details in Sect. 3.2.3).

The second imaging axis is close to the chip surface normal (the tilt is ~ 5 deg). This *vertical imaging* relies on the reflection off the chip's gold surface and is hence sensitive to residual surface roughness and light scattering, diffraction and missing reflected light from the gaps defining the wires. The resulting image quality is good if the atoms are localized far from wire edges, for example above the center of a broad wire and decreases as wire edges are approached. We are mainly using the vertical imaging to determine the position of an atom cloud relative to the chip layout, rather than for quantitative analysis. For that matter, the horizontal imaging turned out be better suited (and sufficient).

The imaging system will be discussed more thoroughly in [196]; some technical information is given here: The horizontal imaging is set up in a way that allows to switch between magnifying ($\sim$ 1.7-fold, currently being changed to $\sim$ 3.5fold) and demagnifying ($\sim$ 3fold) imaging. The switching is done by means of a removable mirror in the imaging path that steers the beam through the demagnifying optics to a simple half inch 8-bit CCD (Pulnix TM6AS) with low quantum efficiency for overview pictures. When the mirror is removed the magnified image (optical resolution $\sim 3\mu$m) is detected with a large CCD (1024×1024 pixels of $13 \times 13\mu\text{m}^2$ size). The chip is a back-illuminated CCD (Roper Scientific MicroMAX 1024BFT) with a quantum efficiency of 70% at 780nm and can be driven in frame transfer mode so that the absorption frame and the reference frame can be acquired with a small time delay, limited only by the time it takes for the atoms to leave the imaging region. A 16-bit pixel depth guarantees a large dynamic range.

The vertical imaging camera is a spectroscopy camera with 1340×400 $20 \times 20\mu\text{m}^2$ 16-bit deep pixels with a quantum efficiency of 85% (Roper Scientific NTE/CCD-

1340/400). Currently, the image is magnified by a factor of ~ 5, so that the pixel limited resolution is $\sim 4\mu$m, optically 3μm are possible with the lens used.

C Chip design

The design of the atom chip used for all experiments presented in chapters 3 and 4 is shown in Fig. C.1. The letters are used for labelling the various wires and correspond to the labels used on the connecting interface in the laboratory.
Two lithography masks have been machined according to this design, one with exactly the structure depicted in Fig. C.1, and one with 2μm narrower wires. This made it possible to fabricate the chip with two connected gold layers with an alignment tolerance of $\pm 1\mu$m. The reason of the layer duplication was twofold: Firstly, a greater total thickness of the gold film could be reached so that the maximally sustained currents are large. Secondly (more importantly), this technique allows to combine structures of very different widths on a single chip without fabrication difficulties arising from extreme ('tower'-like) aspect ratios even if the general layer thickness is large. The advantage of the double layer is that only the wide structures are duplicated while narrow wires are only part of the thinner bottom layer (1.3μm versus 1.8μm for the top layer). In the following, the structures and their purpose are briefly discussed and references to the relevant sections of this thesis are given for some cases. Details of the relevant parts of the design with higher image resolution are illustrated throughout the text in the respective sections.
The main source traps serving as a cold atom reservoir are based on the 100μm-Z (T–H) and the 50μm-Z (U–H). These large volume Ioffe-type traps (Sect. 2.4.8) can be directly loaded from the Cu-Z trap (Sect. 3.1.3). Many of the experiments are directly performed in these traps or other potentials are loaded from here.
Four (mostly parallel) 10μm wide wires in the center of the chip (connections X,Y,Z and G) form a four wire guide that is split and recombined in the guided matter wave interferometer discussed in Sect. 4.4 (bottom of Fig. C.1). A longitudinal confinement turning a guide formed by these wires or a subset thereof into a trap can be provided by (a combination of) the 20μm wide U-shaped wires on the right hand side of the chip (connections A, B, C, D, E, F). One of the wires (E–F) is shaped in a periodically meandering way so that a periodic longitudinal extra potential can be imprinted onto a guiding potential.
The 10μm-Z (S–J) has a substructure in its center that is again Z-shaped. The central part of this inner Z consists of two 2μm wires (only in the 1.3μm tall bottom layer; all other wires have the double layer height of $(1.3 + 1.8)\mu$m$=$ 3.1μm) with a center to center spacing of 4μm (not resolved in Fig. C.1). This structure is meant to form a small scale time-dependent interferometer (Sect. 4.4.4).

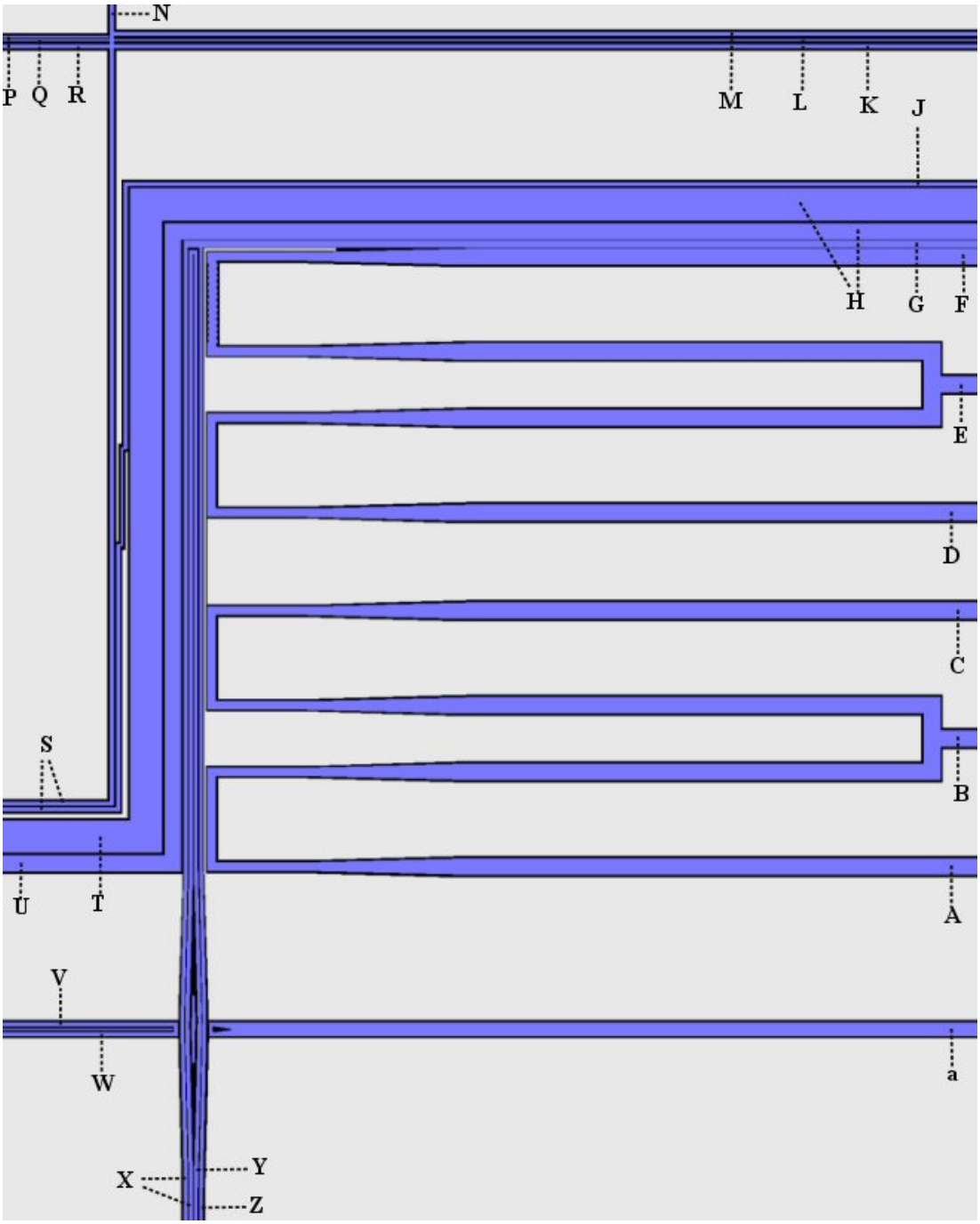

Figure C.1: Design of the atom chip used for the experiments with ^{87}Rb. Only the central region ($3.1 \times 3.9\text{mm}^2$) is shown, all wires are broadened towards the 2.2mm wide connecting pads (outside the field of view). The gold wires are colored blue, the gray areas correspond to grounded parts of the gold mirror and the black lines indicate the gaps from which the gold has been removed in order to define (electrically isolate) the wires.

Finally, the interconnected system of 10μm wires in the upper left part of the image (connections K, M, N, P, R, S) represents a Z-trap double well interferometer (Sect. 4.4.4) and wires intended to be used for its loading. The barrier in the double well can be introduced and tuned with the 5μm wire Q–L.
Of course, the arrangement of wires on this chip can not only be used for the intended experiments outlined above. Rather, a multitude of potential configurations on very different spatial scales can be achieved, and hence many interesting new experiments become feasible. The microscopic magnetic scanning of a conductor surface (wire T–H) with a BEC (Sect. 3.2.6) is just one example of such an originally unplanned experiment.

D List of publications

This PhD thesis and the preceding diploma thesis have led to the following publications:

- R. Folman, P. Krüger, D. Cassettari, B. Hessmo, T. Maier, and J. Schmiedmayer. Controlling cold atoms using nanofabricated surfaces: Atom chips. *Phys. Rev. Lett.*, 84:4749, 2000.

- M. Bartenstein, D. Cassettari, T. Calarco, A. Chenet, R. Folman, K. Brugger, A. Haase, E. Hartungen, B. Hessmo, A. Kasper, P. Krüger, T. Maier, F. Payr, S. Schneider, J. Schmiedmayer. Atoms and Wires: Towards Atom Chips. *IEEE J. Quant. Elec.*, 36:1364, 2000.

- D. Cassettari, A. Chenet, R. Folman, A. Haase, B. Hessmo, P Krüger, T. Maier, S. Schneider, T. Calarco, and J. Schmiedmayer. Micromanipulation of neutral atoms with nanofabricated structures. *Appl. Phys. B*, 70:721, 2000.

- K. Brugger, T. Calarco, D. Cassettari, R. Folman, A. Haase, B. Hessmo, P. Krüger, T. Maier, and J. Schmiedmayer. Nanofabricated atom optics: Atom chips. *J. Mod. Opt.*, 47:2789, 2000.

- P. Krüger and J. Schmiedmayer. Atome im Strahlteiler. *Physik in unserer Zeit*, 32:60, 2001.

- R. Folman, P. Krüger, J. Schmiedmayer, J. Denschlag, and C. Henkel. Microscopic atom optics: from wires to an atom chip. *Adv. At. Mol. Opt. Phys.*, 48:263, 2002.

- P. Krüger, A. Haase, R. Folman, and J. Schmiedmayer. Quantum information processing with neutral atoms on atom chips. In T. Beth and G. Leuchs, editors, *Quantum Information Processing*, page 257, Berlin, 2002. Wiley.

- C. Henkel, P. Krüger, R. Folman, and J. Schmiedmayer. Fundamental limits for coherent manipulation on atom chips. *Appl. Phys. B*, 76:173, 2003.

- P. Krüger, X. Luo, M. W. Klein, K. Brugger, A. Haase, S. Wildermuth, S. Groth, I. Bar-Joseph, R. Folman, and J. Schmiedmayer. Trapping and manipulating neutral atoms with electrostatic fields. *Phys. Rev. Lett.*, 91:233201, 2003.

- S. Wildermuth, P. Krüger, C. Becker, M. Brajdic, S. Haupt, A. Kasper, R. Folman, and J. Schmiedmayer. Optimized mageto-optical trap for experiments with ultracold atoms near surfaces. *Phys. Rev. A*, 69:030901(R), 2004.

- X. Luo, P. Krüger K. Brugger, S. Wildermuth, H. Gimpel, M. Klein, S. Groth, R. Folman, I. Bar-Joseph, and J. Schmiedmayer. An atom fiber for guiding cold neutral atoms. 2004. quant-ph/0311174, submitted to *Opt. Lett.*

- S. Groth, P. Krüger, S. Wildermuth, R. Folman, T. Fernholz, D. Mahalu, I. Bar-Joseph, and J. Schmiedmayer. Atom chips: Fabrication and thermal properties. 2004. cond-mat/0404141, submitted to *Appl. Phys. Lett.*

- K. Brugger, P. Krüger X. Luo, S. Wildermuth, H. Gimpel, M. Klein, S. Groth, R. Folman, I. Bar-Joseph, and J. Schmiedmayer. Two wire guides and traps with vertical bias field on atom chips. 2004. To be submitted to *Phys. Rev. A*.

In addition, there have been a number of contributions to conference proceedings. Publications on reduced disorder potentials near lithographically fabricated wires [117] and on the use of BECs as magnetic surface microscopes are currently being prepared. A new review article on our recent work will be submitted soon [121].

E Acknowledgement

This work would certainly not have been possible without the tremendous support of friends and colleagues. I would like to sincerely thank everyone who has contributed to the various aspects of my thesis. I thank

- **ℵ:** Sönke Groth for his infinite patience in building atom chips; Israel Bar-Joseph for building bridges to semiconductor physics and his great hospitality during my stay at the Weizmann Institute.
- **A:** ANNA.
- **B:** BJÖRN Hessmo for his careful – last minute – reading of the manuscript and the glorious coil winding experience.
- **C:** COCKPIT designer Ron Folman for teaching me a lot, also beyond the realm of physics in the skies over Mannheim and elsewhere.
- **D:** The eight DIPLOMA students I had the pleasure of working together with for their enormous efforts. Stephan Wildermuth, Matthias Klein, Hartmut Gimpel, Christiane Becker, Sebastian Haupt, Mihael Brajdic, Elmar Haller, and Sebastian Hofferberth all helped in designing, building and running the experiments.
- **E:** The Innsbruck (one man) ELECTRONICS team Andreas Mitterer, and the Heidelberg team.
- **F:** Various institutions for FUNDING this work: the Studienstiftung des deutschen Volkes and the Deutsche Forschungsgemeinschaft for personal funding, the Max-Planck Gesellschaft, the Quiprocone network, and the European Union for additional support.
- **G:** The Café GLOCKSEE, Thomas Fernholz, his great Halloween birthday parties, and his equally valuable physics insights.
- **H:** HEIDELBERG and its top spot, the roof of the Physikalisches Institut.
- **I:** The old INNSBRUCK crew that made me keep my diploma time memories fond, thanks to Donatella Cassettari, Markus Bartenstein, Thorsten Schumm and all the others.

- $\langle \hat{\mathbf{I}}_{\mathrm{Tiger}} \rangle$**:** IGOR Lesanovsky and Berth Hoffer for the rules of the game.

- **J:** JÖRG Schmiedmayer for supervising my diploma and now this thesis. I have learned a lot from him about dealing with cold atoms and cold snow during the last five years.

- **K:** The KRÜGERS in Berlin, Buenos Aires and Nürnberg.

- **L:** Tyrol's LASER LEGEND Alex Kasper (Kanpai!).

- **M:** The MIRACULOUS MRS. MUS in spite of the miserable chess and tabletop soccer defeats.

- **N:** The NORDKETTE.

- **Ö:** Well, and the rest of ÖSTERREICH (the Buzzhütte's Eiterbeule, the legendary SFB feasts, and the daily caraway bread).

- **P:** The POSTDOCS. Most notable Mauritz Andersson for letting me share his great optics knowledge and the memorable quiz nights at the pub. I have learned a lot during discussions with Louw Feenstra and Ji Il Kim.

- **Q:** QUANTUM expert Peter Schmelcher for advice and discussion.

- **R:** The REST of the inmates of the "Schwesternheim Innrain" and the Vienna Lounge.

- **S:** The SPIRAL taming Karolina Brugger. Her ability to herd atoms, sheep, and her little Anna is truly impressive.

- **T:** Carsten Henkel and Tommaso Calarco for invaluable THEORY support.

- **U:** The ULTIMATE frisbee team, the Heidees.

- **V:** Dr. VACUUM Sneider and his affinity to flying objects. Don't forget to pay your mountaineering insurance!

- **W:** The WORKSHOP team of the Physikalisches Institut.

- **X:** XUELI Luo for teaching the lithium atoms how to speak Chinese after they had gone through Italian, Hebrew, Swedish, and Tyrolean courses.

- **XXX:** Sebastian, Elmar, Stephan, Anna, and Albrecht for the XXXtra hours they invested in helping to compile this manuspcript.

- **Y:** The Y-beam splitters for their reliable willingness to split cold atom clouds.

- **Z:** The master of the Z-trap Albrecht Haase for introducing me to his mother and for keeping Berlin alive in the South. Which side are you on, boy?

Bibliography

[1] M. H. Anderson, J. R. Ensher, M. R. Matthews, C. E. Wieman, and E. A. Cornell. Observation of Bose-Einstein condensation in a dilute atomic vapor. *Science*, 269:198, 1995.

[2] P. W. Anderson. Absence of diffusion in certain random lattices. *Phys. Rev.*, 109:1492, 1958.

[3] E. Andersson, T. Calarco, R. Folman, M. Andersson, B. Hessmo, and J. Schmiedmayer. Multi mode interferometer for guided matter waves. *Phys. Rev. Lett.*, 88:100401, 2002.

[4] E. Andersson, M. T. Fontenelle, and S. Stenholm. Quantum statistics of atoms in microstructures. *Phys. Rev. A*, 59:3841, 1999.

[5] L. M. Andersson. Unpublished, 2004.

[6] L. M. Andersson et al. 2004. In preparation.

[7] M. Arndt, O. Nairz, J. Voss-Andreae, C. Keller, G. Van der Zouw, and A. Zeilinger. Wave-particle duality of C_{60} molecules. *Nature*, 401:680, 1999.

[8] V. S. Bagnato, G. P. Lafyatis, A. G. Martin, E. L. Raab, R. N. Ahmad-Bitar, and D. E. Pritchard. Continuous stopping and trapping of neutral atoms. *Phys. Rev. Lett.*, 58:2194, 1987.

[9] S. Bali, K. M. O'Hara, M. E. Gehm, S. R. Granade, and J. E. Thomas. Quantum-diffractive background gas collisions in atom-trap heating and loss. *Phys. Rev. A*, 60:R29, 1999.

[10] J. Bardeen, L. N. Cooper, and J. R. Schrieffer. Theory of superconductivity. *Phys. Rev.*, 108:1175, 1957.

[11] A. H. Barnett, S. P. Smith, M. Olshanii, K. S. Johnson, A. W. Adams, and M. Prentiss. Substrate-based atom waveguide using guided two-color evanescent light fields. *Phys. Rev. A*, 61:023608, 2000.

[12] A. Barone and G. Paterno. *Physics and Applications of the Josephson Effect*. Wiley, New York, 1982.

[13] M. D. Barret, J. A. Sauer, and M. S. Chapman. All-optical formation of an atomic Bose-Einstein condensate. *Phys. Rev. Lett.*, 87:010404, 2001.

[14] M. Bartenstein, A. Altmeyer, S. Riedl, S. Jochim, C. Chin, J. Hecker Denschlag, and R. Grimm. Crossover from a molecular Bose-Einstein condensate to a degenerate Fermi gas. *Phys. Rev. Lett.*, 92:120401, 2004.

[15] C. Becker. *Eine neuartige magneto-optische Falle für Atomchip-Experimente*. Diploma thesis, Universität Heidelberg, 2002.

[16] J. S. Bell. On the Einstein-Podolsky-Rosen paradox. *Physics*, 1:195, 1964.

[17] J. S. Bell. On the problem of hidden variables in quantum mechanics. *Rev. Mod. Phys.*, 38:447, 1966.

[18] C. H. Bennett, G. Brassard, C. Crepeau, R. Jozsa, A. Peres, and W. Wootters. Teleporting an unknown quantum state via dual classical and Einstein-Podolsky-Rosen channels. *Phys. Rev. Lett.*, 70:1895, 1993.

[19] T. H. Bergeman, P. McNicholl, J. Kycia, H. Metcalf, and N. Balazs. Quantized motion of atoms in a quadrupole magnetostatic trap. *J. Opt. Soc. B*, 6:2249, 1989.

[20] P. Berman, editor. *Atom Interferometry*, volume 37 of *Adv. At. Mol. Opt. Phys.* Academic Press, New York, 1997.

[21] G. Birkl, F. B. J. Buchkremer, R. Dumke, and W. Ertmer. Atom optics with microfabricated optical elements. *Opt. Commun.*, 191:67, 2001.

[22] S. Bose. Plancks Gesetz und Lichtquantenhypothese. *Z. Phys.*, 26:178, 1924.

[23] D. Bouwmeester, J.-W. Pan, K. Mattle, M. Eibl, H. Weinfurter, and A. Zeilinger. Experimental quantum teleportation. *Nature*, 390:575, 1997.

[24] C. C. Bradley, C. A. Sackett, J. J. Tollett, and R. G. Hulet. Evidence of Bose-Einstein condensation in an atomic gas with attractive interactions. *Phys. Rev. Lett.*, 75:1687, 1995.

[25] M. Brajdic. *Entwicklung einer Computersteuerung und ihre Anwendung in einem Experiment zur vereinfachten Bose-Einstein Kondensation in einer Oberflächenfalle*. Diploma thesis, Universität Heidelberg, 2003.

[26] G. K. Brennen, C. Caves, P. Jessen, and I. Deutsch. Quantum logic gates in optical lattices. *Phys. Rev. Lett.*, 82:1060, 1999.

[27] G. K. Brennen, I. H. Deutsch, and P. S. Jessen. Entangling dipole-dipole interactions for quantum logic with neutral atoms. *Phys. Rev. A*, 61:062309, 2000.

[28] K. Brugger. *Experimente mit mikroskopischen atomoptischen Elementen.* PhD thesis, Universität Heidelberg, 2004.

[29] K. Brugger, T. Calarco, D. Cassettari, R. Folman, A. Haase, B. Hessmo, P. Krüger, T. Maier, and J. Schmiedmayer. Nanofabricated atom optics: Atom chips. *J. Mod. Opt.*, 47:2789, 2000.

[30] K. Brugger, P. Krüger, X. Luo, S. Wildermuth, H. Gimpel, M. Klein, S. Groth, R. Folman, I. Bar-Joseph, and J. Schmiedmayer. Two wire guides and traps with vertical bias field on atom chips. 2004. To be submitted to *Phys. Rev. A*.

[31] E. Buks, R. Schuster, M. Heilblum, D. Mahalu, and V. Umansky. Dephasing in electron interference by 'which-path' detector. *Nature*, 391:871, 1998.

[32] J. P. Burke, J. L. Bohn, B. D. Esry, and C. H. Greene. Impact of the ^{87}Rb singlet scattering length on suppressing inelastic collisions. *Phys. Rev. A*, 55:R2511, 1997.

[33] T. Calarco, H.-J. Briegel, D. Jaksch, J. I. Cirac, and P. Zoller. Quantum computing with trapped particles in microscopic potentials. *Fortschritte der Physik*, 48:945, 2000.

[34] H. B. G. Casimir and D. Polder. The influence of retardation on the London-van der Waals forces. *Phys. Rev.*, 73:360, 1948.

[35] D. Cassettari. *Cold Atoms in Microscopic Traps: From Wires to Chips.* PhD thesis, Universität Innsbruck, 2000.

[36] D. Cassettari, A. Chenet, R. Folman, A. Haase, B. Hessmo, P. Krüger, T. Maier, S. Schneider, T. Calarco, and J. Schmiedmayer. Micromanipulation of neutral atoms with nanofabricated structures. *Appl. Phys. B*, 70:721, 2000.

[37] D. Cassettari, B. Hessmo, R. Folman, T. Maier, and J. Schmiedmayer. Beam splitter for guided atoms. *Phys. Rev. Lett.*, 85:5483, 2000.

[38] M. S. Chapman, T. D. Hammond, A. Lenef, J. Schmiedmayer, R. A. Rubenstein, E. Smith, and D. E. Pritchard. Photon scattering from atoms in an atom interferometer: Coherence lost and regained. *Phys. Rev. Lett.*, 75:3783, 1995.

[39] D. G. Cory, R. Laflamme, E. Knill, L. Violav, T. F. Havel, N. Boulant, G. Boutis, E. Fortunato, S. Lloyd, R. Martinez, C. Negrevergne, M. Pravia, Y. Sharf, G. Teklemariam, Y. S. Weinstein, and W. H. Zurek. NMR based quantum information processing: Achievements and prospects. *Fort. Phys.*, 48:875, 2000.

[40] R. Côté, A. Dalgarno, and M. J. Jamieson. Elastic scattering of two ^{7}Li atoms. *Phys. Rev. A*, 50:399, 1994.

[41] K. B. Davis, M.-O. Mewes, M. R. Andrews, N. J. van Druten, D. S. Durfee, D. M. Kurn, and W. Ketterle. Bose-Einstein condensation in a gas of sodium atoms. *Phys. Rev. Lett.*, 75:3969, 1995.

[42] K. B. Davis, M.-O. Mewes, M. R. Andrews, N. J. van Druten, D. S. Durfee, D. M. Kurn, and W. Ketterle. Bose-Einstein condensation in a gas of sodium atoms. *Phys. Rev. Lett.*, 75:3969, 1995.

[43] T. J. Davis. 2D magnetic traps for ultra-cold atoms: A simple theory using complex numbers. *Eur. Phys. J. D*, 18:27, 2002.

[44] N. H. Dekker, C. S. Lee, V. Lorent, J. H. Thywissen, S. P. Smith, M. Drndić, R. M. Westervelt, and M. Prentiss. Guiding neutral atoms on a chip. *Phys. Rev. Lett.*, 84:1124, 2000.

[45] J. Denschlag. *Kalte Atome in singulären Potentialen.* PhD thesis, Universität Innsbruck, 1998.

[46] J. Denschlag, D. Cassettari, and J. Schmiedmayer. Guiding neutral atoms with a wire. *Phys. Rev. Lett.*, 82:2014, 1999.

[47] J. Denschlag and J. Schmiedmayer. Scattering a neutral atom from a charged wire. *Europhys. Lett.*, 38:405, 1997.

[48] J. Denschlag, G. Umshaus, and J. Schmiedmayer. Probing a singular potential with cold atoms a neutral atom and a charged wire. *Phys. Rev. Lett.*, 81:737, 1998.

[49] S. Dettmer, D. Hellweg, P. Ryytty, J. J. Arlt, W. Ertmer, K. Sengstock, D. S. Petrov, G. V. Shlyapnikov, H. Kreutzmann, L. Santos, and M. Lewenstein. Observation of phase fluctuations in elongated Bose-Einstein condensates. *Phys. Rev. Lett.*, 87:160406, 2001.

[50] D. Deutsch. Quantum theory, the Church-Turing principle and the universal quantum computer. *Proc. Roy. Soc. London, Ser. A*, 400:97, 1985.

[51] M. Drndić, K. S. Johnson, J. H. Thywissen, M. Prentiss, and R. M. Westervelt. Micro-electromagnets for atom manipulation. *Appl. Phys. Lett.*, 72:2906, 1998.

[52] R. Dumke, T. Müther, M. Volk, W. Ertmer, and G. Birkl. Interferometer-type structures for guided atoms. *Phys. Rev. Lett.*, 89:220402, 2002.

[53] C. Durkan, M. A. Schneider, and M. E. Welland. Analysis of failure mechanisms in electrically stressed Au nanowires. *J. Appl. Phys.*, 86:1280, 1999.

[54] S. Earnshaw. On the nature of the molecular forces which regulate the constitution of the luminiferous ether. *Trans. Camb. Phil. Soc.*, 7:97, 1842.

[55] A. Einstein. Über die von der molekularkinetischen Theorie der Wärme geforderte Bewegung von in ruhenden Flüssigkeiten suspendierten Teilchen. *Ann. Phys.*, 17:549, 1905.

[56] A. Einstein. Über einen die Erzeugung und Verwandlung des Lichtes betreffenden heuristischen Gesichtspunkt. *Ann. Phys.*, 17:132, 1905.

[57] A. Einstein. Zur Elektrodynamik bewegter Körper. *Ann. Phys.*, 17:891, 1905.

[58] A. Einstein, B. Podolsky, and N. Rosen. Can quantum-mechanical description of physical reality be considered complete? *Phys. Rev.*, 47:777, 1935.

[59] B. Engeser. *Optische Abbildung einer atomaren Dichteverteilung*. Diploma thesis, Universität Heidelberg, 2002.

[60] J. Estève, C. Aussibal, T. Schumm, C. Figl, D. Mailly, I. Bouchoule, C. I. Westbrook, and A. Aspect. The role of wire imperfections in micro magnetic traps for atoms. 2004. physics/043020.

[61] R. Folman, P. Krüger, D. Cassettari, B. Hessmo, T. Maier, and J. Schmiedmayer. Controlling cold atoms using nanofabricated surfaces: Atom chips. *Phys. Rev. Lett.*, 84:4749, 2000.

[62] R. Folman, P. Krüger, J. Schmiedmayer, J. Denschlag, and C. Henkel. Microscopic atom optics: from wires to an atom chip. *Adv. At. Mol. Opt. Phys.*, 48:263, 2002.

[63] J. Fortagh, H. Ott, S. Kraft, A. Günther, and C. Zimmermann. Surface effects in magnetic microtraps. *Phys. Rev. A*, 66:041604(R), 2002.

[64] J. Fortagh, H. Ott, G. Schlotterbeck, C. Zimmermann, B. Herzog, and D. Wharam. Microelectromagnets for trapping and manipulating ultracold atomic quantum gases. *Appl. Phys. Lett.*, 81:1146–1148, 2002.

[65] H. Gauck, M. Hartl, D. Schneble, H. Schnitzler, T. Pfau, and J. Mlynek. Quasi-2D gas of laser cooled atoms in a planar matter waveguide. *Phys. Rev. Lett.*, 81:5298, 1998.

[66] M. E. Gehm, K. M. O'Hara, T. A. Savard, and J. E. Thomas. Dynamics of noise-induced heating in atom traps. *Phys. Rev. A*, 58:3914, 1998.

[67] H. Gimpel. *Magnetische Oberflächenfallen für Atom-Interferometer.* Diploma thesis, Universität Heidelberg, 2002.

[68] M. Girardeau. Relationship between systems of impenetrable bosons and fermions in one dimension. *J. Math. Ph.*, 1:516, 1960.

[69] Y. V. Gott, M. S. Ioffe, and V. G. Tel'kovskii. *Nucl. Fusion Supplement*, 3:1045, 1962.

[70] S. Gov, S. Shtrikman, and H. Thomas. Magnetic trapping of neutral particles: Classical and quantum-mechanical study of a Ioffe-Pritchard type trap. *J. Appl. Phys.*, 87:3989–3998, 2000.

[71] M. Greiner, O. Mandel, T. Esslinger, T. W. Hänsch, and I. Bloch. Quantum phase transition from a superfluid to a Mott insulator in a gas of ultracold atoms. *Nature*, 415:39, 2002.

[72] M. Greiner, C. A. Regal, and D. S. Jin. Emergence of a molecular Bose-Einstein condensate from a Fermi gas. *Nature*, 426:537, 2003.

[73] R. Grimm, M. Weidemüller, and Y. B. Ovchinnikov. Optical dipole traps for neutral atoms. *Adv. At. Mol. Opt. Phys.*, 42:95, 2000.

[74] S. Groth. PhD thesis, Universität Heidelberg, to be published 2006.

[75] S. Groth, P. Krüger, S. Wildermuth, R. Folman, T. Fernholz, D. Mahalu, I. Bar-Joseph, and J. Schmiedmayer. Atom chips: Fabrication and thermal properties. 2004. cond-mat/0404141.

[76] L. K. Grover. Quantum mechanics helps in searching for a needle in a haystack. *Phys. Rev. Lett.*, 79:325, 1997.

[77] T. L. Gustavson, A. P. Chikkatur, A. E. Leanhardt, A. Görlitz, S. Gupta, D. E. Pritchard, and W. Ketterle. Transport of Bose-Einstein condensates with optical tweezers. *Phys. Rev. Lett.*, 88:020401, 2002.

[78] A. Haase. *Trapping Atoms with a Paper Clip.* Diploma thesis, Universität Innsbruck, Freie Universität Berlin, 2000.

[79] A. Haase. PhD thesis, Universität Heidelberg, to be published 2004.

[80] A. Haase, D. Cassettari, A. Chenet, B. Hessmo, and J. Schmiedmayer. Trapping neutral atoms with a wire. *Phys. Rev. A*, 64:043405, 2001.

[81] E. Haller. Diplomarbeit, Universität Heidelberg, to be published 2004.

[82] W. Hänsel, P. Hommelhoff, T. W. Hänsch, and J. Reichel. Bose-Einstein condensation on a microelectronic chip. *Nature*, 413:498, 2001.

[83] W. Hänsel, J. Reichel, P. Hommelhoff, and T. W. Hänsch. Trapped-atom interferometer in a magnetic microtrap. *Phys. Rev. A*, 64:063607, 2001.

[84] D. M. Harber, J. M. McGuirck, J. M. Obrecht, and E. A. Cornell. Thermally induced losses in ultra-cold atoms magnetically trapped near room-temperature surfaces. *J. Low Temp. Phys*, 133:229, 2003. cond-mat/0307546.

[85] L. Hau, M. Burns, and J. Golovchenko. Bound states of guided matter waves: An atom and a charged wire. *Phys. Rev. A*, 45:6468, 1992.

[86] S. Haupt. *Setup of a New Experiment with Ultracold ^{87}Rb Atoms: Towards Quantum Information Processing on an Atom Chip*. Diploma thesis, Universität Heidelberg, 2003.

[87] W. Heisenberg. Über quantentheoretische Umdeutung kinematischer und mechanischer Beziehungen. *Z. Phys.*, 33:879, 1925.

[88] C. Henkel and S. A. Gardiner. Decoherence of Bose-Einstein condensates in microtraps. *Phys. Rev. A*, 69:043602, 2004.

[89] C. Henkel, K. Joulain, R. Carminati, and J.-J. Greffet. Spatial coherence of thermal near fields. *Opt. Commun.*, 186:57, 2000.

[90] C. Henkel, P. Krüger, R. Folman, and J. Schmiedmayer. Fundamental limits for coherent manipulation on atom chips. *Appl. Phys. B*, 76:173, 2003.

[91] C. Henkel and S. Pötting. Coherent transport of matter waves. *Appl. Phys. B*, 72:73, 2001.

[92] C. Henkel, S. Pötting, and M. Wilkens. Loss and heating of particles in small and noisy traps. *Appl. Phys. B*, 69:379, 1999.

[93] C. Henkel and M. Wilkens. Heating of trapped atoms near thermal surfaces. *Europhys. Lett.*, 47:414, 1999.

[94] C. Henkel and M. Wilkens. Heating of trapped particles close to surfaces — blackbody and beyond. *Acta Phys. Slov.*, 50:293, 2000.

[95] E. A. Hinds and C. Eberlein. Quantum propagation of neutral atoms in a magnetic quandrupole guide. *Phys. Rev. A*, 61:033614, 2000. erratum: *ibid.* 64, 039902 (2001).

[96] E. A. Hinds and I. G. Hughes. Magnetic atom optics: Mirrors, guides, traps, and chips for atoms. *J. Phys. D*, 32:R119, 1999.

[97] E. A. Hinds, C. J. Vale, and M. G. Boshier. Two-wire waveguide and interferometer for cold atoms. *Phys. Rev. Lett.*, 86:1462, 2001.

[98] S. Hofferberth. Diploma thesis, Universität Heidelberg, to be published 2004.

[99] M. J. Holland, C. Menotti, and L. Viverit. The role of boson-fermion correlations in the resonance theory of superfluids. cond- mat/ 0404234.

[100] P. Horak, B. G. Klappauf, A. Haase, R. Folman, J. Schmiedmayer, P. Domokos, and E. A. Hinds. Possibility of single-atom detection on a chip. *Phys. Rev. A*, 67:043806, 2003.

[101] Y. Imry. *Introduction to Mesoscopic Physics*. Oxford University Press, Oxford, 1997.

[102] D. Jaksch, H.-J. Briegel, J. I. Cirac, C. W. Gardiner, and P. Zoller. Entanglement of atoms via cold controlled collisions. *Phys. Rev. Lett.*, 82:1975, 1999.

[103] T. Jennewein, G. Weihs, J. W. Pan, and A. Zeilinger. Experimental nonlocality proof of quantum teleportation and entanglement swapping. *Phys. Rev. Lett.*, 88:017903, 2002.

[104] S. Jochim, M. Bartenstein, A. Altmeyer, G. Hendl, S. Riedl, C. Chin, J. Hecker Denschlag, and R. Grimm. Bose-Einstein condensation of molecules. *Science Express, 13 November 2003 (10.1126/science.1093280)*, 2003.

[105] S. Jochim, M. Bartenstein, G. Hendl, J. Hecker Denschlag, R. Grimm, A. Mosk, and M. Weidemüller. Magnetic field control of elastic scattering in a cold gas of fermionic lithium atoms. *Phys. Rev. Lett.*, 89:273202, 2002.

[106] J. B. Johnson. Thermal agitation of electricity in conductors. *Phys. Rev.*, 32:97–109, 1928.

[107] M. P. A. Jones, C. J. Vale, D. Sahagun, B. V. Hall, and E. A. Hinds. Spin coupling between cold atoms and the thermal fluctuations of a metal surface. *Phys. Rev. Lett.*, 91:080401, 2003.

[108] P. S. Julienne, F. H. Mies, E. Tiesinga, and C. J. Williams. Collisional stability of double Bose condensates. *Phys. Rev. Lett.*, 78:1880, 1997.

[109] A. Kasper. *Bose-Einstein condensation in a robust microtrap – the combination of wire traps and atom chips*. PhD thesis, Universität Heidelberg, 2003.

[110] W. Ketterle, K. B. Davis, M. A. Joffe, A. Martin, and D. E. Pritchard. High densities of cold atoms in a dark spontaneous-force optical trap. *Phys. Rev. Lett.*, 70:2253, 1993.

[111] W. Ketterle and D. Pritchard. Trapping and focusing ground-state atoms with static fields. *Appl. Phys. B*, 54:403, 1992.

[112] M. W. Klein. *Elektrostatische Felder auf Atomchips: Kalte Atome in neuen Mikrofallen*. Diploma thesis, Universität Heidelberg, 2002.

[113] S. J. J. M. F. Kokkelmans, H. M. J. M. Boesten, and B. J. Verhaar. Role of collisions in creation of overlapping Bose condensates. *Phys. Rev. A*, 55:R1589, 1997.

[114] S. Kraft, A. Günther, H. Ott, D. Wharam, C. Zimmermann, and J. Fortagh. Anomalous longitudinal magnetic field near the surface of copper conductors. *J. Phys. B*, 35:L469, 2002.

[115] H. Kreutzmann, U. V. Poulsen, M. Lewenstein, R. Dumke, W. Ertmer, G. Birkl, and A. Sanpera. Coherence properties of guided-atom interferometers. *Phys. Rev. Lett.*, 92:163201, 2004.

[116] P. Krüger. *Von der Laserdiode zum Atom Chip: Aufbau einer magnetooptischen Falle und Experimente mit ultrakalten Atomen in mikroskopischen Magnetfallen*. Diploma thesis, Universität Innsbruck, Freie Universität Berlin, 2000.

[117] P. Krüger et al. Reduction of surface disorder potentials near lithographically fabricated atom chips. In preparation, 2004.

[118] P. Krüger, A. Haase, R. Folman, and J. Schmiedmayer. Quantum information processing with neutral atoms on atom chips. In T. Beth and G. Leuchs, editors, *Quantum Information Processing*, pages 257–265, Berlin, 2002. Wiley.

[119] P. Krüger, X. Luo, M. W. Klein, K. Brugger, A. Haase, S. Wildermuth, S. Groth, I. Bar-Joseph, R. Folman, and J. Schmiedmayer. Trapping and manipulating neutral atoms with electrostatic fields. *Phys. Rev. Lett.*, 91:233201, 2003.

[120] P. Krüger and J. Schmiedmayer. Atome im Strahlteiler. *Physik in unserer Zeit*, 32:60, 2001.

[121] P. Krüger and J. Schmiedmayer. Atomchips: Integrated circuits for matter wave manipulation. *Contemp. Phys.*, 2004. In preparation.

[122] A. E. Leanhardt, A. P. Chikkatur, D. Kielpinski, Y. Shin, T. L. Gustavson, W Ketterle, and D. E. Pritchard. Propagation of Bose-Einstein condensates in a magnetic waveguide. *Phys. Rev. Lett.*, 89:040401, 2002.

[123] A. E. Leanhardt, Y. Shin, A. P. Chikkatur, D. Kielpinski, W. Ketterle, and D. E. Pritchard. Bose-Einstein condensates near a microfabricated surface. *Phys. Rev. Lett.*, 90:100404, 2003.

[124] K. I. Lee, J. A. Kim, H. R. Noh, and W. Jhe. Single beam atom trap in a pyramidal and conical hollow mirror. *Opt. Lett.*, 21:1177, 1996.

[125] P. Lemonde, O. Morice, E. Peik, J. Reichel, H. Perrin, W. Hänsel, and C. Salomon. An opto-electric trap for cold atoms. *Europhys. Lett.*, 32:555, 1995.

[126] A. Lenef, T. D. Hammond, E. T. Smith, M. S. Chapman, R. A. Rubenstein, and D. E. Pritchard. Rotation sensing with an atom interferometer. *Phys. Rev. Lett.*, 78:760, 1997.

[127] I. Lesanovsky. *Rydberg-Atome in magnetischen Quadrupolfallen*. Diploma thesis, Universität Heidelberg, 2003.

[128] I. Lesanovsky. 2004. In preparation.

[129] I. Lesanovsky, J. Schmiedmayer, and P. Schmelcher. Electronic structure of atoms in magnetic quadrupole traps. *Phys. Rev. A*, 69:053405, 2004.

[130] B. Lev. Fabrication of micro-magnetic traps for cold neutral atoms. *Quant. Inf. Comp.*, 3:450–464, 2003. quant-ph/0305067.

[131] Y. Lin, I. Teper, C. Chin, and V. Vuletić. Impact of the Casimir-Polder potential and Johnson noise on Bose-Einstein condensate stability near surfaces. *Phys. Rev. Lett.*, 92:050404, 2004.

[132] O. J. Luiten, M. W. Reynolds, and J. T. M. Walraven. Kinetic theory of the evaporative cooling of a trapped gas. *Phys. Rev. A*, 53:381, 1996.

[133] X. Luo, P. Krüger K. Brugger, S. Wildermuth, H. Gimpel, M. Klein, S. Groth, R. Folman, I. Bar-Joseph, and J. Schmiedmayer. An atom fiber for guiding cold neutral atoms. 2004. quant-ph/0311174.

[134] E. Majorana. Atomi orientati incampo magnetico variabile. *Nuovo Cimento*, 9:43, 1932.

[135] I. Marcikic, H. de Riedmatten, W. Tittel, H. Zbinden, and N. Gisin. Long-distance teleportation of qubits at telecommunication wavelengths. *Nature*, 421:509, 2003.

[136] N. Masuhara, J. M. Doyle, J. C. Sandberg, D. Kleppner, T. J. Greytak, H. F. Hess, and G. P. Kochanski. Evaporative cooling of spin-polarized atomic hydrogen. *Phys. Rev. Lett.*, 61:935, 1988.

[137] R. A. Matula. Electrical resistivity of copper, gold, palladium, and silver. *J. Phys. Chem. Ref. Data*, 8:1147, 1979.

[138] J. M. McGuirk, D. M. Harber, J. M. Obrecht, and E. A. Cornell. Alkali adsorbate polarization on conducting and insulating surfaces probed with Bose-Einstein condensates. cond-mat/0403254, 2004.

[139] C. Menotti, J. R. Anglin, J. I. Cirac, and P. Zoller. Dynamic splitting of a Bose-Einstein condensate. *Phys. Rev. A*, 63:023601, 2001.

[140] H. J. Metcalf. *Laser Cooling and Trapping*. Springer Verlag, Heidelberg Berlin New York, 1999.

[141] D. Müller, D. Z. Anderson, R. J. Grow, P. D. D. Schwindt, and E. A. Cornell. Guiding neutral atoms around curves with lithographically patterned current-carrying wires. *Phys. Rev. Lett.*, 83:5194, 1999.

[142] D. Müller, E. A. Cornell, M. Prevedelli, P. D. D. Schwindt, A. Zozulya, and D. Z. Anderson. Waveguide atom beam splitter for laser-cooled neutral atoms. *Opt. Lett.*, 25:1382, 2000.

[143] C. J. Myatt, E. A. Burt, R. W. Ghrist, and E. A. Cornelland C. E. Wieman. Production of two overlapping Bose-Einstein condensates by sympathetic cooling. *Phys. Rev. Lett.*, 78:586, 1997.

[144] A. Negretti, T. Calarco, and C. Henkel. Unpublished, 2004.

[145] W. Neuhauser, M. Hohenstatt, P. E. Toschek, and H. Dehmelt. Localized visible Ba^+ mono-ion oscillator. *Phys. Rev. A*, 22:1137, 1980.

[146] M. A. Nielsen and I. L. Chuang. *Quantum Computation and Quantum Information*. Cambridge University Press, Cambridge, 2000.

[147] H. Nyquist. Thermal agitation of electric charge in conductors. *Phys. Rev.*, 32:110–113, 1928.

[148] M. Oberthaler. 2004. Unpublished.

[149] D. O'Dell, S. Giovanazzi, G. Kurizki, and V. M. Akulin. Bose-Einstein condensates with 1/r interatomic attraction: Electromagnetically induced "gravity". *Phys. Rev. Lett.*, 84:5687, 2000.

[150] M. Olshanii. Atomic scattering in the presence of an external confinement and a gas of impenetrable bosons. *Phys. Rev. Lett.*, 81:938, 1998.

[151] H. Ott, J. Fortagh, G. Schlotterbeck, A. Grossmann, and C. Zimmermann. Bose-Einstein condensation in a surface microtrap. *Phys. Rev. Lett.*, 87:230401, 2001.

[152] T. Palm and L. Thylén. Analysis of an electron-wave Y-branch switch. *Appl. Phys. Lett.*, 60:237, 1992.

[153] B. Parades, A. Widera, V. Murg, O. Mandel, S. Fölling, I. Cirac, G. V. Shlyapnikov, T. W. Hänsch, and I. Bloch. Tonks-Girardeau gas of ultracold atoms in an optical lattice. *Nature*, 429:277, 2004.

[154] W. Paul. Electromagnetic traps for charged and neutral particles. *Rev. Mod. Phys.*, 62:531, 1990.

[155] A. Peters, K. Y. Chung, and S. Chu. Measurement of gravitational acceleration by dropping atoms. *Nature*, 400:849, 1999.

[156] W. Petrich, M. H. Anderson, J. R. Ensher, and E. A. Cornell. A stable, tightly confining magnetic trap for evaporative cooling of neutral atoms. *Phys. Rev. Lett.*, 74:3352, 1995.

[157] D. S. Petrov, G. V. Shlyapnikov, and J. T. M. Walraven. Regimes of quantum degeneracy in trapped 1D gases. *Phys. Rev. Lett.*, 85:3745, 2000.

[158] D. S. Petrov, G. V. Shlyapnikov, and J. T. M. Walraven. Phase-fluctuating 3D Bose-Einstein condensates in elongated traps. *Phys. Rev. Lett.*, 87:050404, 2001.

[159] T. Pfau, H. Gauck, D. Schneble, M. Hartl, and J. Mlynek. In *Quantum Electronics Conf. Vol. 17*, Washington D.C., 1997. OSA.

[160] T. Pfau and J. Mlynek. A 2D quantum gas of laser cooled atoms. In K. Burnett, editor, *Ultracold Atoms and Bose-Einstein-Condensation (Proceedings of the European Quantum Electronics Conference, Sept. 1996, Hamburg, Germany)*, volume 7, page 33, Washington D. C., 1996. Trends in Optics and Photonics Series, Optical Society of America.

[161] M. Planck. Zur Theorie des Gesetzes der Energieverteilung im Normalspektrum. *Verh. Dt. Phys. Ges.*, 2:237, 1900.

[162] D. Pritchard. Cooling neutral atoms in a magnetic trap for precision spectroscopy. *Phys. Rev. Lett.*, 51:1336, 1983.

[163] E. L. Raab, M. Prentiss, A. Cable, S. Chu, and D. E. Pritchard. Trapping of neutral sodium atoms with radiation pressure. *Phys. Rev. Lett.*, 59:2631, 1987.

[164] A. Rauschenbeutel, G. Noguesv, S. Osnaghi, P. Bertet, M. Brune, J.M. Raimond, and S. Haroche. Step by step engineered many particle entanglement. *Science*, 288:2024, 2000.

[165] J. Reichel. Microchip traps and Bose-Einstein condensation. *Appl. Phys. B*, 74:469, 2002.

[166] J. Reichel, W. Hänsel, and T. W. Hänsch. Atomic micromanipulation with magnetic surface traps. *Phys. Rev. Lett.*, 83:3398, 1999.

[167] P. K. Rekdal, S. Scheel, P. L. Knight, and E. A. Hinds. Thermal spin flips in atom chips. quant-ph/0403166, 2004.

[168] J. A. Sauer, M. D. Barret, and M. S. Chapman. Storage ring for neutral atoms. *Phys. Rev. Lett.*, 87:270401, 2001.

[169] T. A. Savard, K. M. O'Hara, and J. E. Thomas. Laser-noise-induced heating in far-off resonance optical traps. *Phys. Rev. A*, 56:R1095, 1997.

[170] H. Schmaljohann, M. Erhard, J. Kronjäger, M. Kottke, S. van Staa, L. Cacciapuoti, J. J. Arlt, K. Bongs, and K. Sengstock. Dynamics of F = 2 spinor Bose-Einstein condensates. *Phys. Rev. Lett.*, 92:040402, 2004.

[171] J. Schmiedmayer, R. Folman, and T. Calarco. The neutral atom as a qubit for quantum computation. *J. Mod. Opt.*, 49:1375, 2002.

[172] D. Schneble, H. Gauck, M. Hartl, T. Pfau, and J. Mlynek. Optical atom traps at surfaces. In M. Inguscio, S. Stringari, and C. Wieman, editors, *Proceedings of the International School of Physics "Enrico Fermi" (Varenna 1998): Bose-Einstein Condensation in Atomic Gases*, page 469, Amsterdam, 1999. IOS Press.

[173] S. Schneider. *Bose-Einstein Kondensation in einer magnetischen Z-Falle*. PhD thesis, Universität Heidelberg, 2003.

[174] S. Schneider, A. Kasper, Ch. Vom Hagen, M. Bartenstein, B. Engeser, T. Schumm, I. Bar-Joseph, R. Folman, L. Feenstra, and J. Schmiedmayer. Bose-Einstein condensation in a simple microtrap. *Phys. Rev. A*, 67:023612, 2003.

[175] F. Schreck, L. Khaykovich, K. L. Corwin, G. Ferrari, J. Cubizolles T. Bourdel, and C. Salomon. A quasi-pure Bose-Einstein condensate immersed in a Fermi sea. *Phys. Rev. Lett.*, 87:080403, 2001.

[176] E. Schrödinger. Quantisierung als Eigenwertproblem. *Ann. Phys.*, 79:361, 1926.

[177] F. Shimizu and M. Morinaga. Electric trapping of neutral atoms. *Jpn. J. Appl. Phys.*, 31:L1721, 1992.

[178] P. W. Shor. Algorithms for quantum computation: Discrete logarithms and factoring. *Proceedings of the 35th Annual Symposium on Foundations of Computer Science, IEEE Comput. Soc. Press*, page 124, 1994.

[179] R. J. C. Spreeuw, D. Voigt, B. T. Wolschrijn, and H. B. van Linden van den Heuvell. Creating a low-dimensional quantum gas using dark states in an inelastic evanescent-wave mirror. *Phys. Rev. A*, 61:053604, 2000.

[180] A. Stern, Y. Aharonov, and Y. Imry. Phase uncertainty and loss of interference: A general picture. *Phys. Rev. A*, 41:3436–48, 1990.

[181] O. Stern and W. Gerlach. Der experimentelle Nachweis der Richtungsquantelung im Magnetfeld. *Z. Phys.*, 9:349, 1922.

[182] C. I. Sukenik, M. G. Boshier, D. Cho, V. Sandoghdar, and E. A. Hinds. Measurement of the Casimir-Polder force. *Phys. Rev. Lett.*, 70:560, 1993.

[183] C. V. Sukumar and D. M. Brink. Spin-flip transitions in a magnetic trap. *Phys. Rev. A*, 56:2451, 1997.

[184] T.Calarco, E. A. Hinds, D. Jaksch, J. Schmiedmayer, J. I. Cirac, and P. Zoller. Quantum gates with neutral atoms: Controlling collisional interactions in time-dependent traps. *Phys. Rev. A*, 61:022304, 2000.

[185] E. Timmermans and R. Côté. Superfluidity in sympathetic cooling with atomic Bose-Einstein condensates. *Phys. Rev. Lett.*, 80:3419, 1998.

[186] L. Tonks. The complete equation of state of one, two and three-dimensional gases of hard elastic spheres. *Phys. Rev.*, 50:955, 1936.

[187] P. Treutlein, P. Hommelhoff, T. Steinmetz, T. W. Hänsch, and J. Reichel. Coherence in Microchip Traps. *Phys. Rev. Lett.*, 92:203005, 2004.

[188] Q. A. Turchette, C. J. Myatt, B. E. King, C. A. Sackett, D. Kielpinski, W. M. Itano, C. Monroe, and D. J. Wineland. Decoherence and decay of motional quantum states of a trapped atom coupled to engineered reservoirs. *Phys. Rev. A*, 62:053807, 2000.

[189] T. Varpula and T. Poutanen. Magnetic field fluctuations arising from thermal motion of electric charge in conductors. *J. Appl. Phys.*, 55:4015–21, 1984.

[190] D.-W. Wang, M. D. Lukin, and E. Demler. Disordered Bose-Einstein condensates in quasi-one-dimensional magnetic microtraps. *Phys. Rev. Lett.*, 92, 2004.

[191] J. Weiner, V. S. Bagnato, S. Zilio, and P. S. Julienne. Experiments and theory in cold and ultracold collisions. *Rev. Mod. Phys.*, 71:1, 1999.

[192] J. D. Weinstein and K. G. Libbrecht. Microscopic magnetic traps for neutral atoms. *Phys. Rev. A*, 52:4004, 1995.

[193] J.-O. J. Wesström. Self-gating effect in the electron Y-branch switch. *Phys. Rev. Lett.*, 82:2564, 1999.

[194] J. A. Wheeler and W. H. Zurek, editors. *Quantum Theory and Measurement*. Princeton University Press, Princeton, 1983.

[195] S. Wildermuth. *Neue Experimente mit Atomchips*. Diploma thesis, Universität Heidelberg, 2002.

[196] S. Wildermuth. PhD thesis, Universität Heidelberg, to be published 2005.

[197] S. Wildermuth, P. Krüger, C. Becker, M. Brajdic, S. Haupt, A. Kasper, R. Folman, and J. Schmiedmayer. Optimized mageto-optical trap for experiments with ultracold atoms near surfaces. *Phys. Rev. A*, 69:030901(R), 2004.

[198] M. Wilzbach. PhD thesis, Universität Heidelberg, to be published 2005.

[199] L. Windholz, M. Musso, G. Zerza, and H. Jäger. Precise Stark-effect investigations of the lithium D1 and D2 lines. *Phys. Rev. A*, 46:5812, 1992.

[200] W. H. Wing. On neutral particle trapping in quasistatic electromagnetic fields. *Prog. Quant. Electr.*, 8:181, 1984.

[201] W. H. Zurek. Decoherence and the transition from quantum to classical. *Physics Today*, 44(October):36, 1991.